Fig 2.3

ABSTRACT

SEARCH FOR TIME REVERSAL SYMMETRY VIOLATION IN THALLIUM FLUORIDE USING A JET SOURCE

Donghyun Cho

Yale University

May 1990

We have looked for a violation of time reversal symmetry in the molecule thallium fluoride using a rotationally cold beam from a jet source. We measured a frequency shift of thallium nuclear magnetic resonance when external electric field of 29.5 kV/cm was reversed with respect to the magnetic quantization axis. The measured shift, $(1.4 \pm 2.4) \times 10^{-4}$ Hz, was interpreted as a null result. It constitutes a tenfold improvement in sensitivity over the previous measurement. Accordingly it lowered the upper limits on the proton and electron electric dipole moments and other T-violating weak couplings that could be derived from the frequency shift.

SEARCH FOR
TIME REVERSAL SYMMETRY VIOLATION
IN THALLIUM FLUORIDE
USING A JET SOURCE

A dissertation

Presented to the Faculty of the Graduate School

of

Yale University

in Candidacy for the Degree of

Doctor of Philosophy

by

Donghyun Cho

May 1990

Table of Contents

List of Figures

List of Tables

CHAPTER 1

INTRODUCTION

Symmetry principles provide physicists with a valuable map for a systematic investigation of complicated natural phenomena. Even the simplest one of spatial translation has the important result of linear momentum conservation that allows us to study the center of mass and the internal motions of an isolated system separately. The more intricate symmetry of Lorentz invariance puts very stringent limits on physically acceptable forms of a theory: one probably has to go a long way to give even a slightest consideration to a theory that is not compatible with this invariance principle. Besides those related to the geometric transformations of space and time, or spacetime, there are symmetries that are specific to a given system or the interactions governing it. As an example, in a nuclear structure the similar interactions of proton and neutron can be looked at in terms of $SU(2)$ isospin symmetry.

While the symmetry principles are useful because they are largely respected by Nature, it was the discoveries of their violations in some fundamental interactions that had most dramatic impact on physics over the last forty years. The discovery of parity (spatial inversion, P) violation in 1957 led to a new theory of weak interaction and eventually the unification of electromagnetic and weak forces. By contrast, the subsequent revelation in 1964 that in a decay mode of the neutral kaon the combined transformation CP of charge conjugation and parity was not an exact symmetry either remains an isolated phenomenon. The violation of

CP-invariance in neutral kaon decay is very closely related to that of another invariance, time reversal (T) and our search for a T-violating permanent electric dipole moment in molecular TlF is one of the latest efforts to get an understanding of those broken symmetries and hopefully of the new physics in them.

1.1 Time Reversal in Quantum Mechanics

In quantum mechanics, invariance of an interaction Hamiltonian H under a transformation Ω implies the commutation relation,

$$[H, \Omega] = 0. \tag{1.1}$$

As a direct consequence of this relation, if $|\Psi_n\rangle$ is an eigenstate of H with an eigenvalue ω_n, so is the transformed state $\Omega|\Psi_n\rangle$, i.e.

$$H(\Omega|\Psi_n\rangle) = \omega_n(\Omega|\Psi_n\rangle). \tag{1.2}$$

Furthermore when $\Omega|\Psi_n\rangle$ is independent from $|\Psi_n\rangle$, there is a degeneracy associated with the eigenvalue ω_n. It was this type of degeneracy from T-invariance, known as Kramers degeneracy, that led to the introduction of the time reversal transformation in quantum mechanics by Wigner in 1932 [WIG32]. While T shares many properties with other discrete transformations like P and C, it is unique for its antiunitarity - see e.g. [SCH68].

$$T = UK, \tag{1.3}$$

where U is unitary and K is an operator for complex conjugation,

$$KzK^{-1} = z^*. \tag{1.4}$$

For the case of space inversion or charge conjugation, the unitarity of P and C together with the properties, $P^2 = I$ and $C^2 = I$ makes them Hermitian and their eigenvalues are observables. In particular, when a system exhibits symmetry under those transformations, the eigenvalues become conserved quantities. In the mid 1950s the observation that K^+ could decay into two different states of opposite P eigenvalues ($\tau - \theta$ paradox) stimulated the

investigations [LEE56] that led to the discovery of P-violation [WU57]. And similarly for the neutral kaon it was the nonconservation of the eigenvalues for *CP* before and after a decay that signaled CP-violation (§ 1.2). On the other hand, because of its antiunitarity there is no conserved observable associated with *T* and the implication of T-invariance is quite different from those of C and P. In dynamic processes T-invariance takes the form of the principle of detailed balance that requires forward and backward rates be the same. For an atomic or molecular system its application leads to the absence of particular electromagnetic multipole moments of the system. The electric dipole or magnetic quadrupole moment is such an example [SAC87].

1.2 CP- and T-Violations in K^o Decay

1.2.1 Discovery of CP- and T-Violations

The particle-antiparticle pair of neutral kaons, (K^o, $\overline{K}^o$) have been a rich source of interesting phenomena in weak interaction physics which include the strangeness (S) oscillation and the K^o regeneration [PER82]. Those effects are related to the fact that the kaons are produced in a strong interaction which conserves the strangeness - e.g. $\pi^- p \rightarrow \Lambda K^o$ - while they can decay only through a weak interaction of $\Delta S = 1$. And for a free kaon the eigenstates of the total Hamiltonian including weak interaction are given by

$$|K_1\rangle = \frac{1}{\sqrt{2}}(|K^o\rangle + |\overline{K}^o\rangle) \qquad (1.5.a)$$

$$|K_2\rangle = \frac{1}{\sqrt{2}}(|K^o\rangle - |\overline{K}^o\rangle). \qquad (1.5.b)$$

With C invariance assumed, these states were originally interpreted as the simultaneous eigenstates of both charge conjugation and the Hamiltonian. But with the fall of the

separate invariances of P and C in the weak interaction it was replaced with the combined symmetry of CP, and $|K_1\rangle$ and $|K_2\rangle$ were identified as the eigenstates of *CP* with the eigenvalues of +1 and -1, respectively.

$$CP|K_1\rangle = |K_1\rangle \tag{1.6.a}$$

$$CP|K_2\rangle = -|K_2\rangle. \tag{1.6.b}$$

The kaon mass is about 3.5 times the pion mass, and there are two channels for hadronic decays of the neutral kaons: into two pions and three pions, the former being much faster because of the larger phase space available for the decay products. The two-pion system in an *s* state has an even parity and it is unchanged under a *C* operation, which makes it an eigenstate of the combined operation with CP=+1. On the other hand similar analysis shows that the three-pion system is an eigenstate with CP=-1.

$$CP(2\pi) = +1 \tag{1.7.a}$$

$$CP(3\pi) = -1. \tag{1.7.b}$$

Then under the CP-invariant situation $|K_1\rangle$ can only decay into two pions (short-lived state), and $|K_2\rangle$ only into three pions (long-lived state). In their landmark experiment in 1964, however, Christenson, Cronin, Fitch, and Turlay found that the long-lived state occasionally decay into two pions establishing the first - and the only - experimental evidence of CP-violation [CHR64]. Their result can be summarized in the branching ratio of

$$\frac{\Gamma(K_L \to \pi^+\pi^-)}{\Gamma(K_L \to \text{all charged modes})} = (2.0 \pm 0.4) \times 10^{-3}. \tag{1.8}$$

The mixed decays imply that the eigenstates are superpositions of $|K_1\rangle$ and $|K_2\rangle$,

$$|K_L\rangle = (1 + |\varepsilon|^2)^{-1/2} (\varepsilon|K_1\rangle + |K_2\rangle), \tag{1.9}$$

with $\varepsilon \cong 2.3 \times 10^{-3}$. Subsequent experiments confirmed the discovery [KLE89].

It is customary to interpret the finding as an indirect evidence for the violation of time reversal invariance so that the symmetries of CP and T are separately broken. To do so one makes a reference to the CPT theorem which states that a locally Lorentz-invariant field with a Hermitian interaction Hamiltonian is automatically invariant under the combined transformation of C, P and T taken in any order. From the theorem it follows that the CP-violation means the complementary breakdown of time reversal to save the CPT-invariance. It has also been argued that the data from kaon decay could be considered as an evidence of T-violation without going through the CPT theorem [CAS69]. In another approach one can relax the condition on the interaction Hamiltonian so that it can have an anti-Hermitian part [SAC86]. Now the CPT-invariance is not guaranteed and still the experimental data cannot be interpreted consistently without introducing T-violation.

Either with or without the CPT theorem the discovery was followed by great activity to find a satisfactory theory which incorporated the CP-violation in a natural way. There were also many experimental searches for other cases where CP or T is violated.

1.2.2 Proposed Theories

Over the years many different CP-violating theories or models have been proposed and each of them has one or more free parameters that can be fitted to the existing experimental data. One of the earliest attempts was to introduce a completely new type of interaction - superweak interaction - that took the responsibility for the CP-violation of the kaon decay [WOL64]. In this theory K^0 and $\overline{K}^0$ are directly coupled by a $\Delta S = 2$ interaction which can mix $|K_1\rangle$ and $|K_2\rangle$. This mixing is approximately related to the parameter ε in Eq. (1.9) by

$$\varepsilon = \frac{\langle K_1 | H_{sw} | K_2 \rangle}{\Delta m}, \tag{1.10}$$

where H_{sw} is the superweak Hamiltonian that couples K^o and $\overline{K}^o$ and Δm is the mass difference between K_1 and K_2. Noting that $\Delta m/m_K = 0.7 \times 10^{-14}$ is from second-order weak couplings [COM83] or equivalently $\Delta m \cong 10^{-7} < H_w >$ we may conclude that

$$\langle H_{sw} \rangle \sim 10^{-10} \cdot \langle H_w \rangle, \tag{1.11}$$

i.e. the superweak interaction is, if it exists, a very minute one and it is the small mass difference of the kaons that makes its effect observable. For this reason we do not expect its appearance in any other physical phenomena with possible exceptions of the analogous systems like B^o or D^o. Therefore the superweak idea still remains compatible with the currently known data.

In the framework of the weak interaction, where only $\Delta S = 0$ or 1 transitions are allowed, the coupling between K^o and $\overline{K}^o$ can come from a second-order process. Along this line of approach, Kobayashi and Maskawa generalized [KOB73] the Cabibbo-GIM formalism of the quark mixing in weak interaction in such a way that the new theory could have a room for CP-violation. In the KM model, as it is called, they introduced a new generation of the quark doublet (t,b) to complement those of (u,d) and (c,s) that were the constituents of the GIM model. The generalized weak current from the quarks can be written as

$$J^{\mu}(q) = \frac{1}{2}(\overline{u}, \overline{c}, \overline{t})\gamma_{\mu}(1-\gamma^5)U \begin{pmatrix} d \\ s \\ b \end{pmatrix}, \tag{1.12}$$

where U is a 3x3 unitary matrix that governs the quark mixing. In the model with only two generations of quarks the corresponding unitary matrix is of size 2x2 and it can be completely specified by a single real number - Cabibbo angle θ_C - after taking into account independent phase relations among the quark states. The resulting interaction Hamiltonian is forced to be CP-invariant. On the other hand, in the generalized version there are four free parameters left for the matrix U; three for Cabibbo type angles and one for a phase

factor $e^{i\delta}$. In this scheme, unless some deeper symmetry dictates δ to be zero, the coupling U is normally complex. When the amplitude for a hadronic weak process is given in the form of

$$A = \frac{4G}{\sqrt{2}} J^{\mu}(q) \cdot J_{\mu}^{+}(q), \tag{1.13}$$

it can be shown, e.g. [HAL84a], that the complex nature of the matrix U leads to the violation of CP-invariance. For its natural way of incorporating CP-violation and with the subsequent discovery of the b (bottom) quark - t (top) quark has not been discovered yet - the KM model has become the "standard model" for CP-violation in weak interaction. Reasonable parametrizations of the quark-mixing matrix U give a correct prediction on the CP-violation in the kaon decay, which makes it a popular theory in the kaon physics as well. The KM model, however, should be taken with some reservations because the phase angle δ was introduced in an ad hoc way rather than from a first principle. Furthermore it is always possible that more than one mechanism contributes to CP-violation.

T.D. Lee and Weinberg came up with somewhat different ways of generalizing the Weinberg-Salam standard model of electroweak interaction to explain observed CP-violation. While in the KM model CP-violation is from the phase relation among the quarks participating in weak interaction - or the phase introduced in couplings between the quarks and the intermediate vector bosons $W^{\pm}$ - in the ideas of Lee and Weinberg it is the phase introduced between different Higgs fields that leads to the violation. Lee proposed [LEE73] a theory with two Higgs doublets and after some fine tunings of the parameters the theory was reconcilable with the kaon data. In the theory of Weinberg [WEI76] CP-violation was also from the Higgs sector, but there were three Higgs boson fields and it was the coupling among those fields that gave rise to the violation of CP. At present it is uncertain whether this theory can be compatible with all the experimental data.

There are also theories where the strong interaction appears to be responsible for CP-violation. In this type of theory the matrix element for the CP-violating decay $K_L \rightarrow 2\pi$ can be written as

$$A \cong \sum_n \frac{\langle K_L | H_W | \Psi_n \rangle \langle \Psi_n | H_{ST}^{'} | 2\pi \rangle}{m_K - E_n}, \tag{1.14}$$

where $|\Psi_n\rangle$ is a state with S=0 and CP=-1 so that weak interaction takes care of $\Delta S = 1$ and $H_{ST}^{'}$ introduces CP-violation. It is smaller than the corresponding one for $K_S \rightarrow 2\pi$ by the factor of ε and we put

$$\frac{\langle \Psi_n | H_{ST}^{'} | 2\pi \rangle}{m_K - E_n} \sim 10^{-3}, \tag{1.15}$$

where $m_K - E_n$ is of the order of typical strength of strong interaction. It follows that $H_{ST}^{'}$ is only 10^{-3} of the regular strong interaction, hence the name millistrong theory. Actually, the non-Abelian nature of QCD also allows the vacuum to violate CP-invariance, but from the measurements on the neutron electric dipole moment the CP-violation from the vacuum is known to be small and does not account for that in kaon decay.

Many physicists believe that CP-violation in the early universe is responsible for the matter-antimatter asymmetry we observe every day. In that case it is an example of CP-violation in the high, very high, energy limit while that of the kaon decay provides us with the low energy window to the asymmetry.

1.2.3 Experiments in Heavy Mesons

The CP-violation so far observed can be reduced to one parameter, ε. It is quite obvious that we need more facts to get a better idea of what is the underlying physics, and other examples of CP-violation in Nature has been actively sought over the last 25 years. In the field of high energy physics the best hope seems to be in the systems of heavy

mesons - especially B^0 and $\overline{B}^0$ - which are expected to exhibit CP-violating behavior similar to the neutral kaons. On the basis of the KM model one can even argue that there will be larger CP-violating effects in those mesons because in the mixing matrix U the complex phase $e^{i\delta}$ is associated with the heavier quarks. In practice, however, the large mass of them can make detection of such effects very difficult. For the case of the kaons, observations of CP-violation were assisted by the large difference in the lifetimes between the long-lived and the short-lived species, which is a consequence of their lightness. The mass of the B meson, on the other hand, is estimated to be 38 times the pion mass, and the corresponding increase in the number of possible decay channels and available phase space for decay products can wipe out the difference we have seen in the kaons. For the same reason one also has to worry about the small branching ratio of final states of interest. In spite of these difficulties there are many interesting CP-asymmetries that can be looked for from the B^0-$\overline{B}^0$ system [DON87], and a successful experiment may be done with a new facility dedicated to the B-meson physics, or with a "B-factory".

1.3 T-Invariance in Nuclear Physics

Among the most sensitive tests of T-invariance in nuclear structures are the correlation experiments involving nuclear radiation. One of the most precise measurements of that kind was made on the emission of γ photons from ^{131}Xe [GIM82], the transition being due to both electric quadrupole (E2) and magnetic dipole (M1) radiations. They measured angular distribution and polarization of the emitted γ photons in order to determine the correlation with T-odd combination of the variables,

$$(\vec{J} \cdot \vec{k} \times \vec{e})\,(\vec{J} \cdot \vec{k})\,(\vec{J} \cdot \vec{e}), \tag{1.16}$$

where $\vec{k}$ and $\vec{e}$ are the vectors along momentum and polarization, respectively, of the photon and $\vec{J}$ is the nuclear spin in its initial excited state which could be reversed by flipping external magnetic field. The size of this correlation could be related to the phase offset η between the amplitudes of the two competing modes, E2 and M1. T-invariance requires

them be relatively real - i.e. phase difference of 0 or π in which case the correlation is zero. Interpretation of this type of measurement was complicated because the final state interactions, which conserved T-invariance, could also introduce a similar phase shift ξ. The upper limit set on η after correcting for ξ was 1.1×10^{-3}, and it is most naturally related to the degree of T-violation in either the electromagnetic or strong interaction of the nucleus.

One can also measure similar T-odd correlations in β decay to look for T-violation in the weak interaction. Hallin and others made such a measurement to set a limit on the angular correlation

$$\vec{J}_{Ne} \cdot (\vec{P}_e \times \vec{P}_\nu) \tag{1.17}$$

in the decay $^{19}\text{Ne} \rightarrow ^{19}\text{F} + e^+ + \nu$ [HAL84]. Their null result was consistent with T-invariance of the process to the level of 0.8×10^{-3}.

In a different, somewhat direct, approach one can measure forward and backward cross sections of a nuclear reaction to test the principle of detailed balance. The result of such a measurement is conveniently parameterized by the asymmetry

$$\Delta = \frac{[\sigma(\text{forward}) - \sigma(\text{backward})]}{[\sigma(\text{forward}) + \sigma(\text{backward})]/2'} \tag{1.18}$$

which is proportional to the ratio of the T-violating and T-conserving amplitudes in the process. One of the most studied reactions in this regard is $^{27}\text{Al}(p,\alpha)^{24}\text{Mg}$ and its inverse; Blanke and others reported $\Delta < 0.51\%$ which set the limit on the ratio less than 5×10^{-3} [BLA83]. In a variation of this approach one can measure the left-right asymmetry of scattered particles when an incident beam is spin polarized, and compare it with the induced polarization measured as a function of scattered angle in an inverse reaction. The reactions $^7\text{Li}(^3\text{He}, p_{\text{POL}})^9\text{Be}$, $^9\text{Be}(^3\text{He}, p_{\text{POL}})^{11}\text{B}$ and their inverse reactions were studied in search for T-violation in a series of experiments. After a short-lived claim that new evidence for T-violation was found [SLO81], T-invariance in those nuclear interactions was restored by subsequent experiments [HAR82, TRE84].

All of the measurements discussed above set the upper limits at the level of 10^{-3} to 10^{-4} on the T-violating parameters in the nuclear reactions. While these limits are small, they are by no means as small as those obtained from measurements of permanent electric dipole moments of particles and atomic systems.

1.4 Time Reversal and Electric Dipole Moment

1.4.1 EDM as an Evidence of T-Violation

Suppose a particle like a neutron or an electron has an electric dipole moment (EDM), $\vec{d}$. Then for the new moment not to introduce an extra degree of freedom its direction must be fixed to the existing axis of the particle, namely the spin $\vec{\sigma}$, i.e.

$$\vec{d} = g_d \vec{\sigma}, \tag{1.19}$$

where g_d is an electric analogue of a gyromagnetic ratio. Otherwise two possible orientations of the EDM will allow the particle to have four different states, which is in serious contradiction with our understanding of matter based on the exclusion principle. The importance of such a moment lies in that its very existence is in violation of T- and P-invariances. As can be seen in Figure 1.1, where the EDM $\vec{d}$ and the angular momentum $\vec{\sigma}$ are assumed to be parallel in the real world, the two moments in the time-reversed or mirror-imaged world are antiparallel. Thus by observing the relative directions of the two moments one can tell the sense of progression in time or the handedness of the reference frame: a definite sign of breakdown of the symmetries.

Formally, the origin of P- and T-violations associated with the EDM can be traced back to different transformation properties of the two vectors, $\vec{d}$ and $\vec{\sigma}$. The former is a polar vector while the latter is an axial one,

$$P\vec{d}P^{-1} = -\vec{d} \tag{1.20.a}$$

$$P\vec{\sigma}P^{-1} = \vec{\sigma}, \tag{1.20.b}$$

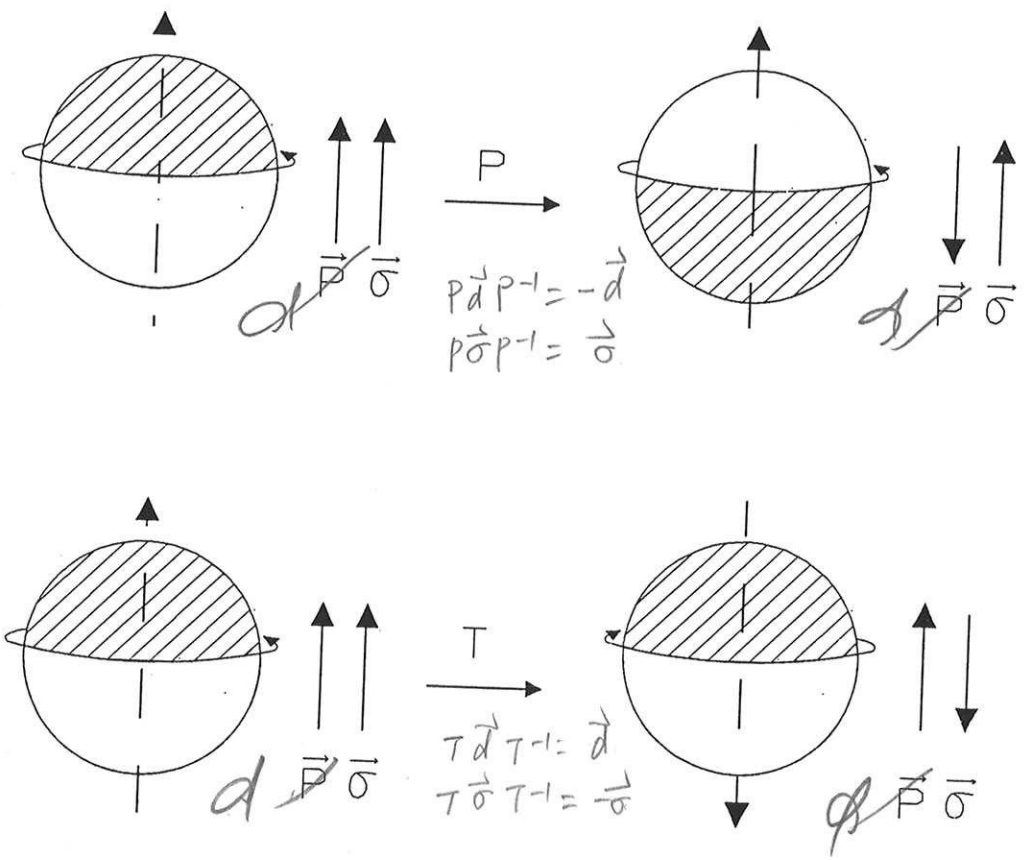

Fig. 1.1 EDM and P and T transformations

and under T

$$T\vec{d}T^{-1} = \vec{d} \qquad (1.21\ a)$$

$$T\vec{\sigma}T^{-1} = -\vec{\sigma}. \qquad (1.21\ b)$$

The transformation properties are compatible with the relation of Eq. (1.19) only if g_d vanishes.

Now generalizing the argument, if an atom or a molecule possesses a permanent EDM along one of its angular momenta then P- and T-invariances are violated in the system. Such a moment would appear as a linear Stark shift changing signs for opposite orientations of the angular momentum. For a composite system like atoms or molecules one can imagine various T-odd mechanisms that can induce the EDM, and a measurement of the moment is sensitive to parameters characterizing them. An important question arises, however, when an EDM is carried by one of its constituent particles, either the electrons or the nucleons, concerning the measurability of such a moment. As was first formulated by Schiff [SCH63], even if a charged point particle in an electrically neutral system has a permanent EDM there is no Stark interaction first order in the dipole moment because total electrostatic force on the particle should vanish in equilibrium. The crucial assumption here is the particle being a point, and for a nucleus with a finite size there can be relative displacement between dipole and charge distributions that allows the nuclear electric dipole interaction big enough to be observed. It was also pointed out by Schiff that when the particle has magnetic interactions as well there is no need for the electrostatic force alone to vanish, and the consequent unbalance in the electric part can lead to a shift first order in the EDM. When these effects are considered in a relativistic situation of a heavy, many-electron atom, the atomic EDM can even be greater than that of an electron by a large factor. Sandars estimated such enhancements for alkali atoms [SAN68] and Thallium atom [SAN75], and similar effects regarding TlF molecule have been noted [SAN67].

Whether it is a simple particle or a composite system, in an experimental search for its EDM one looks for a P- and T-odd Stark interaction,

$$H' = -\frac{d}{\mathrm{J}}(\vec{\mathrm{J}} \cdot \vec{\mathrm{E}}), \tag{1.22}$$

where $\vec{\mathrm{J}}$ is the angular momentum along which the EDM is supposed to lie, $\vec{\mathrm{E}}$ is the applied electric field and d characterizes strength of the EDM or degree of T-violation in the system.

Before describing the experiments to measure an EDM it is worth noting that an electric dipole moment in the context of P- or T-violation should be distinguished from that associated with degenerate levels. As an example, considering two close levels that have opposite parities the Stark shift is

$$W = \pm\sqrt{(\Delta\omega)^2/4 + |v|^2}, \tag{1.23}$$

where $\Delta\omega$ is a separation between the unperturbed pair, and v is proportional to the applied electric field strength,

$$v = \vec{\mathrm{E}} \cdot \langle \Psi_1 | e\vec{r} | \Psi_2 \rangle. \tag{1.24}$$

If $\Delta\omega$ is larger than $|v|$, the leading term in an expansion of the shift is quadratic in the electric field and the dipole is said to be induced. On the other hand, if $|v| \gg \Delta\omega$ the Stark shift is linear in $|\vec{\mathrm{E}}|$ and in a rough terminology the system has a "permanent electric dipole moment". Obviously it is only a matter of relative magnitudes of the two energy scales and in either case there is no part of the normal Stark shift that depends on the sign of $\vec{\mathrm{J}} \cdot \vec{\mathrm{E}}$.

1.4.2 Measurements and Predictions on neutron EDM

Even before the parity violation was discovered, Purcell and Ramsey stressed importance of measuring permanent EDMs in order to test the validity of symmetry principles [PUR50]. Their first measurement on a neutron EDM was made by the beam magnetic resonance method, and its result was $d_n = (-0.1 \pm 2.4) \times 10^{-20}$ ecm [SMI57]. The neutron

was chosen for its electrical neutrality which made the dipole interaction the leading one in its electrostatic potential, and also for its known participation in electromagnetic, weak and strong interactions. In the experiment, spin polarization and its analysis were made possible by the spin-dependent reflection of the neutrons from magnetized surfaces. The neutron spin flip was induced by separated oscillatory magnetic fields (§§ 2.7.5), while the neutron was under the simultaneous influence of electric and magnetic fields,

$$H = -\vec{\mu}_n \cdot \vec{B} - \vec{d}_n \cdot \vec{E}. \tag{1.25}$$

A shift in the resonance frequency accompanying a reversal of the electric field was to be interpreted as resulting from the neutron EDM.

Over the next 20 years basically the same technique was perfected in a series of experiments to set the number $d_n = (0.4 \pm 1.5) \times 10^{-24}$ ecm [DRE77]. It was difficult to make further improvement on the beam resonance method because the short transit time (about 10 msec) of a neutron beam through a transition region produced a linewidth of order 100 Hz while the limit on d_n corresponded to 0.1 mHz. The measurements also suffered from a systematic effect due to the motional magnetic field, $\vec{v} \times \vec{E}/c$ which changed direction upon an electric field reversal and induced the frequency shift mimicking T-violation. Both the problems were nicely solved by introducing the new technique of storing the ultra cold neutrons in a bottle. It was known that when incident velocity of a neutron was less than 7 m/sec, the neutron could make a total reflection from a suitable wall without a spin relaxation, and could evolve coherently for a long period time. Also for trapped particles the average velocity vanishes and there can be no significant $\vec{v} \times \vec{E}$ effect. With the large output of the neutrons from a modern reactor and the proper moderators to slow them down, enough flux of the particles at such a low velocity became available and storage experiments were performed. The results from the two competing groups at Grenoble [SMI90] and at Leningrad [ALT87] are

$$d_n = (-3 \quad \pm 5 \quad) \times 10^{-26} \quad e\text{cm} \tag{1.26.a}$$

$$d_n = (-1.4 \pm 0.6) \times 10^{-25} \quad e\text{cm}, \tag{1.26.b}$$

respectively, the latter being interpreted as $|d_n| < 2.6 \times 10^{-25} e\text{cm}$.

Although a non-zero EDM from the neutron has not been found yet, the present upper limit provides significant tests for the theories devised to account for the kaon data. For an example, if we make an order of magnitude estimate of d_n based on a milliweak interaction

$$d_n \sim e \times l \times f, \tag{1.27}$$

where l is a length representing weak interaction in the neutron, and f is a degree of T-violation which we take to be 10^{-3}. Putting $l = G_F M_n$ ($\hbar = 1, c = 1$), where G_F is the Fermi constant and M_n the neutron mass, we get $d_n \sim 10^{-22} e\text{cm}$ which is at least three orders of magnitude larger than the experimental limit. Similarly, many early models were ruled out for their incompatibility with the neutron EDM [DRE77]. A model that is currently under experimental attack is the one due to Weinberg with three Higgs bosons. In that theory the EDM is induced from the first order effect via virtual Higgs exchange and generally d_n is predicted to be around $10^{-25} e\text{cm}$ [BEA83], although there are estimates running as high as $10^{-22} e\text{cm}$ [ANS84]. On the other hand, the KM model sets the number below $10^{-30} e\text{cm}$ down to $10^{-33} e \cdot \text{cm}$ - e.g [KHR82]. It is so small because the CP-violating phase in the model is related to the heavy quarks whereas the neutron is composed of light ones. The predictions from the superweak model are also at the level of $10^{-30} e\text{cm}$ or below. We note that, in general, predictions of the neutron EDM based on any model have large uncertainties and they can be taken only as order-of-magnitude estimates.

The limit on the neutron EDM has a different implication for strong interaction. CP-violation in QCD is characterized by the free parameter $\bar{\theta}$ that labels its vacuum, and its relation to d_n has been calculated by many researchers [BAR89]; generally

$$d_n \sim \text{a few} \times 10^{-16}\,\bar{\theta}\; e\text{cm}. \tag{1.28}$$

It follows from the limits in Eq. (1.26) that $\bar{\theta}$ is forced to be less than 10^{-9}. While there are other measurements related to the $\bar{\theta}$ parameter, the neutron data puts the most stringent limit on it. In fact such an extremely small limit has raised question of its "naturalness" and some theories introduced a new type of symmetry (Peccei-Quinn symmetry) to make it vanish naturally. In any case the present limit of 10^{-9} to $\bar{\theta}$ makes it an unlikely reason for the CP-violation in the kaon decay.

1.4.3 Measurements and Interpretations of Atomic EDM

Atoms or molecules are interesting systems to look for T-violation because they are composite ones of electrons and nucleons, and those particles are participating in various interactions - electromagnetic, weak and strong. Results from an atomic EDM measurement can be used to put upper limits on either the EDM's of the constituent particles or strengths of T-odd interactions among them [HIN89]. In this way the electron EDM can be measured using atoms with nonzero electron spin angular momentum and the proton and neutron EDM can be deduced from atoms in which the nucleus has non-zero spin. T-odd weak couplings of scalar and tensor interactions among electrons and nucleons can also be measured from atoms and molecules.

Cesium was the first atom to be studied extensively in search for an atomic EDM. The main interest was in the EDM of the electron d_e which, through relativistic effects, should produce a much larger EDM of the atom [SAN68],

$$\frac{d_{Cs}}{d_e} \cong 130. \tag{1.29}$$

A series of atomic beam magnetic resonance experiments were done by a group at Brandeis [SAN64, STE67, CAR68, WEI68]. In those measurements, transitions between ground state Zeeman sublevels were induced by the separated oscillatory fields (SOF)

technique in the presence of an applied electric field. A change in the resonance frequency was looked for when the applied electric field was reversed. As was the case with the neutron beam experiment, these early attempts suffered severely from the $\vec{v}\times\vec{E}$ effect, and they had to run a beam of sodium simultaneously with the cesium to estimate the correction for the effect. In doing so they measured the difference between the atomic EDM's of sodium and cesium. Based on the nonrelativistic nature, and hence the small enhancement factor d_{Na}/d_e, of the sodium atom the comparison led to information on the electron EDM. This approach was successful until the experimental sensitivity began to be dominated by uncertainties in the comparison - e.g. uncertainties in the velocity distributions of the two beams - and set the final limit of $3\times10^{-24}e$cm.

To get around the problem Sandars suggested the study of an atom with large tensor electric polarizability [PLA70]. For such an atom relative Stark shifts among magnetic sublevels can be so large that a pair of states with the same $|M_J|$ - absolute magnetic quantum number - form a two level system well separated from other pairs. For $M_J=\pm1$ states, then, coupling due to a component of magnetic field perpendicular to the electric field is of second order, and the effects of motional magnetic field can be greatly suppressed. (In the TlF experiment the $\vec{v}\times\vec{E}$ effect is also negligible. See §§ 3.4.2) The xenon atom in $^3P_2$ metastable state was a good candidate for its highly polarizable electron in an open shell. It also had a large relativistic enhancement factor comparable to that of the Cs. But the experiment was not free from other spurious effects, which forced the comparison with the krypton beam and the improvement on the limit to d_e was marginal.

As in the neutron work, atomic experiments finally gave way to the storage technique, and a new method was introduced to make measurements on atomic vapors trapped in a cell [VOL84]. The basic ideas in an EDM measurement, however, remain the same: polarize a spin, let it precess under the influence of electric field for a while, and measure the precession angle by analyzing the spin. In a cell experiment the spin polarization is

established by optical pumping and usually two or more cells are stacked up with electrodes in between them so that the field directions are opposite in one cell from another. Spin analysis is then made by observing absorption of polarized light by the vapor.

First measurement using the new technique was made on the $^1S_0$ ground state of the ^{129}Xe atom [VOL84]. In this experiment, interaction of the xenon vapor with pumping light was mediated by the rubidium atoms via spin exchange. Precession of the xenon nuclear spin due to an EDM interaction with an external electric field was looked for. The spin relaxation time for the atoms were about 500 sec, and this long observation time made a very precise measurement of the Xe EDM possible:

$$d(^{129}\mathrm{Xe}) = (-0.3 \pm 1.1) \times 10^{-26}\, e\,\mathrm{cm}. \tag{1.30}$$

Unlike cesium or metastable xenon atoms, Xe atom in the ground state is diamagnetic - total electron spin angular momentum vanishes - and no new limit to the electron EDM was set by the measurement. Instead it was interpreted as limiting a short-range tensor-pseudotensor electron-nucleon coupling strength below $10^{-6}G_F$. Later the same technique was applied to the ^{199}Hg atom to measure its EDM [LAM87]. In the mercury experiment it was possible to polarize the ^{199}Hg nuclear spin by direct optical pumping. Once again the precession of the magnetization modulated the transmission of the pumping light. Two identical cells with sandwiched electrodes were employed to have opposite electric fields in them and the light beams through the cells were compared to extract the information on the electric dipole interaction. The measured atomic EDM,

$$d(^{199}\mathrm{Hg}) = (0.7 \pm 1.5) \times 10^{-26}\, e\,\mathrm{cm} \tag{1.31}$$

was interpreted as setting limits on the coupling strengths of possible T-odd electron-nucleon interactions of tensor and scalar natures and it also set limit on the electron EDM comparable to that from the metastable xenon experiment.

More recently the EDM of the Cs atom was also measured in a cell [MUR89]. The technique used in the experiment involved two lasers: one to polarize the spin by optical pumping, and another to probe its precession in an electric field. The two light beams (along $\hat{x}$ and $\hat{y}$) intersected at right angles and the electric field was perpendicular to them along the z axis to make the atomic EDM precess in the xy-plane. There was no magnetic field present in the apparatus. The probe beam was weak and its circular polarization was modulated rapidly to prevent it from pumping the vapor. Then the change in its transmission in phase with the modulation was a measure of the atomic precession, and hence its EDM. In practice an ambient magnetic field could induce the same effect, and for this reason, the signals from two cells under opposite electric fields were monitored to discriminate against it. The final number,

$$d(\mathrm{Cs}) = (-1.8 \pm 7.0) \times 10^{-24}\, e\,\mathrm{cm}, \tag{1.32}$$

was a factor of 50 improvement over the best limit from the beam experiments, putting the upper limit of $6 \times 10^{-26} e\,\mathrm{cm}$ on the electron EDM. Although the KM model predicts vanishingly small d_e, some of the gauge and supersymmetry models give larger estimates and the present limit from the cesium atom provides a significant constraint on them.

1.4.4 Experiments on Thallium Fluoride

Stimulated by the experiments on the neutron EDM, Sandars suggested a corresponding measurement of the proton EDM (d_p) using the molecule TlF [SAN67]. Being a polar molecule, TlF has a large electric polarizability and this made the system exceptionally sensitive to the nuclear electric dipole moments. That the thallium nucleus was heavy made the sensitivity even greater and because it had one unpaired proton the nuclear EDM could be readily related to the proton EDM. In practical considerations the TlF molecules were suitable for high-intensity beam work. Although the original motivation of a TlF experiment was to measure the proton EDM, later it was realized that the

molecule was very sensitive to various T-violating interactions between the nucleons and the electrons and also to the electron EDM (Chapter 4). It is these latter interpretations that are most significant.

The first experiment with the molecular beam resonance technique [HAR69] set a limit of $9 \times 10^{-20} e$cm on d_p setting the stage for a series of such measurements. The experiment repeated at Oxford with a very long beam machine yielded about the same sensitivity in spite of its narrow linewidth because there was an unexpected drop in signal strength [HIN80b]. The third measurement was carried out by the group of Ramsey with an improved source and a focussed beam [WIL84]. Although they greatly improved the ratio of signal to noise, there was an uncontrollable instrumental effect associated with the method of polarizing the nuclear spins and they could not take full advantage of the increased signal strength. Still they were able to improve the Oxford number by factor of 4. Beginning from 1983 a beam machine dedicated to the TlF experiment was built at Yale with the hope of making a highly sensitive measurement without the systematic effects that limited the previous undertaking. The first result from the new machine was indeed free from an instrumental effect and only limited by beam statistics, and it provided roughly five times smaller limits on T-violation in the TlF molecule [SCH87]. Naturally it was followed by the efforts to improve the signal to noise ratio and make even more precise measurement and that is the work reported here [CHO89].

1.5 Outline of TlF experiment

In this section a brief description is given of how we tried to measure T-violation using thallium fluoride molecules. Only the essential features are discussed and detailed descriptions of each aspect of the experiment are reserved for the following chapters.

In our experiment, a molecular beam resonance technique was employed to observe the Tl nuclear magnetic resonance (NMR) in the presence of an applied electric field $\vec{E}_C$. The aim was to measure an electric dipole interaction, if existing, of the Tl nuclear spin ($\vec{\sigma}$)

with E_C. The applied electric field polarizes the molecule by aligning its internuclear axis. Any dipole moments associated with the nuclear spin can then interact with the internal field which, due to the symmetry of the diatomic system, is along the internuclear axis. In this picture the effective Hamiltonian can be written as

$$H_{PT} = -dh\,\vec{\sigma}\cdot\hat{\lambda}, \tag{1.33}$$

where $\hat{\lambda}$ is a unit vector pointing from the Tl nucleus to the F nucleus, d is a measure of T-violation in TlF, and h is Planck's constant. We note that according to the Schiff's theorem, for a point-like nucleus there is no such effective interaction but in fact it can occur because of the finite volume of the Tl nucleus. The effect of H_{PT} is to appear as a frequency shift in the Tl NMR when the electric field, and hence the unit vector $\hat{\lambda}$, is reversed with respect to the quantization axis of the spin.

Thallium fluoride is a diatomic molecule and both Tl and F nuclei have spin of 1/2, and consequently it has complicated structure of vibration, rotation and hyperfine levels, even when it is in the electronic ground state ($^1\Sigma$). The measurement is done on one of the hyperfine levels within the electronic and vibrational ground state, which is most stable and populous under the experimental conditions. The first excited rotational state is used because it is the least complicated one which can make the experimental scheme work. For a given hyperfine level the Tl NMR was induced by separated oscillating magnetic fields to produce a narrow linewidth with convenient lineshape for the EDM measurements. This NMR region, which is traditionally called the C region, takes up more than half the length of the beam machine in order to make the resonance line as narrow as possible.

For the nuclear magnetic resonance to appear as a detectable signal, a population difference between the two levels - spin up and spin down - of the NMR should be established before the C region and also there should be a means to probe the nuclear spin state afterward. In other words, we need mechanisms for state selection and polarization detection. In the experiment these were done by a pair of electrostatic quadrupoles in cooperation with so called state selectors (Figure 1.2). The quadrupoles are basically regions of electric

field gradient, and due to the Stark effect, molecules in different rotational states experience different forces while passing through them. The specific configurations of the quadrupole fields are such that those in the $|J=1, M_J=0\rangle$ states will get focussed, while $M_J=\pm 1$ states are defocussed, where J refers to the rotational angular momentum. The idea is analogous to the gradient force on an electron magnetic dipole moment in a Stern-Gerlach apparatus, except that the quadrupoles in our machine are electrostatic and cannot distinguish molecules with different magnetic states.

Magnetic state selection is done inside the state selector where the molecule is subject to a magnetic as well as electric field, and all the hyperfine levels with different nuclear spin orientations are resolved. An oscillating field inside the state selector now drives a transition from one of the focussed states to a single hyperfine level in the set of defocussed rotational states, and thereby selectively populate a particular state with Tl nuclear spin pointing in one direction. The nuclear magnetic resonance is targeted on that state. After the NMR region a second state selector checks whether the spin was flipped by inducing the same transition. That puts those that survived the NMR back to the original focussable states. Those that actually changed their Tl nuclear spin states are not affected by the second state selector, and being a member of the defocussing set it cannot get to the detector. The transitions in the state selectors are sometimes called subsidiary resonances and the whole strategy is known as a triple resonance scheme.

The experiment then consists of inducing and comparing the NMR transitions with the electric field ($\vec{E}_C$) either parallel or antiparallel to the magnetic fields of the state selectors which serve as spin quantization axis. In terms of the Hamiltonian $H_{PT} = -dh\vec{\sigma} \cdot \hat{\lambda}$ the E field reversal amounts to flipping the vector $\hat{\lambda}$, which changes the signs of the contribution from H_{PT} to the NMR frequency. On the other hand, T-conserving part of the NMR frequency can be effectively described by $H = -\mu_{Tl}\vec{\sigma} \cdot \vec{B}_O$, where μ_{Tl} is the magnetic dipole moment of the Tl nucleus and $\vec{B}_O$ is the internal magnetic field. This observation leads us to another way to detect the T-violating Hamiltonian; we may reverse $\vec{B}_O$ by reversing the

magnetic fields in the state selectors. A third possibility is tuning the state selectors to a different transition so that a state with reversed angular momenta, and hence reversed $\vec{B}_o$ is selected (§§ 3.1.2).

CHAPTER 2

APPARATUS

A new machine was built from scratch to measure the electric dipole moment of a TlF molecule and a detailed description of the apparatus was already given [SCH88]. A few significant changes , however, have been made to the machine over the last two years and those improvements made it possible to measure the EDM with ten times better sensitivity. In this chapter the machine and physical ideas underlying its design are described with more words devoted to the new features.

2.1 Beam Machine

2.1.1 Overall Construction

The beam machine is 5.3 meters long and consists of three differentially pumped regions: a source chamber, a main beam line and a detector chamber. The machine is sitting on two carts which can move on rails independently. The source and the detector chambers are made of type 304 stainless steel, and both are connected through necks to the main beam line. The main beam line itself has T-shaped chambers made of aluminum at both ends to house the electrostatic quadrupoles, with a 3.0-meter long Pyrex tube for the main resonance region in the middle. In between the long tube and the quadrupole chambers are octagons that have feedthroughs for electrical connections. Figure 2.1 and Table

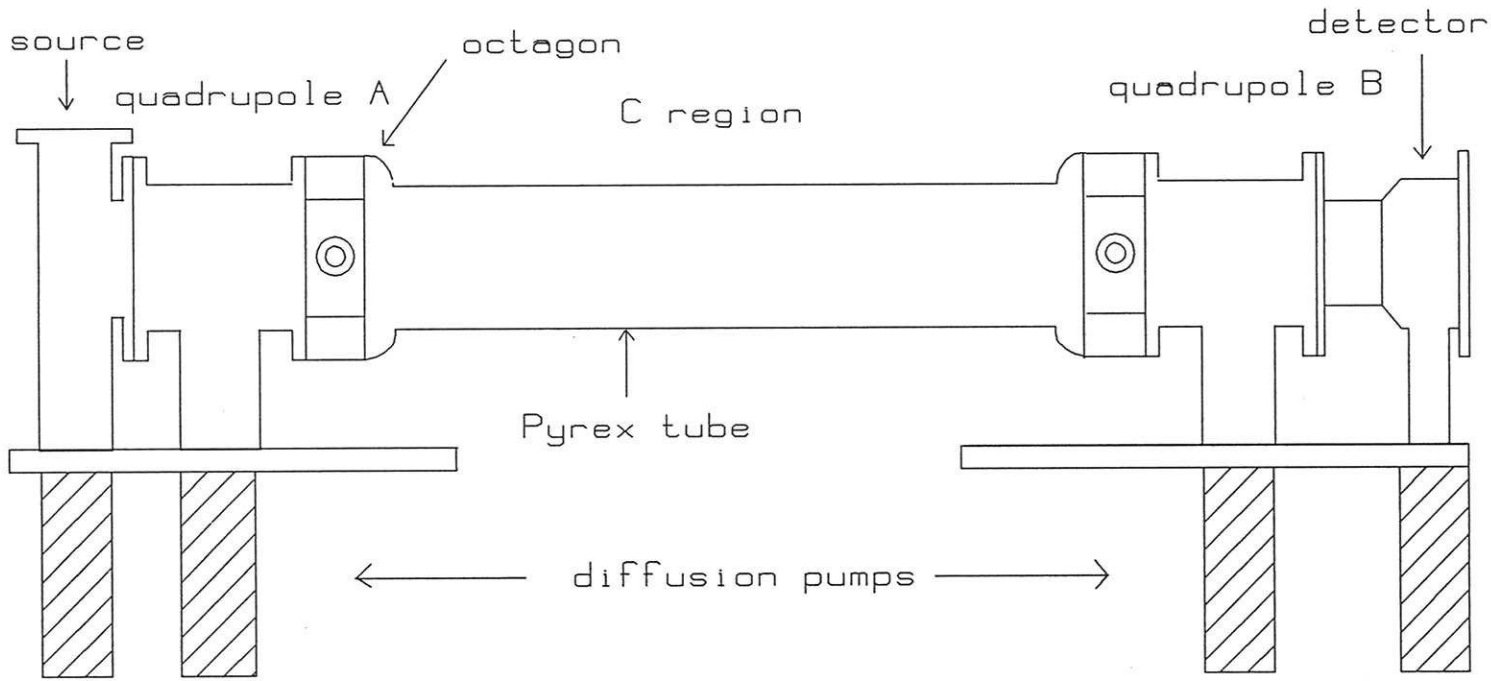

Fig. 2.1 Schematic of beam machine

a) Axial Dimensions

distance from source hole to skimmer hole	0.4 cm
distance from source hole to quadrupole entrance	24.0 cm
length of quadrupole	60.0 cm
distance from quadrupole exit to state selector entrance	4.0 cm
length of state selector	24.0 cm
distance from state selector exit to C plates	6.0 cm
length of C plates	245 cm
distance between two SOF coils	215 cm
distance from source hole to detector	481 cm

b) Radial Dimensions

diameter of source hole	0.5 mm
diameter of skimmer hole	1.5 mm
diameter of quadrupole rod	35.0 mm
diameter of entrance circle of quadrupole	23.2 mm
distance between state selector electrodes	24.0 mm
distance between C plates	20.0 mm
diameter of beam stop	2.4 mm
diameter of effective detector area	2.5 mm

Table 2.1 Dimensions of the beam machine

2.1 give the schematic and dimensions of the machine.

2.1.2 Pumping Systems

Under running conditions the pressures inside the source and detector cans were generally higher than it was in the rest of the machine. To keep the pressure in the main beam line, where TlF molecules spent most of their time, as low as possible the three parts of the machine were differentially pumped. Each part was pumped by its own diffusion pumps and was separated by a baffle with a hole of 1.2-cm diameter which limited gas conductances. Each of the source and the detector cans was pumped by a 15.2-cm diameter diffusion pump (Innotech R620) and the main beam region was pumped by two 10.2-cm diameter ones (Innotech R420) placed under the quadrupoles. The butterfly valves installed between the differentially pumped regions sealed one from another so that each of them can be vented and maintained without disturbing other parts of the machine. All the vacuum seals in the machine were made with Viton o-rings. The diffusion pumps were filled with Dow Corning 705 pump oil and backed by two mechanical pumps (Sargent-Welch 1402B) placed near the source and detector ends of the machine. They were properly interlocked against failures of cooling water or an excessive surge of the backing pressure. The source and the detector cans were also protected by automatic gate valves that would close when the backing pressure went above the preset threshold.

The pressure at the source can (P_{ss}) was monitored by a cold-cathode gauge because hot TlF vapor shortened a life of an ion gauge to a few months. For the main beam line it was measured with two ion gauges at the quadrupole chambers, (P_{sq} and P_{dq}). The pressure inside the detector can (P_{dd}) was also separately monitored with an ion gauge. When the machine was in operation, $P_{ss} = 3.0 \times 10^{-7}$ torr, and $P_{sq} = P_{dq} = 1.0 \times 10^{-7}$ torr. The pressure inside the detector can was raised to $P_{dd} = 3.0 \times 10^{-7}$ torr by leaking oxygen into the can to enhance the detecting efficiency (§ 2.3). Without the oxygen flow $P_{dd} = 5.0 \times 10^{-8}$ torr was

routinely achieved. After the machine was vented and exposed to the atmosphere and possibly made dirty from the handlings inside, it was baked at around 100 °C for a few days to bring the final pressure down and also to reduce the frequency of pressure bursts.

2.2 Source

All of the previous experiments on TlF looking for a T-violation were done with an effusive source. The present experiment used a jet source and this was the most remarkable difference of this project compared with the old ones. The idea of developing a jet source to produce a high-intensity and low-temperature beam has been considered for the TlF experiment since the experiment was first conceived. However, the adoption of a jet source became essential only recently after more pressing technical and systematic problems were solved by previous workers. In the application of the jet beam technology to our experiment, there are three major characteristics of a beam to be considered: local temperature of the beam (thermodynamic properties), velocity distributions and total flux (kinematic properties), and the ratio of monomers to dimers (chemical compositions). These are the factors that can directly affect the sensitivity of the EDM measurements. In this section we discuss the basic physics of a jet beam with special attention to these parameters. The constructions and the operation of the source are also described.

2.2.1 Thermodynamic and Kinematic Properties of a Beam

A source is called effusive when the mean free path (l) of a molecule inside an oven is large compared with a typical linear dimension (d) of its exit hole. In that case a molecule in the source escapes through the hole only by chance, and the beam out of it reflects the thermodynamic states of the molecules in the source exactly except for some kinematic factors. On the other hand, when the vapor pressure inside a source is large enough, the mean free path can be much smaller than a diameter of the exit hole and the molecules are

actively pushed out of the source. Under this condition it is called a jet source and the emerging molecular beam mostly "remembers" how it was pushed out rather than how the molecules in the source were thermally distributed [PAU68].

The most significant thermodynamic effect of this jetting process is that the energy related to the random motion of the molecules is transformed into a collective and directed motion of the beam, i.e. a large part of the available energy appears in the form of center-of-mass motion. Now if we look at the beam in its center-of-mass frame, there is very little energy left for thermal randomness, and the result is that the beam velocity has gone up but locally the beam is colder than the oven from which it originated. This cooling effect can be considered quantitatively by a simple model. Suppose a group of molecules with molecular mass m emerge from a source at temperature T_o and pressure P_o into a region of low pressure through the constriction of a nozzle. After the steady state situation is established, the process is adiabatic (Joule-Thomson process) and the enthalpy is conserved [REI65]. For a single molecule the enthalpy is

$$h = e(T,P) + Pv, \tag{2.1}$$

where e is the energy of the molecule given as a function of temperature (T) and pressure (P), and v is the volume per molecule. Inside the source,

$$e(T_o,P_o) = c_v T_o \tag{2.2.a}$$

$$P_o v_o = kT_o, \tag{2.2.b}$$

with c_v being molecular specific heat at a constant volume, and

$$h_o = \frac{\gamma}{\gamma - 1} kT_o, \tag{2.2.c}$$

$\gamma = c_p/c_v$

$= 1 + k/c_v$

where k is a Boltzmann constant and γ is a specific heat ratio. After an expansion the gas has acquired kinetic energy in its center-of-mass motion along the beam axis with a new local temperature T_b, and its enthalpy is

$$h(T_b, P_b) = \frac{1}{2} m v_{CM}^2 + \frac{\gamma}{\gamma - 1} k T_b. \tag{2.3}$$

Requiring the conservation of enthalpy we obtain the relation,

$$\frac{\gamma}{\gamma - 1} k T_o = \frac{1}{2} m v_{CM}^2 + \frac{\gamma}{\gamma - 1} k T_b, \tag{2.4}$$

or equivalently,

$$T_b = \frac{T_o}{1 + \frac{1}{2} M^2 (\gamma - 1)}, \tag{2.5}$$

where $M = v_{CM}/\sqrt{\gamma k T_b / m}$ defines the Mach number. For a diatomic molecule $\gamma = 7/5$ - or 4/3 if the vibrational degree of freedom is included - and we can estimate how cold a beam is in comparison with the oven if v_{CM} is known.

In designing our jet source we relied on data from the jet beam experiments with diatomic molecules similar to TlF [REE77, BOR75]. Also we were guided by the empirical formula, originally obtained for argon [AND66]:

$$M_{terminal} = 1.17 Kn^{\frac{1-\gamma}{\gamma}}, \tag{2.6}$$

where $M_{terminal}$ is the final Mach number after a full expansion and Kn is the Knudsen number, l/d. In practice the application of Eq. (2.6) was not straightforward because the effective cross section of a strongly polar molecule like TlF can be substantially larger than one would simply estimate from its internuclear distance [TOE84].

We remark that if a molecule has an internal structure, each degree of freedom can have different temperatures because of the nonequilibrium nature of a jet expansion. The expansion is most effective in relaxing translational motions followed by rotational and then vibrational motions, a phenomenon known as a heat capacity lag,

$$T_{translation} < T_{rotation} < T_{vibration}. \tag{2.7}$$

To be accurate in characterizing a jet of TlF we need three temperatures, $T_{translation}$, $T_{rotation}$ and $T_{vibration}$. T_b in Eq. (2.4) can be considered as a suitably weighted average of them.

Having a cold beam of TlF is to our advantage in that it increases the number of molecules in the states that we perform the experiment on. TlF is a diatomic molecule with the rotational and vibrational levels from the internal motions described by the Hamiltonians,

$$H_{ROT} = hB\vec{J}^2 \tag{2.8.a}$$

$$H_{VIB} = (n + 1/2)h\nu_o \tag{2.8.b}$$

with B=6.69×10^9 Hz and $\nu_o = 1.43 \times 10^{13}$ Hz [HER72] - see Table 2.2 in §§ 2.6.1. Converted into temperatures hB corresponds to only 0.32 °K and $h\nu_o$ to 687 °K and while the experiment was done on the hyperfine levels of the first-excited rotational (J=1) and the ground vibrational state (n=0), at a typical oven temperature of 753 °K the fractional equilibrium population of those states is very low, less than one part in a thousand. The expressions for the fractional populations of each rotational and vibrational states at a temperature T are

$$P_J = \frac{N(J)}{N} = \frac{(2J+1)\exp(-hBJ(J+1)/kT)}{\sum_{j=0}^{\infty}(2j+1)\exp(-hBj(j+1)/kT)} \tag{2.9.a}$$

$$P_n = \frac{N(n)}{N} = \frac{\exp\left(-h\nu_o\left(n+\frac{1}{2}\right)/kT\right)}{\sum_{m=0}^{\infty}\exp\left(-h\nu_o\left(m+\frac{1}{2}\right)/kT\right)}. \tag{2.9.b}$$

Cooling in the rotational and vibrational modes can push the thermal distribution in favor of the low-lying states and the useful fraction of a beam can thus be greatly enhanced.

The kinematic nature of a jet beam can be described by the two parameters v_{CM} and $T_{translation}$ that were among those introduced to characterize the thermodynamic state. Along the beam axis molecular speed increased by an amount v_{CM} in comparison with an effusive beam while both the axial and transverse velocities have a narrower dispersion of $\alpha=\sqrt{2kT_{translation}/m}$. When we define a differential flux $f(\vec{v})$ as the number of molecules emerging into a unit solid angle around $\vec{v}$ per unit time and exit area, it can be most conveniently expressed in cylindrical polar coordinates by

$$f(\vec{v})d^3\vec{v}=\frac{n}{\sqrt{2\pi^3}\alpha^3}v_z\exp\left[-\frac{(v_z-v_{CM})^2}{\alpha^2}-\frac{v_\rho^2}{\alpha^2}\right]v_z dv_z v_\rho dv_\rho dv_\phi, \qquad (2.10)$$

where n is the number of molecules per unit volume just inside the exit hole and the z axis is along the beam machine. The first factor is the molecular number density times the normalization constant and the factor v_z is from the usual cosine distribution of an effusion process. The Boltzmann factors reflect modified distributions of the velocities: the central value of v_z is shifted upward and the dispersions are squeezed (Figure 2.2.).

In terms of our EDM measurements, the new flux has mixed implications. The fast beam velocity is bad news in that we have larger linewidth in the Tl nuclear magnetic resonance and the focussing requires higher potential on the electrostatic quadrupoles. On the other hand, the narrow velocity distributions have positive effects. Axially it means the beam is monochromatic, and transversely the molecules are moving slowly and readily focussable. Another good feature of a jet beam in contrast to an effusive one is the higher intensity available. In general simply increasing an oven temperature does not generate correspondingly larger useful beam. Instead, one develops a cloud of molecules in front of the exit hole and its surface becomes the source of the beam. After collimations the number of those molecules into a correct solid angle remains about the same. For a jet source, however, the very mechanism of emitting beam and the subsequent directedness of it make

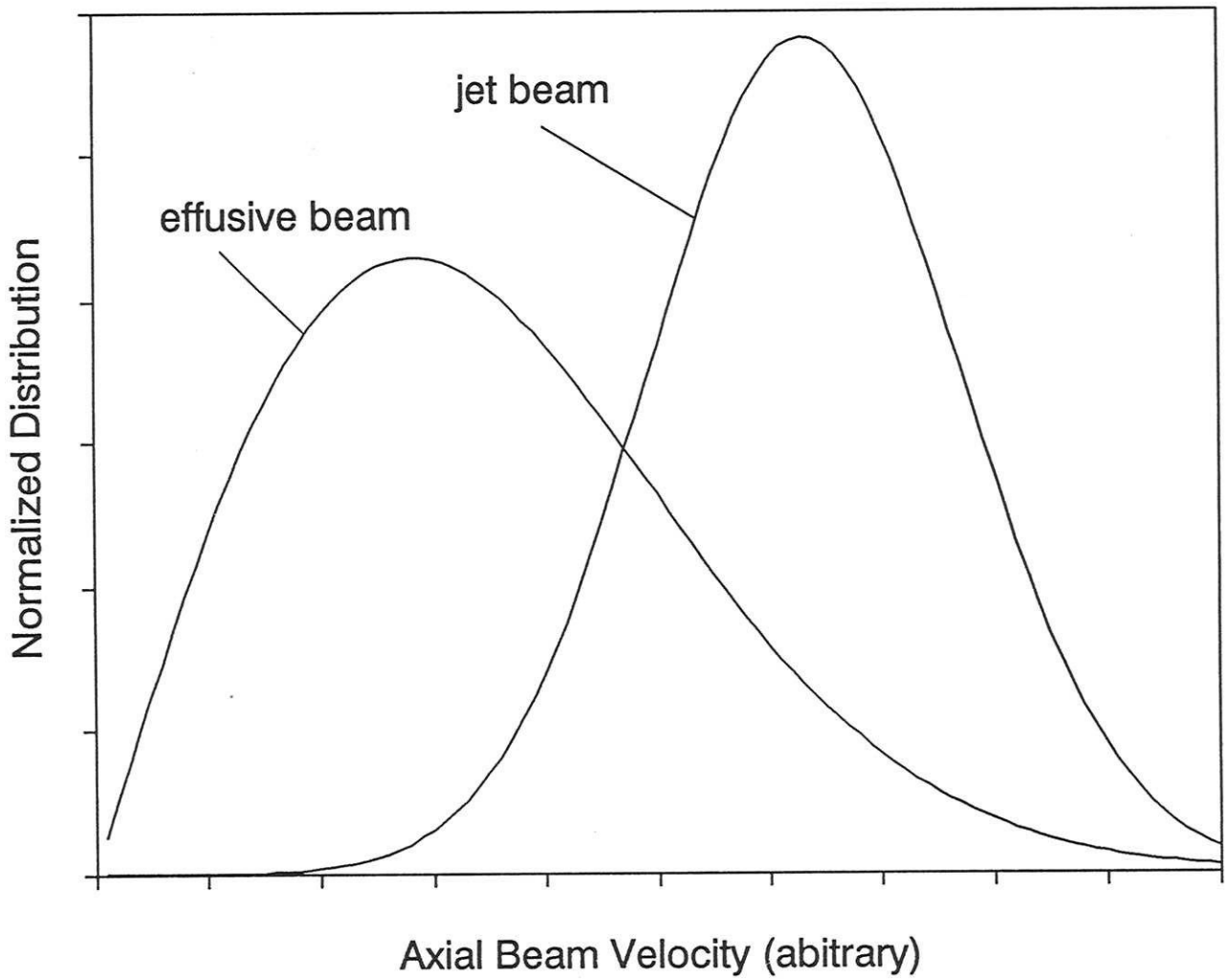

Fig. 2.2. Axial velocity distributuions of effusive and jet beams

substantial increase in the beam intensity easily achievable, provided that the unused portion of the output is properly pumped away. To get an especially high intensity, the outer part of the jet is removed by a skimmer before the molecules have a chance to be scattered by background gas.

In our apparatus the intensity is measured by allowing the beam to travel directly to the detector. This we call the full beam (FB). Hence from Eq. (2.10),

$$\mathrm{FB} = \int_{d\Omega} d^3\vec{v} A_{exit} f(\vec{v}), \tag{2.11}$$

where A_{exit} is the area of the exit hole and $d\Omega$ is the solid angle defined by the detector.

Another quantity of interest in this context is the total number of molecules coming out of the source per unit time - the total output (TO). This determines how frequently we have to refill the source or clean the machine, and

$$\mathrm{TO} = \int_{\text{forward}} d^3\vec{v} A_{exit} f(\vec{v}). \tag{2.12}$$

At the oven temperature of 753°K, the condition ($l \ll d$) was only mildly satisfied, yet we observed more than 50% drop in the beam temperature. The translational temperature was estimated by using the velocity distribution of Eq. (2.10). The most direct way to map out the distribution was to do the time-of-flight measurements, but lacking the gadgets to do the job in our machine, we used the velocity-selective nature of the focussing quadrupoles (§§ 2.5.5). In this sense the quadrupoles worked as a variable velocity filter, whose window could be moved around by changing the applied potentials. For a given potential the center of the window was known to us both from computer simulations and from the measured linewidth of the subsequent nuclear magnetic resonances. In this way we determined the velocity distribution - or the parameters v_{CM} and α

$$v_{CM} = 3.44 \pm 0.20 \times 10^4 \text{cm/sec} \tag{2.13.a}$$

and

$$\alpha = 1.50 \pm 0.12 \times 10^4 \text{cm/sec}. \tag{2.13.b}$$

which was interpreted as $T_{translation}=300\pm50°K$.

While the rotational temperature was the number of prime interest in terms of the sensitivity of our EDM measurements, it was also the hardest to estimate. $T_{rotation}$ Is usually measured by comparing the relative populations of two or more rotational levels [TSO79], and with our machine we could compare the numbers for J=1 and J=2. Unfortunately, because of the smallness of the spacing between rotational levels the ratio of their populations is not a very sensitive function of the temperature and it remains virtually the same from 200°K to 800°K. The situation is much better for the vibrational temperature, for a vibrational excitation takes much larger energy. The Tl nuclear magnetic resonance of our machine could resolve the lines from different vibrational levels (§§ 2.7.7), and comparing their strengths we concluded that $T_{vibration} = 400\pm50°K$. This estimate was complicated by the overlapping lines from the Tl isotopes. As a check we used this temperature to estimate the absolute strength of the NMR signal from the ground vibrational level and found good agreement with what we actually observed.

The temperatures we measured were consistent with the phenomenon of heat capacity lag, Eq. (2.7), and suggest that $T_{rotation} = 350\pm50°K$, which was also supported by the direct measurement of the J=1 population from the number of focussed molecules (§§ 2.5.5). Using T = 350°K as a representative temperature of the beam, the fractional population of ground vibrational and first excited rotational states was 2.36×10^{-3}, which was a factor of 3.0 improvement over the equilibrium value at the oven temperature of 753°K. One might expect that as the oven became even hotter, the beam would become colder and more intense and indeed the intensity vs. temperature curve fairly well followed the exponential growth of the vapor pressure as a function of temperature, but above 753 °K the fraction of molecules that participated in the main resonance became progressively smaller, indicating the onset of cluster formation. Because of this decline in the useful fraction, our measurements of the EDM were made at the relatively modest temperature of 753°K with the nozzle 20 to 30 °K hotter.

2.2.2 Chemical Composition of a Beam

The TlF vapor in the source exists mainly in two different forms: monomer and dimer. The vapor pressures for each species in equilibrium with liquid TlF at temperature T can be calculated from the formulas [KEN67],

$$\log(P_1) = -\frac{7325}{T} - 3.62\log T + 20.254 \qquad (2.14.a)$$

and

$$\log(P_2) = -\frac{7143}{T} - 5.55\log T + 25.881 \qquad (2.14.b)$$

where the pressures, P_1 for monomers and P_2 for dimers, are in torr, T is in °K and the log is to the base of 10. In fact, at our typical oven temperature of 753°K, this equilibrium partial pressure of dimers is twice of that of monomers. In the EDM measurement dimers are only spectators but they are doubly efficient in increasing the detected beam background. With either an effusive or a jet source many efforts have been made to obtain a better ratio of P_1 to P_2 than that dictated by the liquid-vapor equilibrium.

Breaking a dimer into two monomers is a heat-absorbing process and it also increases the total pressure by adding one more molecule. Hence the process is favored when temperature is high and pressure is low. In our previous effusive source the condition of low pressure was fulfilled by having a constriction between the lower chamber of liquid TlF and the upper one with the exit hole [WIL81]. For a jet source the situation can be potentially very bad [RYA84]. The beam is in the state of high density and low temperature which can foster formations of dimers or even clusters. However, to conserve momentum and energy, the formation of a dimer needs a three body collision which is far less frequent than the usual two body collisions. Because many two body collisions are all it takes to cool the beam, it is still possible to get a cold beam of TlF monomers with proper design and operation. Our design was a 30-cm long nozzle with heating wire wrapped around it [FEN87]. The separate heater for the nozzle made it possible to keep the gas

much hotter than the liquid TlF while the long path with a small cross section ensured that the molecular number density near the exit was significantly smaller than that was just above the surface of liquid TlF.

At 753°K the observed full beam was 1.3×10^{10} molecules/sec, and from the expression (Eq. 2.11), we infer that

$$n = 6.5 \times 10^{14} \quad \text{molecules/sec,} \tag{2.15}$$

assuming 90% detector efficiency. We note that this number density is about 1/100 of that in equilibrium with the liquid TlF. Given the total number density n, the partial pressures can be calculated from the chemical equilibrium constant $K_p(T) = (P_1)^2/P_2$ of the reaction

$$2(TlF) \Leftrightarrow (TlF)_2. \tag{2.16}$$

$K_p(T)$ is a function of temperature only, and its value can be obtained from the equilibrium vapor pressures in Eq. (2.14). In this way we obtain the number densities, n_1 for monomers and n_2 for dimers. When the nozzle is about 20°K hotter than the oven,

$$n_1 = 6.0 \times 10^{14} \text{molecules/cm}^3 \tag{2.17.a}$$

and

$$n_2 = 2.6 \times 10^{13} \text{molecules/cm}^3 \tag{2.17.b}$$

which means the monomer fraction, $r_m = n_1/n$, is 92 %. In above analysis we put $n = n_1 + 2n_2$ assuming the dimers have the same velocity distribution as the monomers.

An independent way to estimate n near the exit, and thereby calculate the number densities n_1 and n_2 is to use the transport theory of gas kinetics [ROT76]. When conductances C_1 and C_2 for the two species of TlF through the nozzle are given, n can be found by equating the rate of flow from the oven with the total output, TO,

$$C_1 n_1^{eq} + C_2 n_2^{eq} = TO, \tag{2.18}$$

where the superscript eq stands for the equilibrium value from Eq. (2.14). The flow regime of TlF gas through the nozzle is intermediate between that of molecular flow and viscous one, making the estimate difficult. We made calculations in the two extreme cases and they agree with that of Eq. (2.15) within a factor of 5.

2.2.3 Construction of a Jet Source

The source itself (Figure 2.3) consisted of a cylindrical container and a lid with the long nozzle attached to it. The container held 150 grams of TlF, which lasted for a few months under normal operation, and a flat surface on top of it made a breakable seal with a knife edge on a lid so that the source could be refilled a few times. The nozzle was made with a 30-cm long, 0.125-cm outside diameter standard (1/8") copper tubing. In order to make the nozzle, one end of the tubing was conically swaged until the hole was squeezed to close, and later it was cut to open to a desired diameter of 0.5 mm. All other parts were also made of copper, and the nozzle was soldered onto the lid with copper-silver alloy. Earlier attempts to make a source with either stainless steel or alumina(Al_2O_3) failed due to corrosion by the hot TlF. Heating was provided by two separate coaxial resistive wires (Amperex 1NCI10), each had resistance of about 20 ohms and were wrapped around the container and the nozzle. Temperature was monitored with two type K thermocouples placed near the bottom of the container (T_{liquid}) and on the nozzle (T_{gas}). T_{liquid} was used as a feed back information to stabilize the oven temperature to within one degree K. A corrugated piece of copper was also put in the container with TlF to spread the heat evenly, thereby suppressing local boiling and other violent eruptions of the liquid. In this way a very stable beam intensity was maintained for a long period of operations.

A loaded source complete with heaters and thermocouples and with its long nozzle shaped into a coil (Figure 2.3) was placed in a stainless steel jacket surrounded by with a few layers of blankets made of alumina fiber. The blankets were excellent thermal insulators with good vacuum properties and also held the source in position firmly. Finally the jacket was fixed to a brass rod from the top plate where the heat leaking out of the source

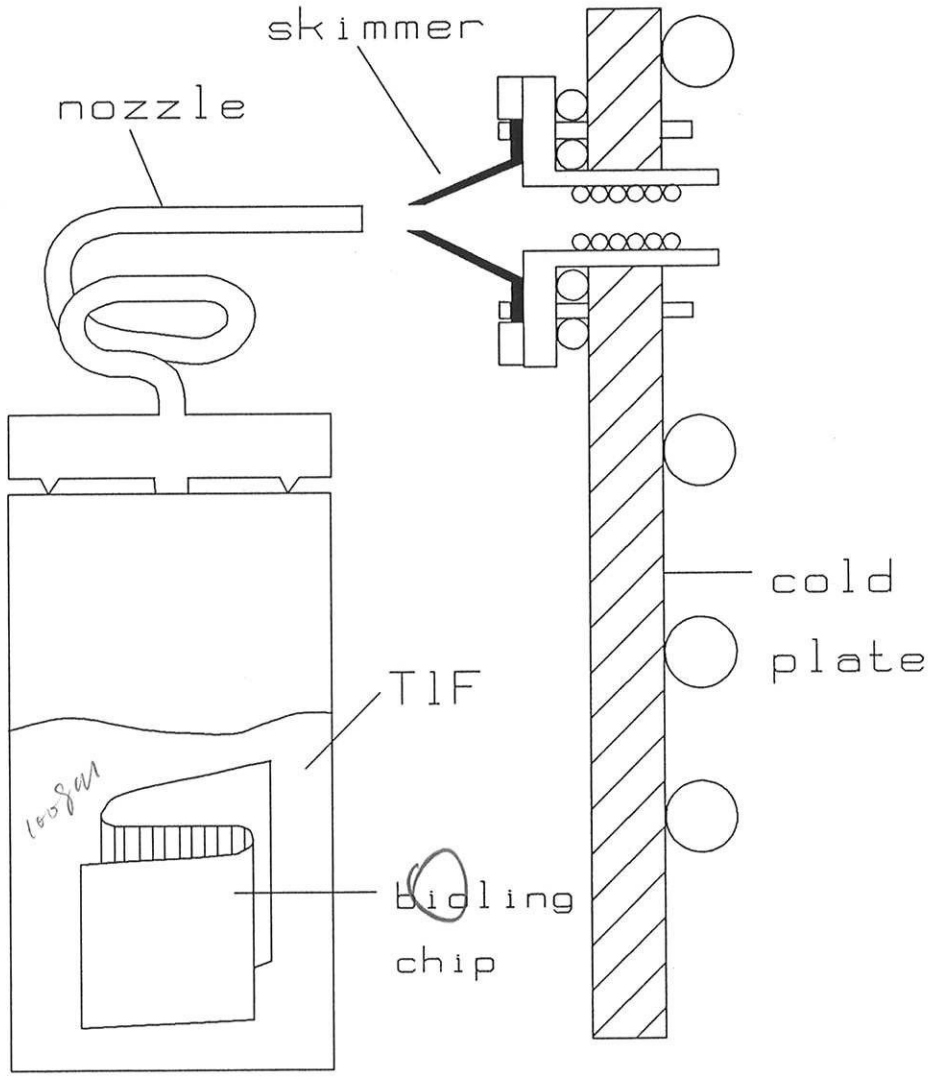

Fig. 2.3 Source and skimmer

was taken away by cooling water. The position and orientation of a nozzle tip can be completely specified by 5 parameters; 3 for the position of a hole and 2 for the orientation. Using the designs of a rotating flange and bellows we had external control of all the parameters. Those coordinates could be adjusted independently from one another, which made the fine adjustments in real operation straightforward.

Inside the source chamber, immediately downstream from the source hole, there was a skimmer mounted on a water-cooled plate. The skimmer was made by electroplating nickle onto a conical mold which was later machined to fit our system. It had a hole of 1.5-mm diameter which allowed only the core of a jet to go through. Most of the TlF molecules that hit the water-cooled plate were condensed there, maintaining a low background pressure in the source chamber. To prevent the skimmer hole from becoming clogged, a heater with proper insulation was placed between the cooled plate and the base of a skimmer holder. Under our operating condition, however, the presence of the skimmer did not make much difference in terms of the characteristics of the beam. It worked mainly as a collimator.

2.2.4 Other Techniques of a Jet Source

Two techniques commonly used in jet source applications are seeding a carrier gas [BEN78] and pulsing [LOV87]. In the seeding technique, a sample is mixed with a carrier gas, which is usually an inert gas such as argon. When it expands the carrier gas works as an effective coolant and it largely determines the beam velocity since the gas of interest generally makes up only a small fraction of the beam. Incidentally, the depletion of dimers in a seeded jet beam has been reported by some investigators [YAM81]. When we tried our prototype we injected variously argon, nitrogen or carbon dioxide gases into a source. It did not work to our specifications because the acceleration of the jet and the increase in the background pressure overwhelmed any positive effects. To avoid the excessive increase in the beam velocity, we could have tried heavier gas such as xenon, and to handle

the background pressure a new and more powerful pumping system could have been used. With the successful development of our unseeded source, however, this more radical modification of the apparatus was not pursued.

A pulsed jet beam makes the best sense when used in synchronously with a pulsed laser or when extremely high densities are required in a system of finite pumping speed. In our application there was no pulsed interactions and we were interested in the time-averaged intensity rather than the instantaneous peak value. Furthermore considering noise that might accompany pulsing we opted for continuous operation.

2.3 Detector

A hot, oxygenated tungsten filament (work function 6.4 eV) was used to detect TlF molecules by surface ionization The thallium ions are collected on a plate biased at -30 V relative to the ionizing surface. The collected charge is measured by an electrometer whose output voltage is then amplified and converted into pulses for a computer to read in (Figure 2.4).

To avoid the noise from potassium contamination, an inevitable manufacturing residue, an impurity-free filament was made by coating tungsten (produced by the decomposition of tungsten-hexacarbonyl, $W(CO)_6$) onto a hot tantalum substrate in an evacuated jar [GRE61]. A 2.5-mm wide and 65-mm long tantalum ribbon of 0.01-mm thickness was put on a holder under spring tension and placed in rough-pumped chamber containing solid $W(CO)_6$ and its vapor. As the coating proceeded, the current through the ribbon increased from 2.5 A to 10 A while the voltage was kept constant at 4.5 V and it took about 15 minutes for the process while the color of the ribbon changed from dull red to bright yellow. A finished filament was typically 0.08 mm thick. It was very brittle and the holder was installed in a detector can carefully.

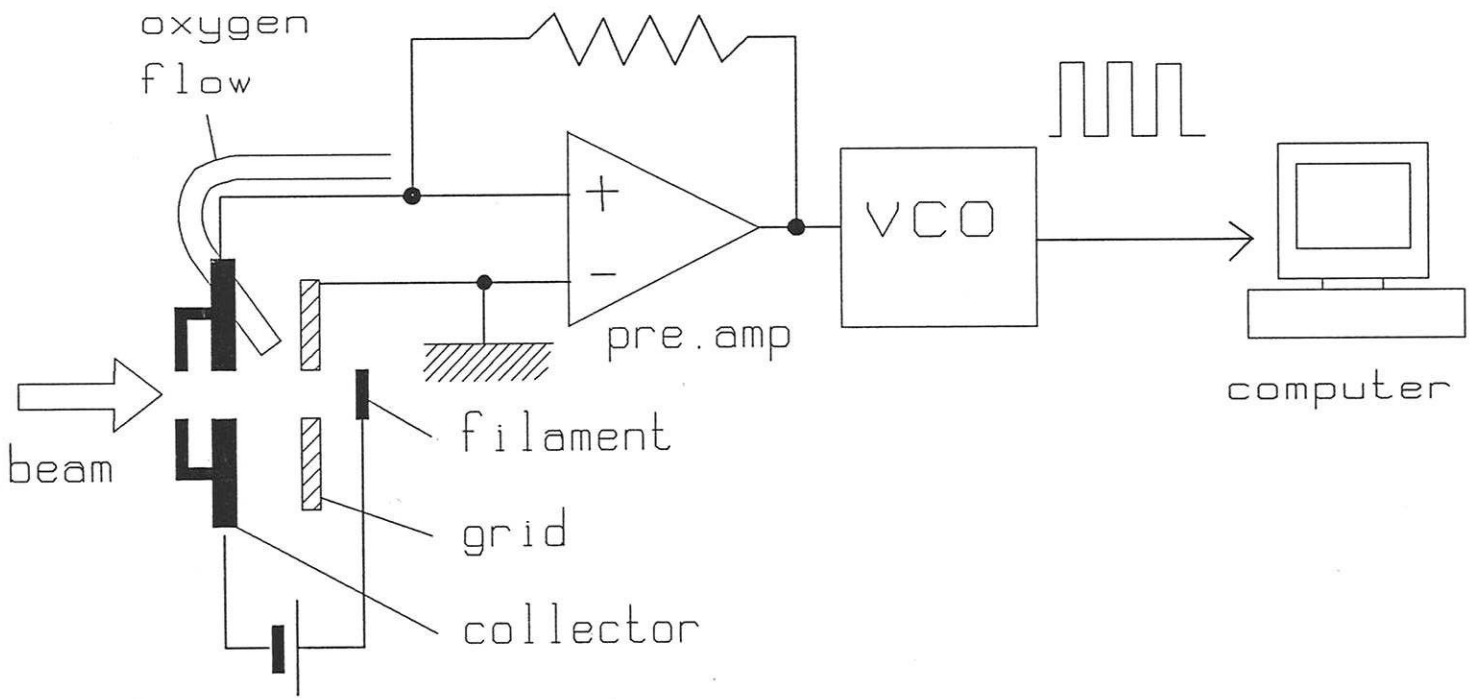

Fig. 2.4 Detector electronics

Immediately upstream from the filament a grounded grid with a hole of 3.5-mm diameter was placed to shield the collecting plate from the ions randomly emitted by the hot filament (Figure 2.4). The collector was placed 0.5 cm upstream of the grid and it was a 5 cm by 5 cm square copper plate with 2.5-mm diameter hole in the middle to admit the TlF beam. This hole defined the effective area of the detector. The whole assembly was on a board whose position in a plane transverse to the beam could be externally adjusted. To keep the surface of the tungsten filament oxygenated O_2 gas was introduced through a 3.2-mm diameter copper tubing aimed at the filament with its flow controlled by an external leak valve (Varian 951-5106). The collecting plate was connected to the electrometer through a coaxial cable and the collector and feedthrough were well insulated to prevent the accumulated charge from leaking out. The electrometer was a current-to-voltage converter consisting of a low-noise op amp (Analog Device AD515) with a 10^{10}-ohm resistor across it, and hence the conversion factor was 10^{10} volt/amp. Depending on the signal size, its output was further amplified with a gain of 1-100, and then digitized by a voltage controlled oscillator (Analog Device AD460) with a conversion factor of 100 kHz/volt. Most of the data was taken with the intermediate amplifier at the gain of 2 for which one pulse from the VCO corresponded to 3.1×10^3 ions on the collector. The VCO box was placed next to the electrometer to avoid an analog signal running a long distance.

To obtain a good detection efficiency and a low level of noise, heating current and oxygen flow were carefully optimized before each run. A filament worked best when it was kept red to orange (900 to 1000°C) by flowing 5 or 6 A of current through it. A large ion background was detected from a fresh filament even with the grid, and it took about 10 hours for stabilization, after which a typical detector background was 7.5×10^7 ions/sec. When a filament was fresh it worked with very high detecting efficiency, but after a few days of continuous use it became less responsive and a replacement was required. The oxygen flow was turned up until the pressure inside the can increased from its base value 3×10^{-8} torr to the optimal 3×10^{-7} torr. Further opening of the leak valve resulted in more

scattered background without any increase in the signal strength. Noise from the detector including its electronics was carefully studied and found to be negligible compared with the statistical fluctuations of a beam.

2.4 Beam Stop and Collimators

2.4.1 Moveable Beam Stop

In observing the resonance signals we relied on the state-dependent deflection of TlF molecules by the electrostatic quadrupoles. The uninteresting straight-through beam, which would have constituted a huge background, was blocked by a ball placed on the beam axis. A 2.4-mm diameter stainless steel ball was spot-welded onto two thin and springy wires intersecting at 90 degrees and each wire was connected to a micrometer that allowed us to put the ball at the right position while monitoring the beam. This unit was placed just inside the quadrupole at the detector end, 1.5 cm past the entrance plane. Electrically it was grounded so that when the quadrupole was symmetrically charged, the ball and wires did not disturb the field.

While the solid angle subtended by the beam stop completely shadowed the effective area of the detector, some molecules from the source still went around it by scattering. We defined the scattered beam, SC, as the number of TlF's detected per unit time with the beam stop in position. Collisions of TlF with background gas were mainly responsible for the scattered beam. Consequently, SC depended on the pressure inside the machine and at a normal operating condition it was about 3.5% of the full beam (Eq. 2.11), i.e. at the FB of 1.25×10^{10} molecules/sec, SC was 4.4×10^{8} molecules/sec. In addition to this, SC seemed to be contributed by the rebounding TlF molecules off the various field plates along the beam machine - e.g. the electric field plates in the NMR region. This was substantiated by the observation that even when the pressure was extrapolated to zero there

remained a finite SC of 1 or 1.5% of the FB. The scattered background could have been reduced with a larger beam stop, but only at the expense of the resonance strength and we settled at the present size after a few trials.

2.4.2 Collimators

Collimators defined admissible molecular trajectories and thereby reduced the scattered background. At the detector end, a TlF molecule could reach the hot surface of a filament only through the 2.5-mm diameter hole in the collecting plate. It helped to keep the SC low. In the source can there was a 9.5-mm diameter collimating hole at 8.8-cm downstream from the nozzle which kept the rest of the machine from being coated with TlF sprayed out of the source. This was important in order to ensure the electric stabilities of the high-voltage field plates and the proper operation of the butterfly valve at the downstream end of the source can. There were also two baffles with 1.2-cm diameter holes separating the source and detector chambers from the main region of the beam machine (§§ 2.1.2), which served as collimators as well as the constrictions for the differential pumping.

In an effort to reduce the scattered background without compromising the signal strength, two irises were tried. One was placed at the neck of the detector can, 5 cm downstream the exit of the quadrupole and another right in front of the collecting plate of the detector. It was possible to open and close them from the outside so that the openings were optimized for maximum ratio of signal to background. They turned out to be, however, only marginally useful and already having many parameters to adjust we did not push the idea very far.

2.5 Electrostatic Quadrupoles

Being a strongly polar molecule, TlF in a high electric field experiences a significant Stark shift and depending on its rotational state the shift can be either positive or negative. Consequently, molecules in different rotational states follow different trajectories in a

region of electric field gradient. This state-dependent motion was used as a part of state-selection and polarization-detection mechanisms in the experiment: only those molecules in the "right" states were kept in the mainstream while others were pushed away. In the beam machine these regions of electric field gradient were realized by two identical electrostatic quadrupoles A and B, near the source and detector ends respectively. Another important function of the quadrupoles was to increase the number of molecules participating in the EDM measurement. For those molecules in the right state the quadrupoles worked as a pair of focussing lenses, increasing the accepting solid angle by a factor of more than 100. Many molecules that would never have reached the detector could do so with the help of the lenses.

2.5.1 Stark Effect of a Diatomic Polar Molecule

Stark interaction of a diatomic polar molecule is given by $-\vec{\mu}_E \cdot \vec{E}$, where the electric dipole moment $\vec{\mu}_E$ is along the internuclear axis. The strength of the moment is independent of rotation, vibration, or nuclear spin states to a good approximation - for TlF in its ground vibrational state μ_E/h=2128.5 kHz/(v/cm), see Table 2.2 -, and the interaction is determined from the orientation of the molecule inside an electric field. For this reason the molecule can be modeled as a rigid rotator with a constant electric dipole moment along its axis of symmetry and then the Hamiltonian is,

$$H_{Stark} = hB\vec{J}^2 - \vec{\mu}_E \cdot \vec{E} \tag{2.19}$$

where $\vec{J}$ is the rotational angular momentum, and the corresponding eigenvalue equation is

$$H_{Stark}\psi = W\psi. \tag{2.20}$$

Because the rotational symmetry is broken by the introduction of the external electric field $\vec{E}$, J is not a good quantum number any more and the matrix to be diagonalized can involve states with different rotational angular momenta. It can be solved either by a direct

diagonalization or by approximate analytic methods [KUS59] and the result for the J=1 manifold is plotted in Figure 2.5 using the dimensionless parameters $\lambda = \mu_E E/hB$ and $\varepsilon = W/hB$.

2.5.2 Focussing by the Electric Field Gradient

When the electric field is small ($\mu_E E \ll hB$), the Stark shift for the $|J = 1, M_J = 0\rangle$ state can be approximated by a quadratic function,

$$W(J = 1, M_J = 0) \cong hB\left[2 + \frac{1}{10}\left(\frac{\mu_E E}{hB}\right)^2\right]. \tag{2.21}$$

In the field gradient region of the quadrupoles, where the strength of the E field grows approximately linearly with the radius, the energy of Eq. (2.21) corresponds to a radial potential well for a simple harmonic oscillator. There are two such quadrupoles in our beam machine, and the field strength there can be chosen so that a molecule will complete a quarter of a period of a radial harmonic motion as it passes through each of them. In this way a molecule diverging from a source can be focussed onto a detector if it stays on the same focussable state during its travel through the machine. In practice, however, this low-field focussing is not the most efficient, and the optimal field is strong enough for the higher order terms of the Stark shift to become important. Nevertheless the basic idea remains the same.

From the Stark shift diagram of Figure 2.5 we note that $|M_J| = 1$ states seek the high field. Since the field grows radially in the quadrupoles, those molecules are defocussed. Even in the $M_J = 0$ state the Stark shift changes its directions when λ is larger than 4.9 and the focusing does not work any more. This sets the largest operating electric field E_{max} and the maximum radial speed v_{max} of a molecule that can be focused. From the parameters of a TlF molecule in Table 2.2 and its mass,

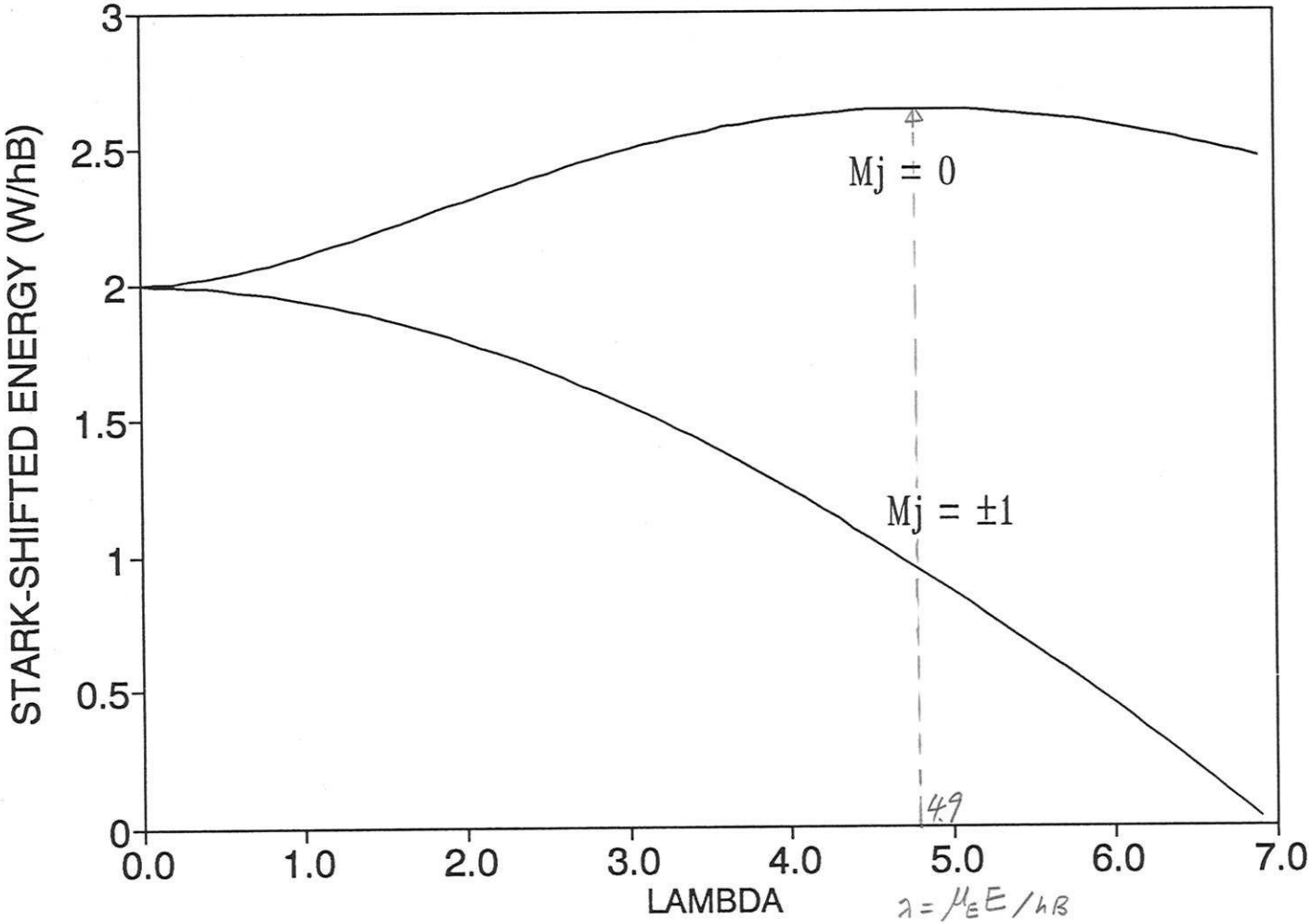

Fig.2.5 Stark shift of J=1 manifold

$\lambda = \mu_E E / hB$

$\mu_E/h = 2128.514$ kHz/(V/cm)

$B = 6.68987$ GHz

$\lambda = 4.9 \Rightarrow E = 15.4$ (kV/cm)

$$m = 3.71 \times 10^{-22}\text{gram} \tag{2.22.a}$$

the limiting values are

$$E_{max} = 14.4\text{kV/cm} \tag{2.22.b}$$

$$v_{max} = 3.9 \times 10^{2}\text{cm/sec}, \tag{2.22.c}$$

where the Stark shift of $0.64hB$ at λ=4.9 was used. Similar focussing effects are expected for the higher rotational states as well, but progressively stronger electric field would be required to overcome the increased centrifugal forces.

2.5.3 Design of the Quadrupoles

For the 2 dimensional configuration of charges in Figure 2.6.a, the electrostatic potential can be expanded near the origin as

$$V(x,y) = \frac{3q}{4\pi\varepsilon_o}\frac{x^2 - y^2}{a^3}. \tag{2.23}$$

The electric field is given by its gradient

$$\vec{E}(x,y) = \frac{6q}{4\pi\varepsilon_o}\frac{-x\hat{x} + y\hat{y}}{a^3}. \tag{2.24}$$

The direction of the field changes from one point to another, but the magnitude is proportional to the radial distance $r = \sqrt{x^2 + y^2}$ in so far as Eq. (2.24) remains valid and it is given by

$$E(r) = \frac{6q}{4\pi\varepsilon_o}\frac{r}{a^3}. \tag{2.25}$$

In the real electrostatic quadrupoles the hyperbolic equipotential surfaces are approximated by four parallel cylindrical rods which are alternately charged to $+U_o$ and $-U_o$ (Figure 2.6.b). The E field strength in the central zone is expressed by

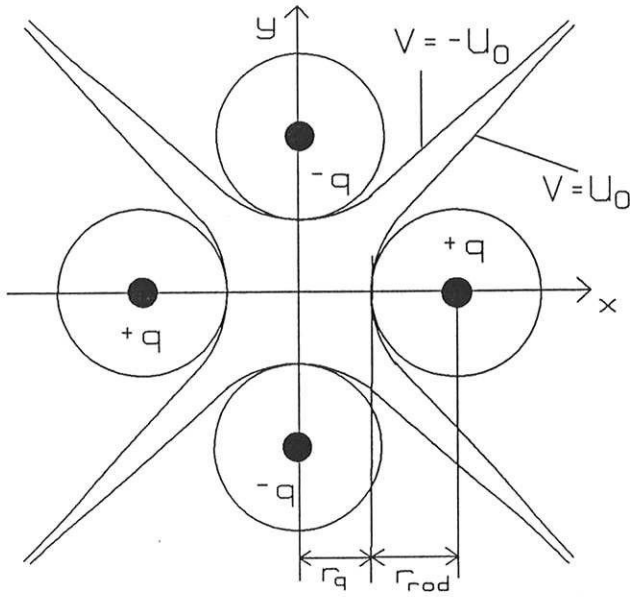

Fig 2.6.a Quadrupole charge distribution

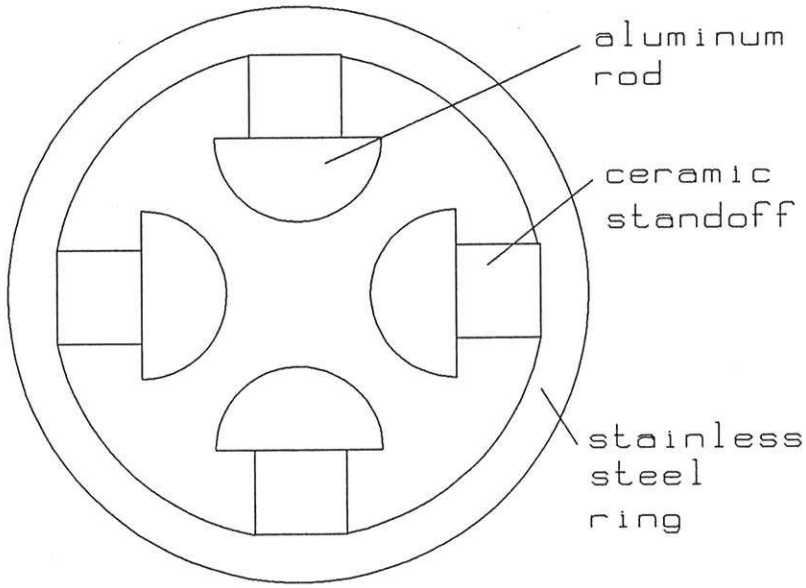

Fig 2.6.b Quadrupole construction

$$E(r) = \frac{2U_o}{R_q}\frac{r}{R_q}. \tag{2.26}$$

The four-rod geometry is known to be closest to the hyperbolic one when the ratio R_{rod}/R_q is 1.16 [DAY54].

The original pairs of the quadrupoles that were used with an effusive source were found to be inadequate for the jet source because of the increased beam velocity. For a few typical velocity distributions of the jet beam (Eq. 2.10), focussing efficiencies of the quadrupole lenses with different dimensions and operating voltages were estimated by calculating the trajectories of TlF molecules in the focussable state through the machine. Here the focussing efficiency κ is defined by

$$\kappa = \frac{\int_{\Delta\Omega} d^3\vec{v}\,\eta(\vec{v})f(\vec{v})}{FB}, \tag{2.27}$$

where $\Delta\Omega$ is the accepting solid angle of the A quadrupole, $\eta(\vec{v})$ is 1 if the molecule with $\vec{v}$ is focussed onto the detector, and 0 otherwise, and FB is the full beam (Eq. 2.11). The path of a TlF molecule inside the quadrupoles was computed by a second order Runge-Kutta method. As a consequence of this calculation we built new quadrupoles in which the length was doubled to 60 cm and the radii were slightly increased to R_{rod}=1.75 cm and R_q=1.16cm. (We note that the ratio R_{rod}/R_q for our design was 1.51. This deviation from an ideal prescription, however, did not affect the performance of the quadrupoles in practice.) Though detailed computations were involved, these design parameters can be rationalized by simple arguments. First, the increase in the radial dimensions is desirable for larger acceptance of a beam, but it requires higher voltages on the rods to build strong enough field inside of them. Since we were equipped with supplies to provide ±15 kV, we set R_q=1.16 cm so that the maximum attainable field would be 22.3 kV/cm which is roughly 50% larger than E_{max}. Secondly, using the low field approximation (Eq. 2.21) and the field of Eq. (2.25), the frequency of radial oscillation is

$$\omega = \frac{2U_o\mu_E}{R_q^2}\sqrt{\frac{1}{5mhB}}. \qquad (2.28)$$

For a typical voltage of U_o=12 kV, one quarter of a period is 1.7 msec which translates into about 60 cm for a molecule flying with the typical velocity of 3.4×10^4 cm/sec.

Vcm page 36

2.5.4 Quadrupoles Construction and High Voltage Systems

Each rod of the quadrupole had a cross section of a semi-circle, and was made of aluminum, mainly for ease of machining. They were annealed to prevent distortions and finally the surfaces were polished to hold high electric fields. They were assembled by mounting the four rods on two stainless steel rings through ceramic standoffs, and the electrical connections were made by wiring pairs of facing rods together (Figure 2.7). We could then plug the unit into the chamber which had grooves to locate the rings, and the quadrupole centered itself. Two feedthroughs on each chamber made spring contacts with top and one of the horizontal rods and allowed us to supply high voltages to the quadrupoles.

Two separate units of programmable high voltage supplies of positive and negative 15 kV (Bertan 602B-150P/N) were used to provide required potentials on the quadrupoles. The outputs from the supplies went through a pair of DPST relays (Kilovac K61C341) before connected to the feedthroughs so that we could reverse the polarities on the quadrupoles. This reversal of the quadrupole field, which was accompanied by those of the electric fields in the state selectors and the NMR regions, was an essential part of the experimental method we used to measure the CP-violating EDM (§§ 3.1.2). The relays rated to 35 kV were immersed in transformer oil, which had higher dielectric strength than air, and they worked without a breakdown up to ±15kV. In a normal configuration, output from the positive supply was connected to the NC (normally closed) terminals of the two relays and the negative one to the NO (normally open) terminals while the relays were

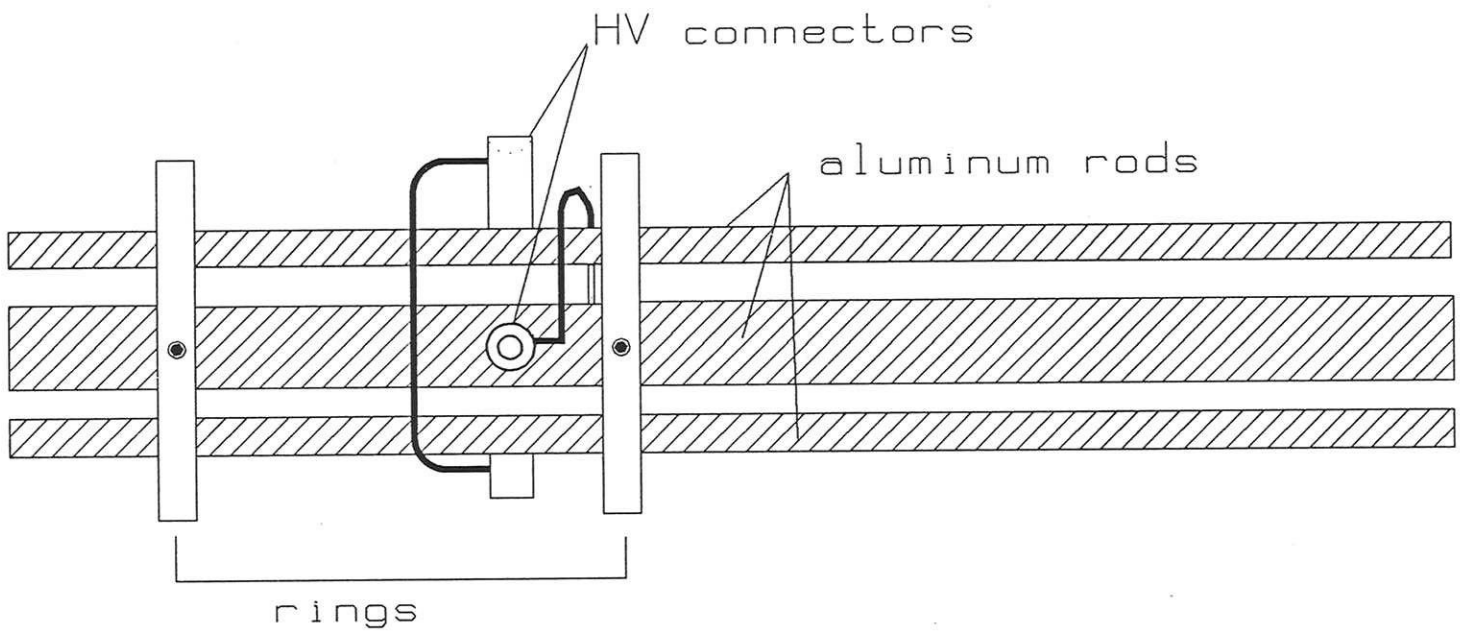

Fig 2.7 Side view of quadrupole

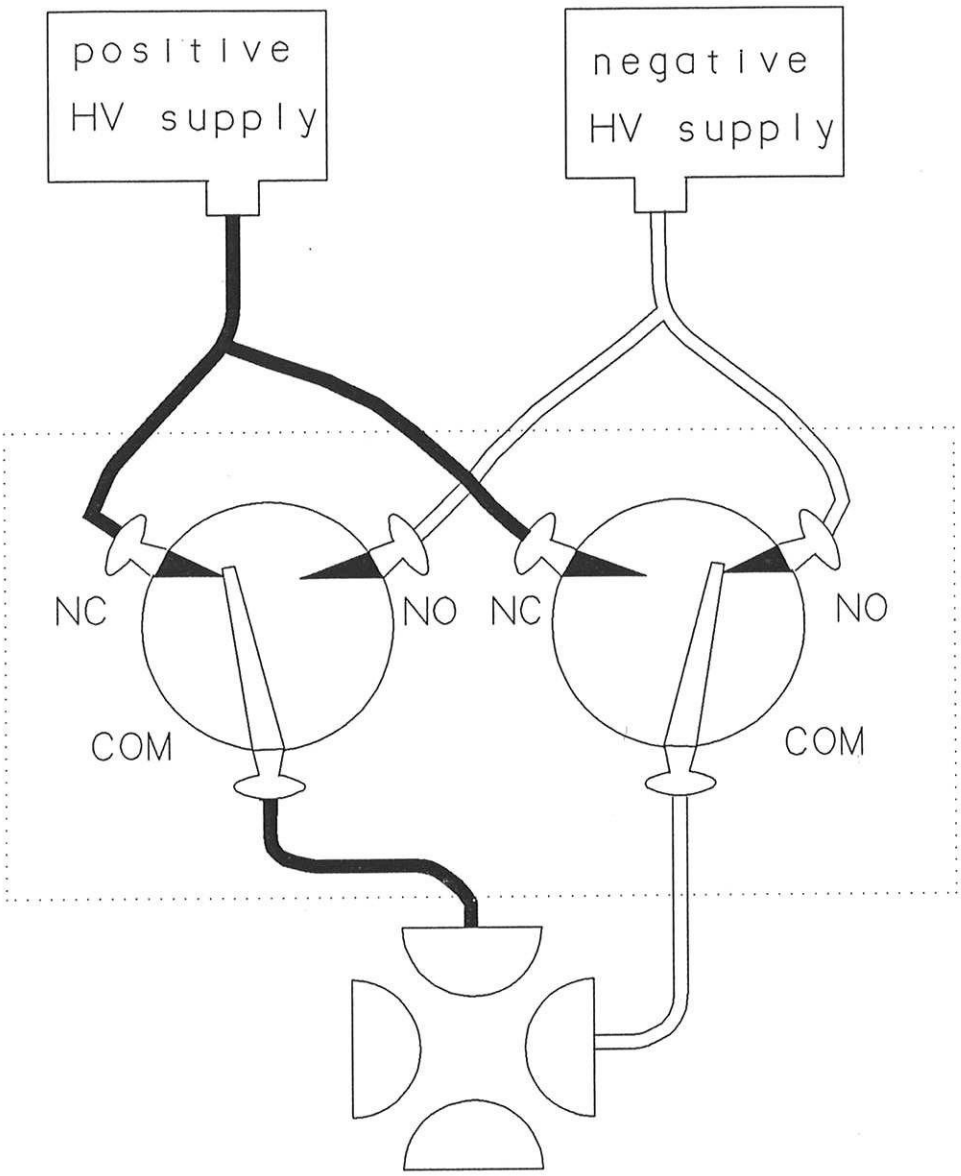

Fig 2.8 Quadrupole HV connections

operating in a complementary manner so that the two COMMON's were the effective outputs (Figure 2.8). This was a better way of wiring than having the COMMON's as the inputs in which case the positive and negative supplies could be shorted in case of a relay failure. To reverse the polarity, first the high voltages were turned off and after they dropped down to one or two kV the relays were flipped and the voltages were turned back on.

2.5.5 Operation and Performance of the Quadrupoles.

In daily operation of the machine, we first minimize the scattered beam by placing the beam stop at the center, and then the quadrupoles are turned on. The consequent increase in the detected beam intensity is called the focussed beam, or FOC. According to the definition of focussing efficiency κ of Eq. (2.27), FOC would have been simply related to FB by FOC=κFB if all the molecules coming out of the source were monomeric TlF in the $|J=1, M_J=0\rangle$ state. Since this is not the case,

FB is unrelated to FOC !!!

$$FOC(J=1) = \kappa \cdot \frac{1}{3} P_{J=1} \cdot r_m \cdot FB, \qquad (2.29)$$

where the factor of 1/3 is included to take into account that only one out of the three magnetic sublevels of J=1 is focussed. For typical operation of the source the J=1 fraction, $P_{J=1} = 2.7 \times 10^{-3}$ which corresponds to the rotational temperature of 350°K and the monomer fraction, $r_m \cong 0.92$. FOC(J=1) was measured at a few different quadrupole high voltages (U_o). The calculation of FOC(J=1) vs. U_o was remarkably close to the measurements (Figure 2.9) when the calculation was done for the velocity distribution $f(\vec{v})$ with the parameters in Eq. (2.13) which corresponded to the translational temperature of 300°K. The measurement was made at the oven temperature of 753°K and FB=1.25×10^{10} molecules/sec. The maximum FOC(J=1) observed at U_o=14 kV was 1.01×10^9 molecules/sec which could implied κ=97. The calculations put it at 120 ±15, and this excellent agreement supports our estimate of the rotational temperature. We note that there was an increasing

$1.01 \times 10^9 = k \cdot \frac{1}{3} \cdot 2.7 \times 10^{-3} \times 0.92 \times 1.25 \times 10^{10}$

$\rightarrow k = 97$

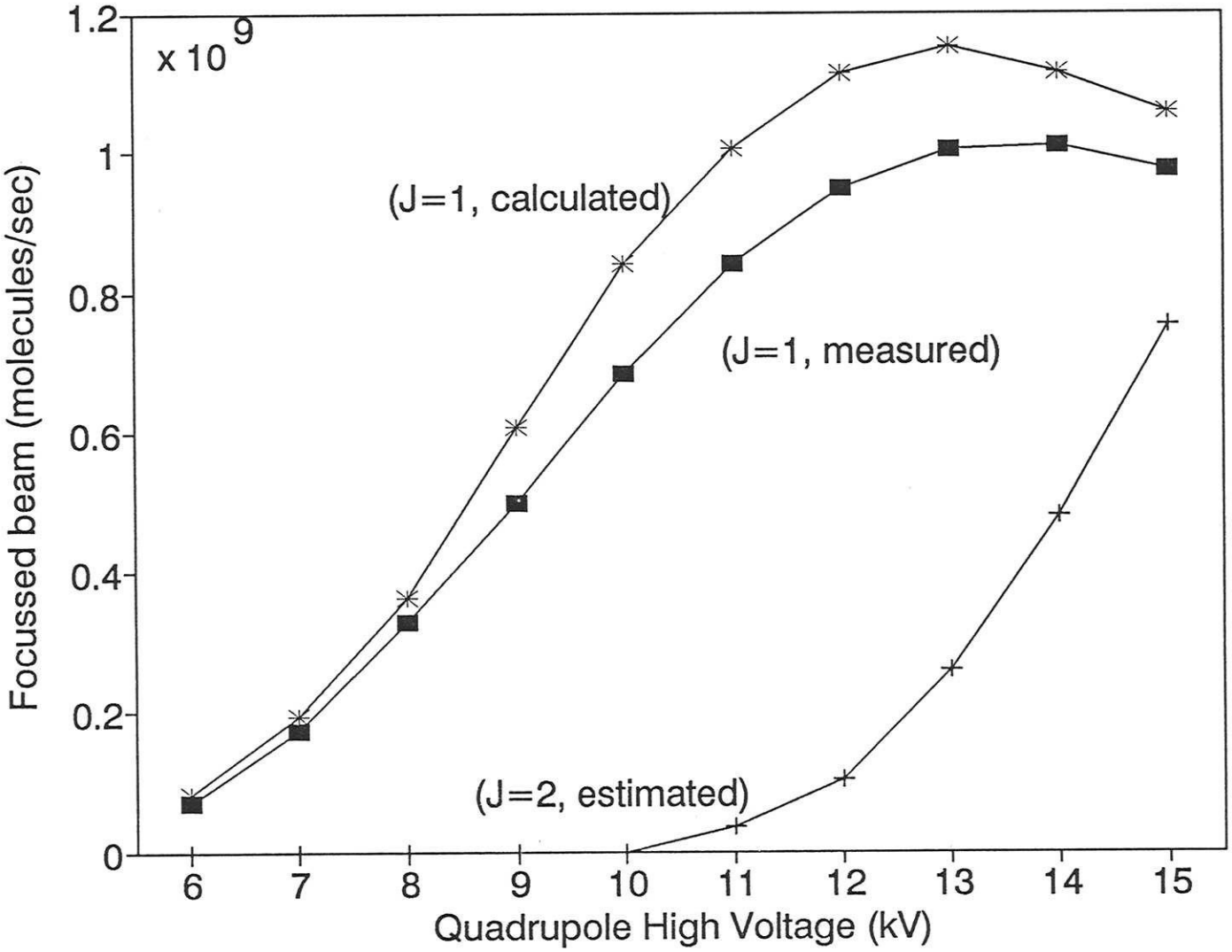

Fig. 2.9 Focussed beam for J=1 and J=2 states

contribution from the J=2 states to the total focussed beam as U_o went up. The distinction between FOC(J=1) and FOC(J=2) was made by observing the strength of a state selector resonance specific to one of the J=1 hyperfine levels and the unexplained part of the focussing was taken to be from the J=2 states. When we tried to measure the CP-violating EDM of the molecule, this J=2 component gave a troublesome background. Consequently, most of the data was taken at U_o=9 kV, where the focussing efficiency for J=1 was only 45% of its peak value at 14 kV, FOC=4.43×10^8 molecules/sec, but virtually all of them were in the J=1 state.

By scanning the quadrupole voltage we can vary the average beam velocity as well as the focussing efficiency - a fact already used to determine the translational temperature from the FOC vs. U_o curve. Numerically, the average axial beam velocity, $\langle v_z \rangle$ of the focussed molecules is given by the expression,

$$\langle v_z \rangle = \frac{\int_{\Delta\Omega} d^3\vec{v}\, v_z \eta(\vec{v}) f(\vec{v})}{\int_{\Delta\Omega} d^3\vec{v} \eta(\vec{v}) f(\vec{v})}. \qquad (2.30)$$

Results of the calculations at $T_{translation}$=300°K and the measurements are plotted in Figure 2.10. The indirect measurements of $\langle v_z \rangle$ were made from the linewidth of the nuclear magnetic resonance which was proportional to the beam velocity (§§ 2.7.5). The excellent agreement provided an independent evidence that our estimate of the translational temperature was correct. We note that the change in $\langle v_z \rangle$ over the range of U_o in the plot is quite significant; e.g. $\langle v_z \rangle$ at 9 kV is only 74 % of that at 14 kV and the corresponding reduction in the linewidth makes the operating voltage of 9 kV not so much a loss in the final sensitivity of the experiment as it first appeared.

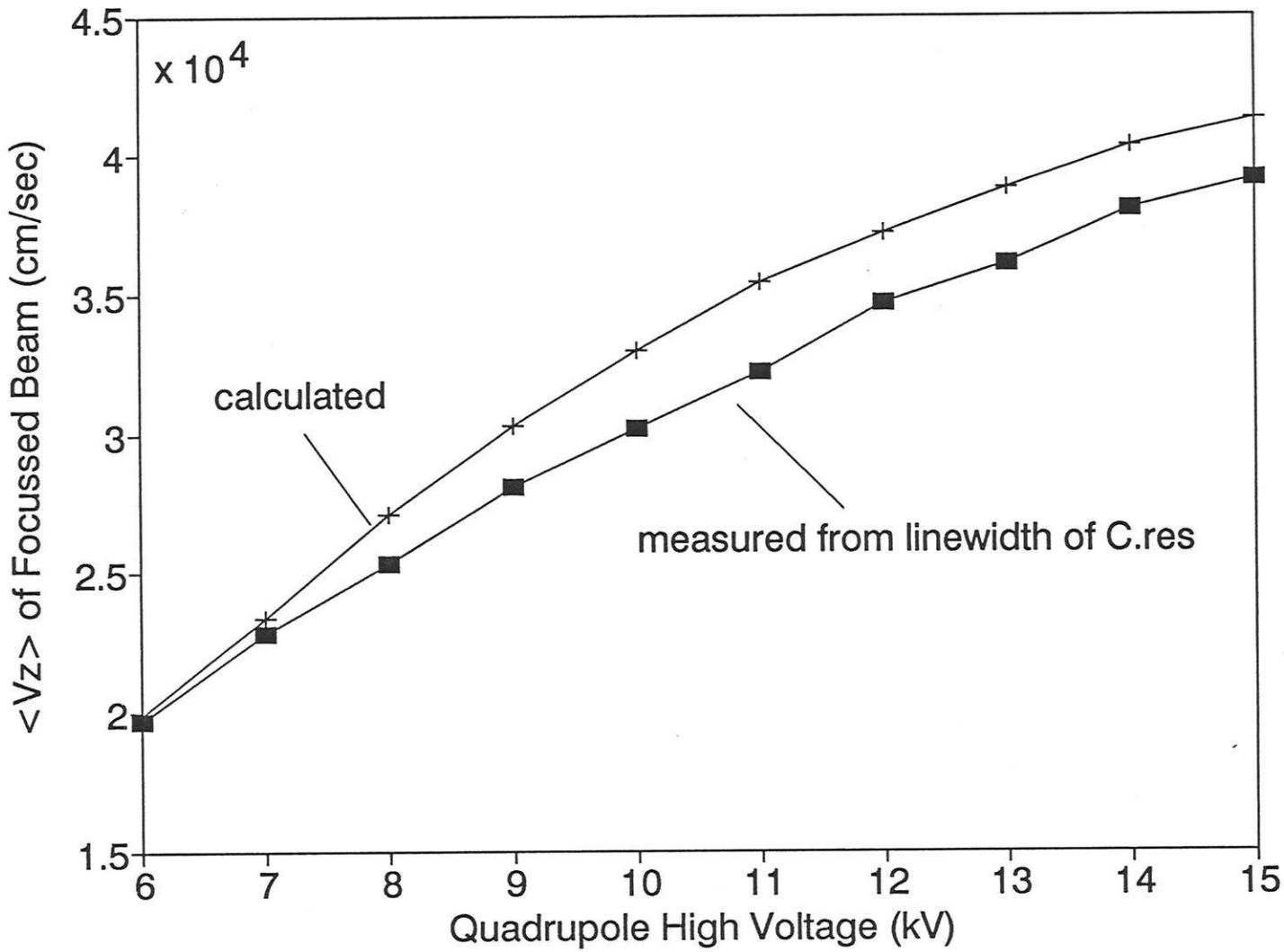

Fig. 2.10 <Vz> vs. quadrupole HV.

2.6 State Selectors

In addition to focussing the beam, the quadrupoles do part of the required state selection by focussing only those molecules in the state $|J=1, M_J=0\rangle$, but they are insensitive to the spin states of thallium and fluorine nuclei - both of them have spin 1/2. The focussing is equally effective on each of the four combinations of nuclear spin states. Polarization and analysis of the nuclear spins is accomplished by a pair of "state selectors", A on the source side and B on the detector side. To understand how the state selectors are working we need to know more about the inner details of a thallium fluoride molecule.

2.6.1 Hyperfine Structure of free TlF

For a complete quantum mechanical description of a thallium fluoride molecule one has to consider its electronic, vibrational, rotational, and hyperfine structures. In this experiment, however, everything interesting happens in the ground vibrational and J=1 rotational state, leaving only the twelve hyperfine sublevels of the state to consider. They are subject to various electric and magnetic fields in the apparatus, but the largest shift in energy they experience in the interactions is only of the order of the rotational energy hB which is much smaller than the separation of vibrational levels and even smaller than that of the electronic levels. Consequently, the proper basis set for the interactions can be provided by the eigenstates of the Hamiltonian,

$$H_{HF} = H_{ROT} + H_{S\text{-}R} + H_{S\text{-}S}^{DIRECT} + H_{S\text{-}S}^{INDIRECT}, \tag{2.31}$$

where

$$H_{ROT} = hB\vec{J}^2,$$

$$H_{S\text{-}R} = C_1(\vec{I}_{Tl} \cdot \vec{J}) + C_2(\vec{I}_F \cdot \vec{J}),$$

$$H_{S\text{-}S}^{DIRECT} = 10C_3\left\{\frac{3(\vec{I}_{Tl} \cdot \vec{J})(\vec{I}_F \cdot \vec{J}) - (\vec{I}_{Tl} \cdot \vec{I}_F)\vec{J}^2}{(2J+3)(2J-1)}\right\},$$

and

$$H_{S\text{-}S}^{INDIRECT} = C_4(\vec{I}_{Tl} \cdot \vec{I}_F).$$

Here $\vec{I}_{Tl}$ and $\vec{I}_F$ are the Tl and F nuclear spins, $\vec{J}$ is the rotational angular momentum and C_1 through C_4 are the coupling constants of the hyperfine interaction. The values of the various constants involved are shown in Table 2.2 for vibrational states n=0 to n=2, together with other spectroscopic parameters [DIJ72, HER79]. H_{ROT} is the kinetic energy of the rotational motion, and $H_{S\text{-}R}$ is the interaction energy of the nuclear magnetic dipole moments with the magnetic field generated by the rotation of the polar molecule as a whole, which is called a spin-rotation coupling. There are two different ways that the nuclear spins of Tl and F can interact with each other; $H_{S\text{-}S}^{DIRECT}$ is the usual dipole-dipole interaction,

$$H_{\text{dipole-dipole}} = \frac{\mu_0}{4\pi}\frac{1}{r^3}\left[\vec{\mu}_{Tl}\cdot\vec{\mu}_F - \frac{3(\vec{\mu}_{Tl}\cdot\vec{r})(\vec{\mu}_F\cdot\vec{r})}{r^2}\right] \tag{2.32}$$

evaluated for a given angular momentum J using the vector nature of $\vec{r}$, and $H_{S\text{-}S}^{INDIRECT}$ is the same interaction mediated by the electrons [RAM56].

The Hamiltonian H_{HF} commutes with the total angular momentum vector $\vec{F} = \vec{J} + \vec{I}_{Tl} + \vec{I}_F$, as well as with $\vec{J}^2$, $\vec{I}_{Tl}^2$, and $\vec{I}_F^2$. Consequently, its eigenstates have the quantum numbers (F, M_F) and $(J, I_{Tl} = 1/2, I_F = 1/2)$ with M_F being a magnetic quantum number of $\vec{F}$. When J=1, the 12 states group into F=2, F=1, F=1, and F=0 - there are two different ways to have the total angular momentum F of 1 - and the four corresponding energy eigenvalues give rise to the unperturbed hyperfine structure with a typical scale of 10^5 Hz measured in frequency. Those twelve eigenstates have been conventionally labelled by A through L. Their expansions in terms of $|M_J, M_1, M_2\rangle$, where M's are the magnetic quantum numbers and 1 and 2 refer to Tl and F nuclei respectively, are given in Table 2.3.a. The unperturbed structure is shown in the level diagram of Figure 2.11, where it is apparent that the levels with F=2 and F=1 are grouped separately from those with F=1′ and F=0.

		n=0	n=1	n=2
C_1/h	(kHz)	126.03(12)	124.99(7)	123.89(39)
C_2/h	(kHz)	17.89(15)	17.87(7)	17.39(39)
C_3/h	(kHz)	0.70(3)	0.70(2)	0.72(2)
C_4/h	(kHz)	-13.30(72)	-13.0(10)	-13.1(10)
μ_E/h	(kHz/(V/cm))	2128.5(4)	2163.2(5)	2198.1(5)

ν_o	1431	GHz	
B	6.68987	GHz	
μ_J	0.035(15)	kHz/gauss	
μ_{Tl}^{205}	1.2487	kHz/gauss	
μ_{Tl}^{203}	1.2366	kHz/gauss	
μ_F	2.0039	kHz/gauss	

Table 2.2 Spectroscopic parameters of TlF

Such a substructure within the J=1 manifold is one consequence of the strong spin-rotation coupling between $\vec{J}$ and $\vec{I}_{Tl}$. Among various possible ways to combine the three angular momenta, $(\vec{J}+\vec{I}_{Tl})+\vec{I}_F$ is the most reasonable coupling scheme here.

2.6.2 Zeeman and Stark Interactions of TlF

The Zeeman and Stark interactions of thallium fluoride are described by the Hamiltonians,

$$H_{ZEE} = -\frac{\mu_J}{J}(\vec{J}\cdot\vec{B}) - \frac{\mu_{Tl}}{I_{Tl}}(\vec{I}_{Tl}\cdot\vec{B}) - \frac{\mu_F}{I_F}(\vec{I}_F\cdot\vec{B}), \tag{2.33}$$

and

$$H_{STA} = -\vec{\mu}_E\cdot\vec{E}, \tag{2.34}$$

where the various dipole moments are already given in Table 2.2.

Inside a state selector we have both magnetic and electric fields with strengths of 27 gauss (B_{SS}) and 35 V/cm (E_{SS}), respectively. These fields give the shifts comparable with the unperturbed hyperfine structure itself and there emerges no definite coupling scheme. We therefore used a computer to diagonalize the total Hamiltonian,

$$H = H_{HF} + H_{ZEE} + H_{STA} \tag{2.35}$$

using a basis that includes rotational states of J up to 6. We note that by design, the applied magnetic and electric fields were parallel in the state selectors leaving M_F still a good quantum number. The Stark and Zeeman shifts of the twelve J=1 states for electric and magnetic fields near E_{SS} and B_{SS} are shown in Figure 2.12 and 2.13.

Although we have electric and magnetic fields of intermediate strengths in the state selector it is still instructive to consider the limits of high fields. In a strong magnetic field the three angular momenta decouple in the fashion of the Pashen-Back effect, and the limiting eigenstates are $|M_J, M_1, M_2\rangle$ as shown in Table 2.3.b. The case of strong electric field was already considered in the discussion of the quadrupoles, where the field strength was around 10 kV/cm and the states spilt into two groups of $M_J = 0$ and $M_J = \pm 1$ with a typical separation of hB or 10^9 Hz. This is 4 orders of magnitude larger than the hyperfine structure which, however, is still present within the groups of 4 ($M_J = 0$) and 8 ($M_J = \pm 1$). In Figure 2.16 the levels of $M_J = \pm 1$ at the electric field strength of 29.5 kV/cm are shown. The eigenstates in this limit have well defined $|M_J|$ and M_F but otherwise they can be combinations of different $|M_J, M_1, M_2\rangle$ states with various J's. The combinations for the states labelled by J=1 are given in the third column of Table 2.3.b. Finally we note that in the NMR region once again strong electric field is present without magnetic field and the states regroup according to their quantum numbers of $|M_J|$ - see Figure 2.16.

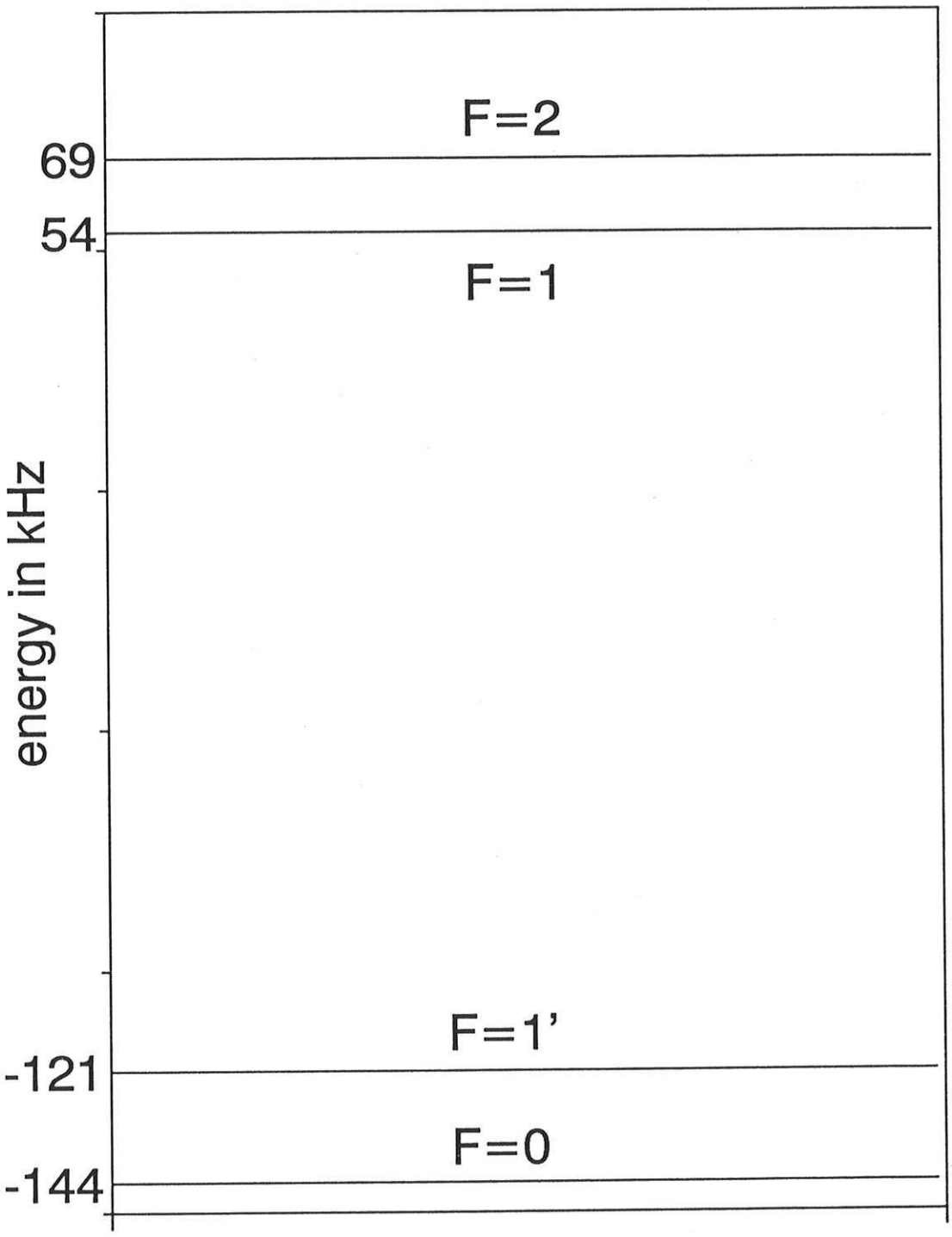

Fig. 2.11 Spectrum of free TlF

label	$\|F, M_F\rangle$	free hyperfine states
A	$\|2,-1\rangle$	$\frac{1}{\sqrt{2}}\left\|0,-\frac{1}{2},-\frac{1}{2}\right\rangle+\frac{1}{2}\left\|-1,+\frac{1}{2},-\frac{1}{2}\right\rangle+\frac{1}{2}\left\|-1,-\frac{1}{2},+\frac{1}{2}\right\rangle$
B	$\|2,0\rangle$	$\frac{1}{\sqrt{6}}\left\|+1,-\frac{1}{2},-\frac{1}{2}\right\rangle+\frac{1}{\sqrt{3}}\left\|0,+\frac{1}{2},-\frac{1}{2}\right\rangle+\frac{1}{\sqrt{3}}\left\|0,-\frac{1}{2},+\frac{1}{2}\right\rangle+\frac{1}{\sqrt{6}}\left\|-1,+\frac{1}{2},+\frac{1}{2}\right\rangle$
C	$\|1,0\rangle$	$-.36\left\|+1,-\frac{1}{2},-\frac{1}{2}\right\rangle-.61\left\|0,+\frac{1}{2},-\frac{1}{2}\right\rangle+.61\left\|0,-\frac{1}{2},+\frac{1}{2}\right\rangle+.36\left\|-1,+\frac{1}{2},+\frac{1}{2}\right\rangle$
D	$\|2,1\rangle$	$\frac{1}{2}\left\|+1,+\frac{1}{2},-\frac{1}{2}\right\rangle+\frac{1}{2}\left\|+1,-\frac{1}{2},+\frac{1}{2}\right\rangle+\frac{1}{\sqrt{2}}\left\|0,+\frac{1}{2},+\frac{1}{2}\right\rangle$
E	$\|2,-2\rangle$	$\left\|-1,-\frac{1}{2},-\frac{1}{2}\right\rangle$
F	$\|1,1\rangle$	$-.86\left\|+1,+\frac{1}{2},-\frac{1}{2}\right\rangle+.36\left\|+1,-\frac{1}{2},+\frac{1}{2}\right\rangle+.36\left\|0,+\frac{1}{2},+\frac{1}{2}\right\rangle$
G	$\|1,-1\rangle$	$.36\left\|0,-\frac{1}{2},-\frac{1}{2}\right\rangle+.36\left\|-1,+\frac{1}{2},-\frac{1}{2}\right\rangle-.86\left\|-1,-\frac{1}{2},+\frac{1}{2}\right\rangle$
H	$\|2,2\rangle$	$\left\|+1,+\frac{1}{2},+\frac{1}{2}\right\rangle$
I	$\|1',0\rangle$	$.61\left\|+1,-\frac{1}{2},-\frac{1}{2}\right\rangle-.36\left\|0,+\frac{1}{2},-\frac{1}{2}\right\rangle+.36\left\|0,-\frac{1}{2},+\frac{1}{2}\right\rangle-.61\left\|-1,+\frac{1}{2},+\frac{1}{2}\right\rangle$
J	$\|1',-1\rangle$	$.61\left\|0,-\frac{1}{2},-\frac{1}{2}\right\rangle-.79\left\|-1,+\frac{1}{2},-\frac{1}{2}\right\rangle-.08\left\|-1,-\frac{1}{2},+\frac{1}{2}\right\rangle$
K	$\|1',1\rangle$	$.08\left\|+1,+\frac{1}{2},-\frac{1}{2}\right\rangle+.79\left\|+1,-\frac{1}{2},+\frac{1}{2}\right\rangle-.61\left\|0,+\frac{1}{2},+\frac{1}{2}\right\rangle$
L	$\|0,0\rangle$	$\frac{1}{\sqrt{3}}\left\|+1,-\frac{1}{2},-\frac{1}{2}\right\rangle-\frac{1}{\sqrt{6}}\left\|0,+\frac{1}{2},-\frac{1}{2}\right\rangle-\frac{1}{\sqrt{6}}\left\|0,-\frac{1}{2},+\frac{1}{2}\right\rangle+\frac{1}{\sqrt{3}}\left\|-1,+\frac{1}{2},+\frac{1}{2}\right\rangle$

Table 2.3.a Eigenvectors of free TlF in J=1

label	high E field limit	high B field limit
A	$\left\|0,-\frac{1}{2},-\frac{1}{2}\right\rangle$	$\left\|0,-\frac{1}{2},-\frac{1}{2}\right\rangle$
B	$-\frac{1}{\sqrt{2}}\left\|0,+\frac{1}{2},-\frac{1}{2}\right\rangle+\frac{1}{\sqrt{2}}\left\|0,-\frac{1}{2},+\frac{1}{2}\right\rangle$	$\left\|+1,-\frac{1}{2},-\frac{1}{2}\right\rangle$
C	$-\frac{1}{\sqrt{2}}\left\|0,+\frac{1}{2},-\frac{1}{2}\right\rangle-\frac{1}{\sqrt{2}}\left\|0,-\frac{1}{2},+\frac{1}{2}\right\rangle$	$-\left\|0,+\frac{1}{2},-\frac{1}{2}\right\rangle$
D	$\left\|0,+\frac{1}{2},+\frac{1}{2}\right\rangle$	$-\left\|+1,+\frac{1}{2},-\frac{1}{2}\right\rangle$
E	$\left\|-1,-\frac{1}{2},-\frac{1}{2}\right\rangle$	$\left\|-1,-\frac{1}{2},-\frac{1}{2}\right\rangle$
F	$-\left\|+1,+\frac{1}{2},-\frac{1}{2}\right\rangle$	$-\left\|+1,-\frac{1}{2},+\frac{1}{2}\right\rangle$
G	$-\left\|-1,-\frac{1}{2},+\frac{1}{2}\right\rangle$	$\left\|-1,+\frac{1}{2},-\frac{1}{2}\right\rangle$
H	$\left\|+1,+\frac{1}{2},+\frac{1}{2}\right\rangle$	$\left\|+1,+\frac{1}{2},+\frac{1}{2}\right\rangle$
I	$-\frac{1}{\sqrt{2}}\left\|+1,-\frac{1}{2},-\frac{1}{2}\right\rangle-\frac{1}{\sqrt{2}}\left\|-1,+\frac{1}{2},+\frac{1}{2}\right\rangle$	$-\left\|0,-\frac{1}{2},+\frac{1}{2}\right\rangle$
J	$-\left\|-1,+\frac{1}{2},-\frac{1}{2}\right\rangle$	$-\left\|-1,-\frac{1}{2},+\frac{1}{2}\right\rangle$
K	$\left\|+1,-\frac{1}{2},+\frac{1}{2}\right\rangle$	$-\left\|0,+\frac{1}{2},+\frac{1}{2}\right\rangle$
L	$\frac{1}{\sqrt{2}}\left\|+1,-\frac{1}{2},-\frac{1}{2}\right\rangle-\frac{1}{\sqrt{2}}\left\|-1,+\frac{1}{2},+\frac{1}{2}\right\rangle$	$\left\|-1,+\frac{1}{2},+\frac{1}{2}\right\rangle$

Table 2.3.b Eigenvectors of TlF in J=1 at high E or B field

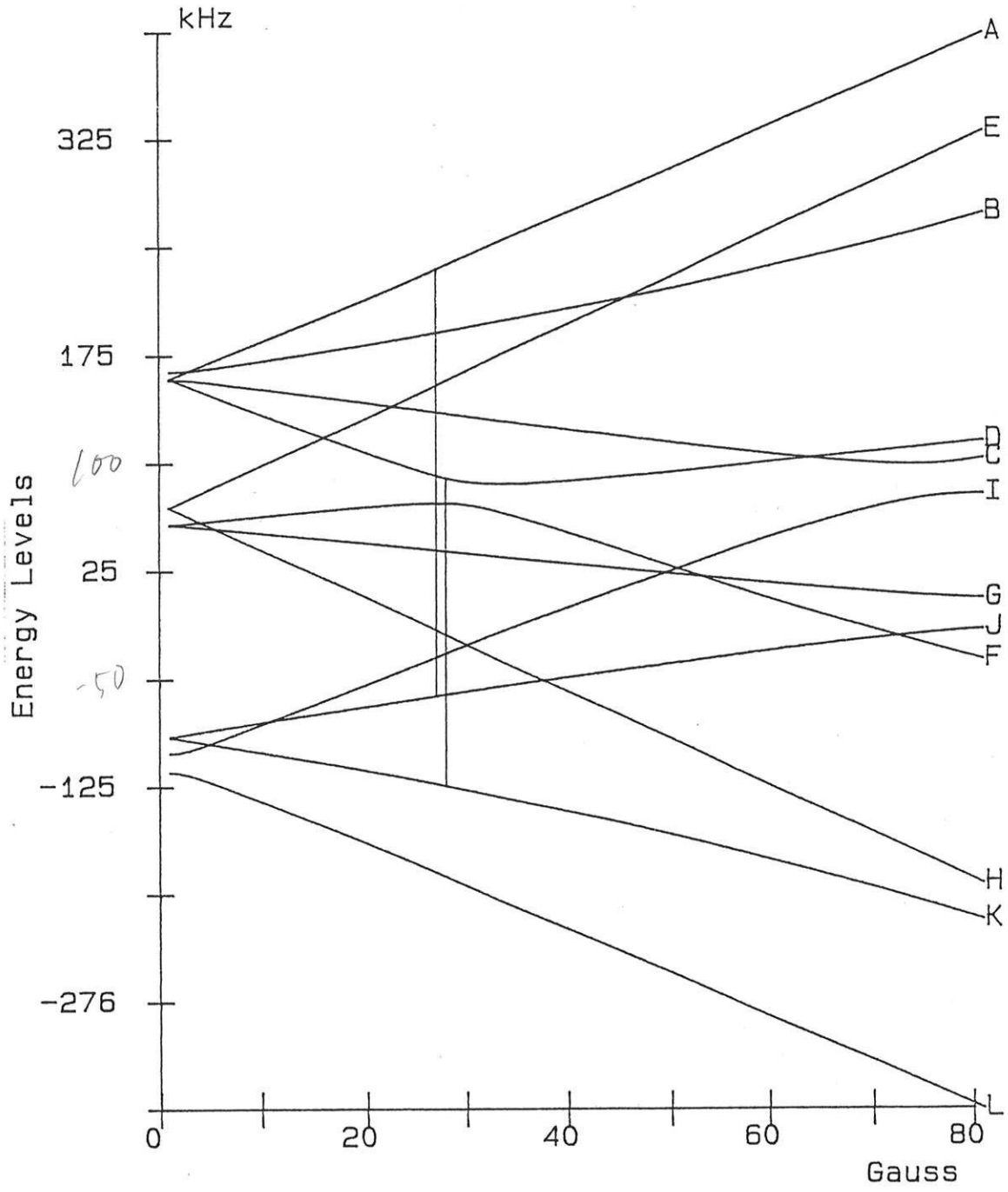

Fig. 2.12 Zeeman Shifts at E=35 V/cm

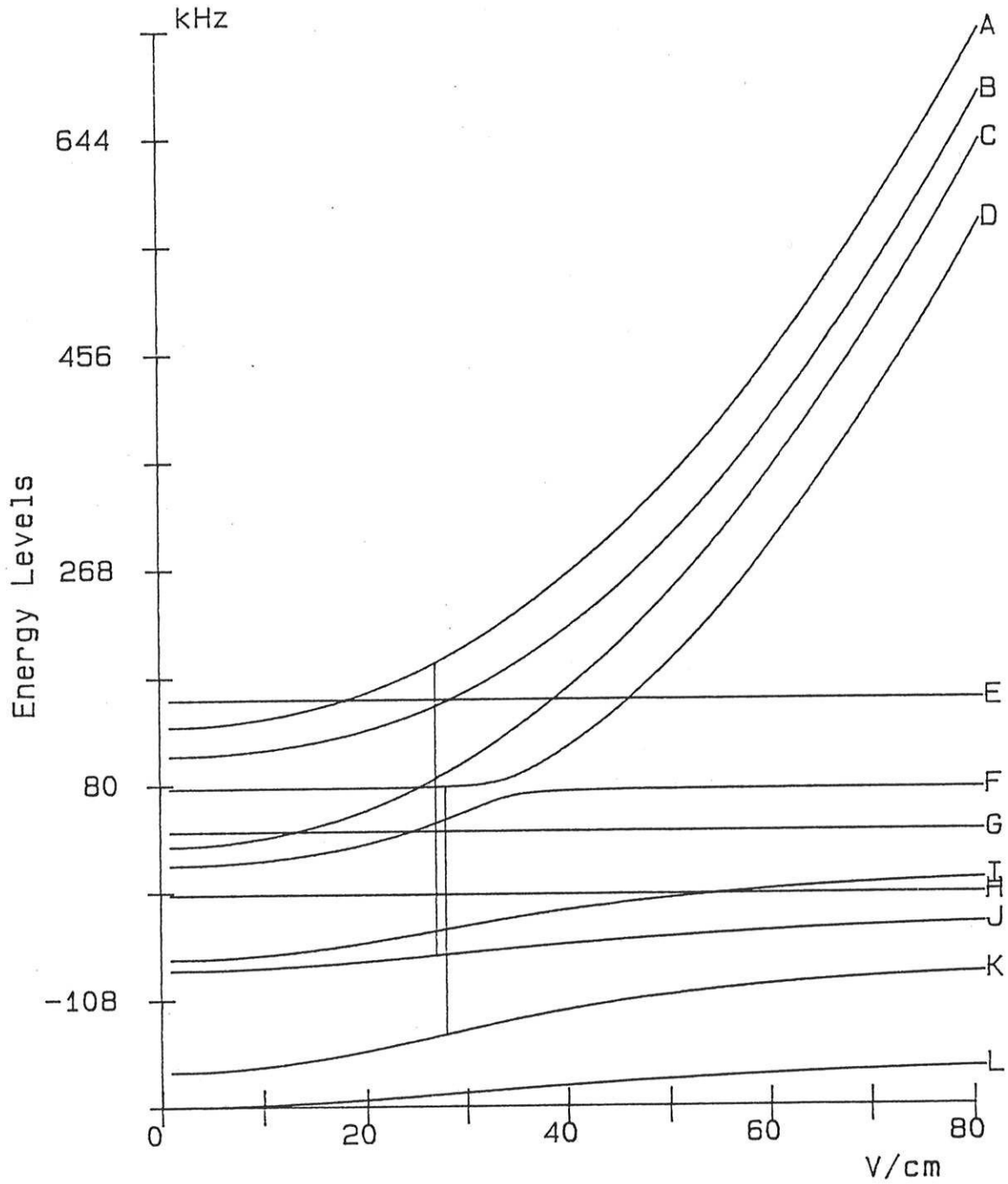

Fig. 2.13 Stark Shifts at B=27 Gauss

2.6.3 Intended and Unintended Transitions

In the NMR region there are a few possible M1 transitions of the thallium nuclear spin within the group $|M_J| = 1$. Among them the transitions between the pairs of levels (J,E) and (K,H) were studied in the experiment - the transitions are shown with dotted lines in Figure 2.16. The state selectors were tuned to the transitions that could populate either J or K from the focussed states A or D, respectively. We call the two sequences of transitions the AJE and DKH schemes, and both were employed in our EDM measurement.

One way to understand why the electrostatic quadrupoles are incomplete polarizers - or analyzers - in the measurement of T-violating effects is to note that the electric field vector is invariant under the time reversal transformation and the electric field gradient cannot distinguish a pair of states that are time reversed conjugates of each other. This situation can be improved by the introduction of magnetic fields which can resolve those states and lift the degeneracy associated with the T-invariance. In this sense the magnetic field is a logical necessity for a state selector, but having an electric field turns out to be as important. First of all, a state selector resonance is supposed to connect one hyperfine level of the focussed states to another in the unfocussed, and both belong to the manifold of the J=1, hence the same parity. With the help of the electric field we can get around the selection rule and drive an electric dipole (E1) transition that is much stronger than a magnetic dipole (M1) one. Secondly, it just gives us another degree of freedom in designing and operating the state selector and we have made very effective use of it in achieving a state selection with high purity as well as with good efficiency.

The state selectors were built in such a way that the oscillating electric field for an E1 transition was parallel to the applied electric and magnetic fields, allowing only $\Delta M_F = 0$ transitions (π). Because of this additional selection rule none of the focussed states, all of which have $|M_F| \leq 1$, can be driven down to E or H, both with $|M_F| = 2$. It was A to J and D to K transitions that were used: we will frequently refer these transitions as simply AJ and DK. For the chosen field strengths the AJ transition was resonant at 300 kHz and DK at 197 kHz. Besides the AJ and DK all other transitions that satisfy the selec-

tion rules could also be driven by adjusting either RF or static fields of the state selectors. They were useful in studying how each state evolved through the machine, and could have been used to select the states of F or G if we were interested in investigating the T-violating effects associated with the nuclear spin of fluorine.

The TlF experiment has some history of problems with state selection that limited the final sensitivity of the measurement severely, and it was the first triumph of the beam machine at Yale that controlled and highly efficient state selection was made possible. For this purpose the states of interest were guided carefully so that there was no Majorana transition (unintended transition made by a molecule which experiences time-dependent fields as a consequence of its motion) from one state to another.

One of the regions with a sudden change in the fields is between the quadrupole and the state selector where focussed molecules can make premature transitions that would compete with the intended AJ or DK resonance. Similarly, the passage from the state selector to the NMR region is accompanied by a large change in the fields. To make the transformations of the fields less dramatic, electrodes with intermediate field of a few hundred V/cm, which we called the buffer plates, were introduced in the state selector on both ends of the transition region (Figure 2.14). Once the state J (or K) is selected by the applied RF power, it is important to keep it from making any further transitions. It is especially vulnerable when the electric and magnetic fields of the apparatus are such that the state J happens to be degenerate with some other state, for example, I. Even a small perturbation can mix the degenerate pair transforming the selected state into the state I (Landau-Zener effect). Assuming that the energy eigenvalues, E(J) and E(I), change linearly in time near the degeneracy, the probability of J making an adiabatic transition to I is given by [RUB81]

$$P(J,I) = \exp\left(-2\pi \frac{|\langle \Psi_J | V | \Psi_I \rangle|^2}{\hbar (dE/dt)}\right), \tag{2.36}$$

where E is the difference between E(J) and E(I) given as a function of time, and V is the perturbation responsible for the coupling of the two states. Near the state selector the stray fields perpendicular to the quantization axis can give rise to such a coupling. To avoid this type of adiabatic transitions, the evolution of each state through the machine was mapped and all the crossings with potential problems were identified. Then a condition was sought to minimize the matrix element $\langle \Psi_J | V | \Psi_I \rangle$ for both E1 and M1 type interactions. Most of the study was done with a special attention to the state J which became degenerate with the state I when the magnetic field dropped to 9.6 gauss from its peak value at the transition region, quite independently of the electric field strength. Calculations showed that the matrix element was the smallest when the electric field was 90 V/cm, which was then applied across the buffer plates. In practice, field strengths higher than 90 V/cm up to 200 V/cm were found to be safe.

In addition to the effects from the changing fields, the RF field itself could drive unintended transitions, and every effort was made to separate the AJ and DK transitions away from nearby ones allowed by the selection rules. In the original design, an electric field of 30.5 V/cm and a magnetic field of 52 gauss were prescribed which put the AJ transition 25 kHz away from the nearest other line. For the runs we report here the fields were chosen to be E=35 V/cm and B=27 gauss, and the adjacent lines were the CL transition at 23 kHz and BI at 17 kHz away from AJ and DK, respectively. We opted for the new field values to achieve simultaneous isolation of both transitions and to work with a smaller magnetic field since we found the fringes of the B field from the state selector could leak into the NMR region and were a potential source of systematic effects.

2.6.4 Construction of the State Selectors

There were two identical state selectors in the apparatus and each of them was made of two parts; one to provide the static and oscillating electric fields, another for the static magnetic field. The electric part was a long box partitioned into 5 parallel pairs of plates separated by 2.4 cm (Figure 2.14). The center one of width 0.5 cm carried the RF field to

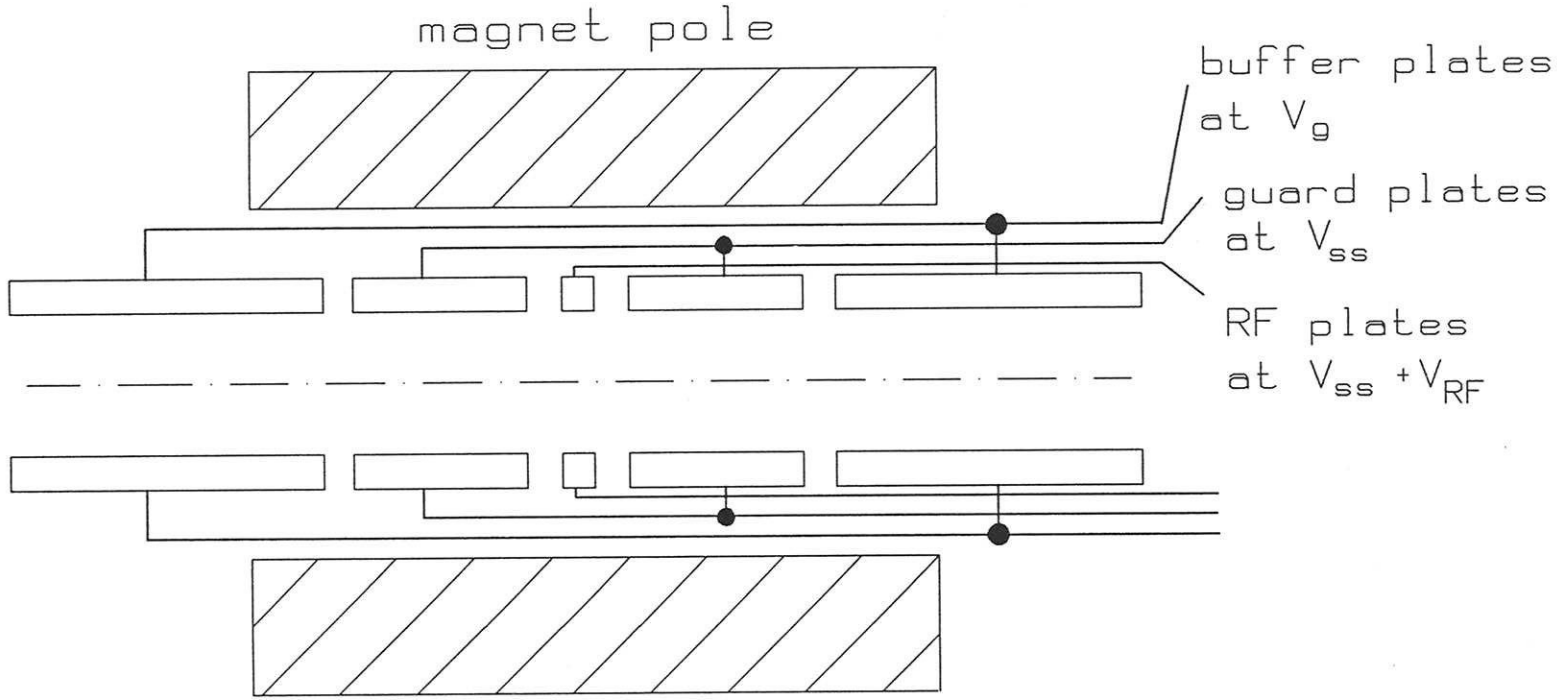

Fig 2.14 State selector

drive an E1 transition on top of a dc field that was shared with the two inner pairs, called the guard plates, to induce the Stark shift. The outermost pairs were the buffer plates. Narrow ground plates were added to the top and bottom of the box to provide the boundary conditions that could minimize the distortion of the electric field throughout the transition region. The magnet had a rectangular frame with somewhat larger cross section so that the box of the electric plates could slide in. The poles and the yokes were made of a high-permeability and low-hysterisis material (Ad-Mu 80) to shield the ambient field and to ensure an accurate reversal of the applied magnetic fields. The high permeability material was also machined to make a structure with high magnetic conductance to get a maximum uniformity of the field in the transition region. The field was generated by two of 165 turns of 16-gauge wires on each yoke, and it took 0.5 A to produce the required field of 27 gauss.

2.6.5 RF Power and Lineshape

Given the geometry of the state selectors we can calculate the optimal RF power for the AJ and DK transitions, and their lineshape. The application of the oscillating potential on the pair of RF plates (Figure 2.14), which are separated by 2a (2.4 cm) along the z axis, leads to the following boundary condition in the two dimensional idealization;

$$\text{at} \qquad z = \pm a \qquad V(x,z) = \pm V_0 h \delta(x), \tag{2.37}$$

where h (0.5 cm) is the width of the RF plates along the x axis, and the implicit time dependence of $\cos(\omega t)$ is assumed. For this boundary condition the solution of Laplace equation has an integral form, describing the electric potential between the field plates

$$V(x,z) = \frac{V_0 h}{2\pi} \int_{-\infty}^{+\infty} dk \, \frac{\sinh(kz)}{\sinh(ka)} \cos(kx). \tag{2.38}$$

At resonance ($\omega = \omega_0$) the optimal RF power for a molecule passing through the state selector with velocity v (2.8×10^4 cm/sec) is to be determined from the relation,

$$\frac{1}{2}|\langle\Psi_f|\vec{\mu}_E\cdot\hat{z}|\Psi_i\rangle|\int_{-\infty}^{+\infty}dt|E_z(t)|=\frac{\pi}{2} \tag{2.39}$$

with $$E_z(t)=-\frac{\partial}{\partial z}V(x,z)\Big|_{(x=vt,z=0)},$$

where the factor 1/2 comes from the rotating wave approximation. This can be integrated to give

$$\frac{1}{2}|\langle\Psi_f|\vec{\mu}_E\cdot\hat{z}|\Psi_i\rangle|\frac{V_0 h}{a\ v}=\frac{\pi}{2}. \tag{2.40}$$

The matrix elements for the AJ and DK transitions in static fields of E=35 V/cm and B=27 gauss were calculated numerically with the results,

$$D_{AJ}=|\langle\Psi_A|\vec{\mu}_E\cdot\hat{z}|\Psi_J\rangle| = 1.35\times10^4\ \text{sec}^{-1}/(\text{V/cm}) \tag{2.41.a}$$

$$D_{DK}=|\langle\Psi_D|\vec{\mu}_E\cdot\hat{z}|\Psi_K\rangle| = 1.62\times10^4\ \text{sec}^{-1}/(\text{V/cm}). \tag{2.41.b}$$

From these numbers we could predict that the AJ transition would be at its best efficiency when V_0 = 15.7 V and DK when V_0 =13.1 V. In our measurements the transitions were most efficient at

$$V_0(\text{AJ}) = 15V \tag{2.42.a}$$

$$V_0(\text{DK}) = 11V. \tag{2.42.b}$$

We consider the results as reasonable agreement considering the approximations made in the modeling of the boundary conditions and the calculation of the matrix element by first order perturbation.

In order to determine the lineshape of the state selector resonance we make a Fourier transformation of the oscillating electric field,

$$E_z(t)=-\frac{1}{2}\frac{\partial}{\partial z}V(x,z)\Big|_{(x=vt,z=0)}e^{-i\omega_0 t} \tag{2.43}$$

to get

$$G(\omega)=\frac{1}{\sqrt{2\pi}}\frac{V_0 h}{a}\frac{(\omega-\omega_0)a/v}{v\sinh\{(\omega-\omega_0)a/v)\}}. \tag{2.44}$$

The FWHM is $\Delta\omega=4.4(v/a)$ and we note that in this expression the effective length of the interaction region is the separation, not the width of the plates. In terms of a frequency the expected FWHM is $\Delta f=16.4$ kHz and it is in excellent agreement with what we observed.

2.6.6 State Selector Resonances

First of all we were interested in the efficiencies of both AJ and DK transitions at each state selector. As a direct measure of them the resonance strengths were compared with the number of focussed molecules, a quarter of which could participate in either of the transitions. The efficiency of the A state selector tuned to the AJ transition, a(AJ), is defined by,

$$a(AJ)=\frac{A_{RES}(AJ)}{(FOC/4)}, \tag{2.45}$$

where $A_{RES}(AJ)$ is the number of molecules for a unit time that undergoes a transition from A to J at the A state selector. Similar definitions can be made for the B state selector and for the DK transitions. Given the focussed beam (FOC) of 4.4×10^8 molecules/sec at quadrupole voltage $U_o=9$kV, the resonances at the A state selector were measured to be

$$A_{RES}(AJ)=8.31\pm0.33\times10^7 \text{molecules/sec} \tag{2.46.a}$$

$$A_{RES}(DK)=6.65\pm0.33\times10^7 \text{molecules/sec} \tag{2.46.b}$$

and similar signal strengths were observed for the B state selector. These numbers could be converted into a(AJ)=75 ± 3% and a(DK)=60 ± 3%.

In an attempt to check these results we devised a different and complementary method in which we observed the resonance strength of one state selector while the other was being turned on and off. In this case one can show that the efficiency of the A state selector on transition AJ is given by

$$a(AJ) = \frac{1}{2}\left(1 - \frac{B_{RES}(AJ)[A_{RF}(AJ) = ON]}{B_{RES}(AJ)[A_{RF}(AJ) = OFF]}\right), \tag{2.47}$$

and similar expressions give efficiencies for the B state selector and for the DK transitions. In this way the AJ transition efficiency was again found to be $75 \pm 3\%$ for both state selectors. But now we also measure $75 \pm 3\%$for both state selectors on the DK transitions while the absolute strengths of the DK transitions were still consistently smaller than the AJ by as much as 20%. The most obvious explanation for the smallness of the DK signal is that we lose about 20% of the molecules in the state D after they are focussed.

Other than the 20 % loss in the state D there were no unwanted transitions that interfered with our state selections. When either of the RF fields in the state selectors was turned off the NMR became invisible, and a long integration was needed to observe any residual signal. There was indeed a residual signal with the state selectors turned off and this was identified to be from the J=2 manifold. This background was below 1.0% of the regular NMR strength with both RF fields on. Its effects on the EDM measurement are discussed in §§ 3.4.4.

The results of the second measurements of the resonance efficiencies also indicated that neither of the states J or K lost their polarization after they were populated. As a more direct investigation we scanned through various NMR lines in search of any states accidentally populated from either J or K, and once again no significant signal was detected. Finally, because of the relatively large linewidth of the resonances the AJ and DK transitions were not well separated from the nearby ones (§§ 2.6.3). Using the lineshape of Eq. (2.44), we estimated that 3% of the CL transition was accompanying the AJ resonance and 10% of BI was present in DK. These were not negligible numbers, but the nuclear

magnetic resonances associated with either of L or I were at least 10 kHz away from the NMR of J or K, and they did not affect our EDM measurements because the NMR line-width was narrow.

2.7 Nuclear Magnetic Resonance Region

In this region, which is the heart of the machine and traditionally called the C region, a transition between two hyperfine levels is driven by a pair of separated oscillating magnetic fields while the molecule is in a polarizing electric field (E_C). The transition is in essence the flipping of a Tl nuclear spin which is coupled to the magnetic field produced by the rest of the molecule; this is why it is called nuclear magnetic resonance. A schematic diagram of this region is shown in cross section in Figure 2.15. For the convenience of the descriptions the region can be considered as consisting of three different functional parts; i) a pair of parallel electric field plates (C plates) that provides up to 30 kV/cm and a few grounded cylinders (electric shields) to shield the molecules from an influence of static charges on the Pyrex tube, ii) the magnetic shield that keeps the ambient fields away from the NMR region and the magnetic field coil for final compensation, and iii) a pair of RF coils that drive the transitions by the separated oscillating fields method. Before we go into the mechanical or electronic details we need to consider the Stark shift of the molecule again, this time from the point of view of the NMR transitions for the EDM measurement.

2.7.1 Stark Effect in the NMR region

The Stark effect of a TlF molecule in both strong and intermediate fields was already discussed in the context of focussing and state selection. In the NMR region we have E_C, which is about three times larger than the field inside the quadrupoles, and the groups with different $|M_J|$'s are again well separated (although, the focussing would not have worked at this high field). The nuclear magnetic resonances are to be induced either between J and E or K and H (the JE or KH transition), all belonging to the group of $|M_J| = 1$. The levels of the group at 29.5 kV/cm are shown in Figure 2.16. From the diagram we note that

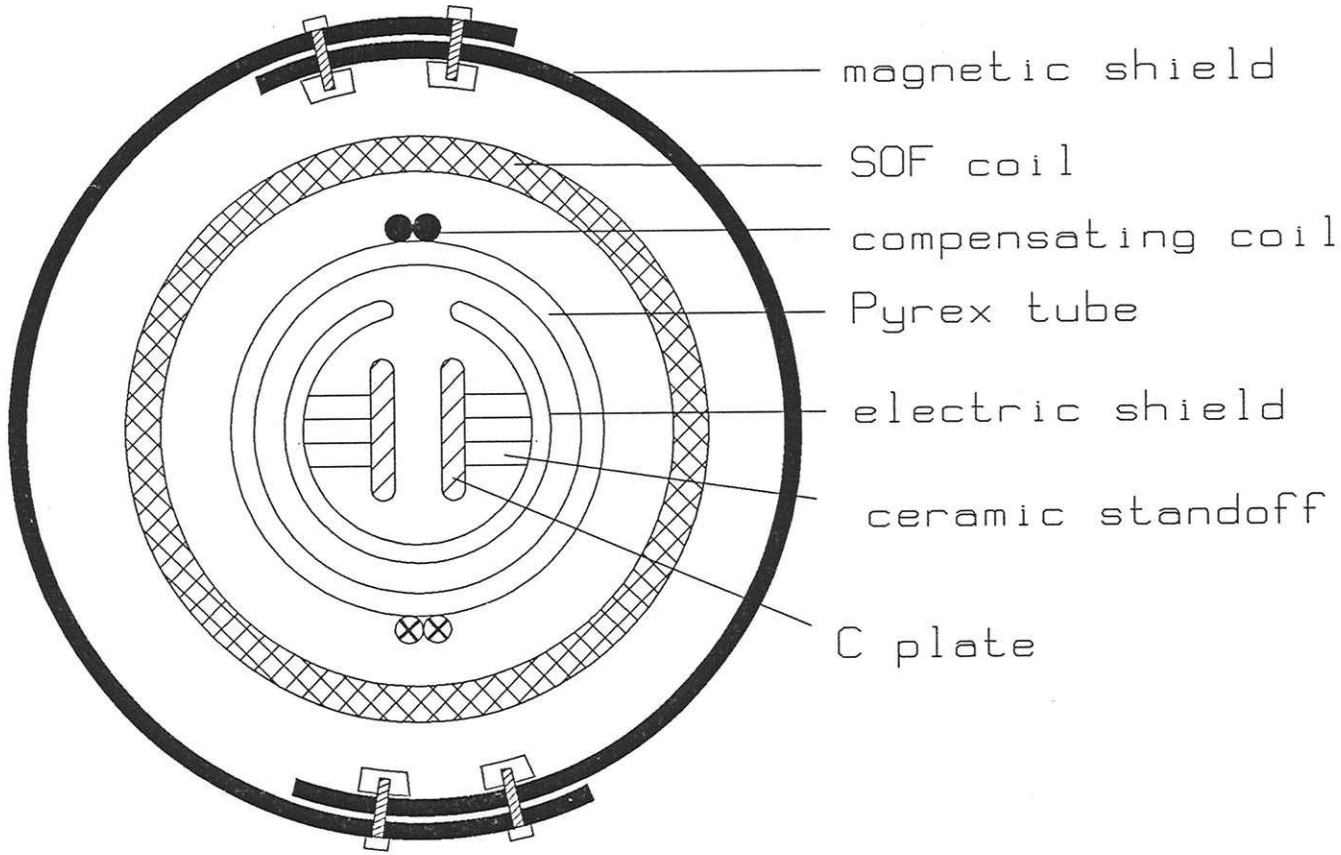

Fig 2.15 Cross section of C Region

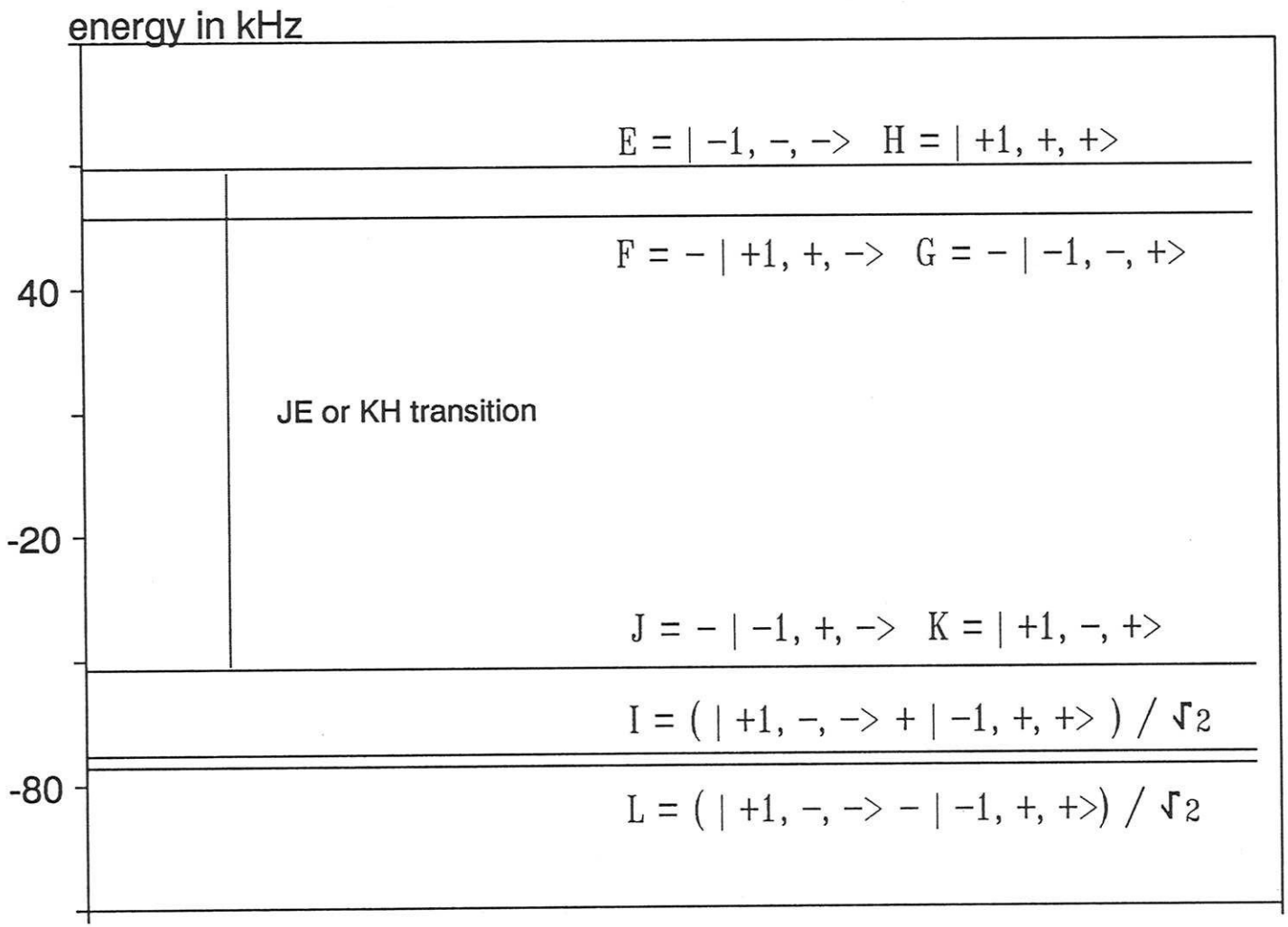

Flg 2.16 J=1, Mj=±1 energy levels at Ec=29.5 kV/cm

the absence of an external magnetic field leaves some pairs of states degenerate. These are the Kramers doublets - the states are the time-reversed versions of each other - mentioned in § 1.1. On the other hand, those pairs with $M_F = 0$ are coupled to make symmetric and antisymmetric combinations (the states I and L). The tensor interaction of the two nuclear magnetic dipoles, which commutes with the z component of the total angular momentum but not of the individual angular momenta, is responsible for the coupling. As alternatives to JE or KH, there are four possible transitions from the state F or G to the state I or L, which also involve a spin flip of the thallium nucleus and are sensitive to the proposed T-violating Hamiltonian $H_{PT} = -hd\vec{\sigma} \cdot \hat{\lambda}$. We note, however, that because the states I and L have zero net projection of $\vec{\sigma}$ along the quantization axis, those transition frequencies are only half as sensitive to H_{PT} as the ones we used for the measurement.

Now we focus our attention on the transitions, JE or KH, which we used. The resonance frequency is mainly determined by the interaction $C_1(\vec{I}_{Tl} \cdot \vec{J})$ and is only weakly shifted by the applied electric field E_C. In fact at 29.5 kV/cm, the field we used, the NMR frequency is 119.57 kHz and the variation of the Stark shift with the electric field is

$$\frac{df_0}{dE_C} = -41 \frac{\text{mHz}}{\text{V/cm}}. \tag{2.48}$$

This slope remains constant over a wide range of E_C, and is primarily a consequence of the change in the spin rotation coupling as a molecule becomes stretched in the field. Another quantity of interest here is the degree of polarization, a measure of how well the polar molecule is aligned with the applied electric field. It is one of the variables in the experiment that is directly related to the sensitivity of the measurement and is considered in a rigorous way when we interpret the results of the runs (§ 4.1). In this section we simply note that the polarization at the operating electric field of 29.5 kV/cm was 0.542.

2.7.2 Electric Field Plates and Shields

Each of the two field plates was 245 cm long, 7.6 cm wide, and 0.95 cm thick, and made of aluminum for its nonmagnetic property and for ease of machining. Their surfaces were polished with a great care and all the corners were rounded smoothly. The plates were then held together by four aluminum rings through 2.54-cm long ceramic standoffs so that the gap between the plates was 2.0 cm. The holding rings had adjustable Teflon feet on which the whole assembly could slide into the long Pyrex tube. The high voltages of positive and negative 29.5 kV were then supplied through connecting rods from the high voltage feedthroughs on the octagon to connectors placed on the outer sides of the plates. The rods were made of brass and insulated with thick glass tubing.

In the measurements, where we aimed at a final sensitivity of 0.1 mHz in the resonance frequency after roughly 100 hours of data taking, even an instability of $\Delta E_C = 1.0$ V/cm over a minute, which converted into $\Delta f = 40$ mHz, was intolerable and many efforts were made to maintain the electric field absolutely stable for a long period of time. Besides the stability problem, another consideration here was that of exact reversal of the field to avoid a shift in the resonance frequencies. Exact reversal of the potentials was made possible with a homemade high voltage relay, but there was still some non reversing field generated by the static charge accumulated on the inside of the Pyrex tube. Five aluminum cylinders with inner diameter of 12.7cm were used to line the tube and they were electrically grounded so that the molecules were no longer exposed to the influence of the static charges. They were very successful in reducing the stray field (§§ 3.3.1). These aluminum cylinders were also polished and rounded, and we put a 1.0-cm wide slot through each one to keep them from developing azimuthal eddy currents and interfering with the RF currents that drove the NMR transitions.

Finally, in constructing the field plates and their connectors we paid special attention to possible paths for leakage currents from one side of the electrode to the other - or to the surroundings. Such current could generate magnetic fields dependent upon the polarity of E_C and complicate the EDM measurement in a significant way (§§ 3.3.4). The ceramic

standoffs on the holding rings and the thick glass tubing around the connecting rods provided good insulation as well as mechanical support. The relevant resistances at the operating high voltage were all measured to be in excess of 10^{13} ohms which proved to be large enough.

2.7.3 C High Voltage Relay

The electric field, E_C, in the NMR region was generated by two 50 kV supplies (Bertan 205A-50P/N). This field was reversed by a high voltage relay placed between the supplies and the plates. The importance of an exact field reversal has already been emphasized in the previous section, and it was essential to have a reliable high voltage relay for it. It was a demanding requirement to reverse voltages of ±30 kV within an accuracy of 0.1 V and the frequent failures of commercial relays led us to make one ourselves. The heart of our design was a 10-cm diameter Lucite rotor holding a pair of symmetrically placed stainless steel arcs (Figure 2.17). Each of them covers slightly more than a quarter of the circumference and could connect one input to one output. The relay was then a DPDT type and a rotation by 90 degrees in either direction switches the connections. Each of the input and output posts was a spring-loaded bronze roller to ensure good contact with the arcs while minimizing friction. The assembly was placed in an aquarium filled with transformer oil like the relays for the quadrupoles. Finally, torque for the rotation was provided by an ac motor whose motion was "quantized" into a quarter of a turn either clockwise or counterclockwise by the computer control and limit switches.

After quite a few modifications and improvements the relay worked reliably for long enough for us to make a series of EDM measurements. It reversed the voltages very precisely and we observed no relay-induced systematic effects. Still mechanically it leaves something to be desired because it needs frequent adjustments and it should be improved in the next phase of the experiment.

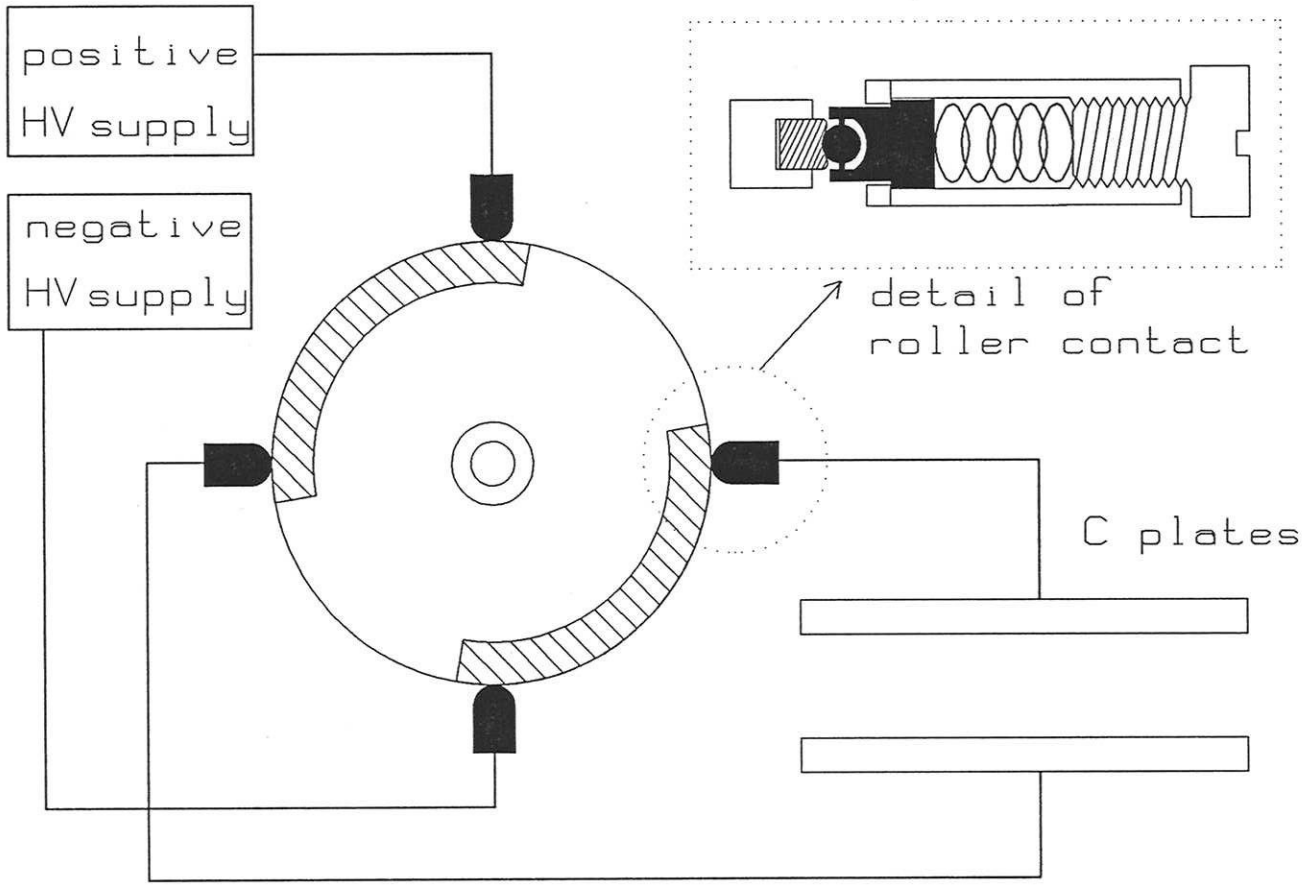

Fig.2.17 C-region HV relay

2.7.4 Magnetic Shield and Compensating Coil

In the NMR region we apply only the electric field, and any magnetic field interacting with the thallium nuclear spin is supposed to be internal. Of course, in practice there are always some ambient magnetic fields present in the laboratory, most notably the earth's field. We placed a large magnetic shield around the NMR region to exclude the ambient fields. The magnetic shield was a set of four half cylinders which, when assembled, extended over 3 meters and covered the whole length of the NMR region at a diameter of 30 cm. They were made of 0.1-cm thick high permeability material (Ad-MU 80) which were annealed by the manufacturer to increase the permeability even further. In our machine this was originally estimated to be 8.0×10^4, which we tried to preserve by the careful handling. After each reassembly we degaussed the shield by flowing AC current of a few tens of amperes through a coil of six turns wound around one side of the shield lengthwise.

Without the shield we estimated that the ambient magnetic field strength along the direction of E_C (z axis) was 120 mgauss which was then reduced to 1.0 mgauss after the shield was installed. Instead of investing in more shielding we compensated the small residual field with a coil (Figure 2.15) that had been glued onto the Pyrex tube lengthwise to produce uniform field along the z axis. It took about 3.5 mA through the coil to null out the remaining field, and this needed to be adjusted between runs to follow the fluctuation of the ambient fields. In the actual operation of the machine to measure the EDM we found more applications of the compensating coil to deal with other types of the stray magnetic fields (§§ 3.3.1). Because the shield worked very poorly along the axis of the beam machine, the field component in that direction was of order 100 mgauss. However the magnetic field of this size perpendicular to the z axis did not induce any significant effects in our measurement.

2.7.5 Separated Oscillating Fields Method

The magnetic dipole transition of the Tl nuclear spin was induced by the technique of separated oscillating fields (SOF). The method, which is due to N. Ramsey [RAM56], is basically amplitude modulation of the RF power; as the molecule flies through the two separated fields it experiences two bursts of RF power. This results in a narrow linewidth and a lineshape convenient for the detection of small frequency shifts. It was a great innovation over a more direct way of subjecting a molecule to a constant RF power longer and longer to get a narrower linewidth, and it has been a method of choice for EDM and other sensitive measurements since its invention.

Considering the SOF technique in a semiclassical picture, a spin parallel to a static magnetic field B_0 along the z axis is first flipped through an angle $\pi/2$ into the xy-plane under the influence of the first RF magnetic field. The spin then evolves freely for a time T until a second RF field, having a definite phase relation with the first one, acts on the spin again. Here the RF fields are rotating magnetic fields of strength b in the xy-plane with a frequency ω. The motion of the spin can be understood most easily in a reference frame also rotating with frequency ω, in which the first rotating field is fixed along the x′ axis. Then the halfway spin flip is a consequence of its precession about the x′ axis and as a result of the free evolution its azimuthal angle increases by $\phi = (\omega_L - \omega)T$. Here $\omega_L = \gamma B_0$ is the Lamor frequency of the spin with γ being the gyromagnetic ratio and it is the same as the nuclear magnetic resonance frequency $\omega_0 = 2\mu_\Pi B_0/\hbar$. When the second rotating field which makes an angle δ to the x′axis comes in, its effectiveness in completing the spin flip depends on the azimuthal precession angle ϕ as well as the angle δ.

Quantum mechanically, the transition probability $P(\delta)$ can be most easily calculated by using rotation operators,

$$|\Psi_f\rangle = \exp\left(-\frac{i}{\hbar}\vec{S}\cdot\hat{u}\theta\right)\exp\left(-\frac{i}{\hbar}S_Z\phi\right)\exp\left(-\frac{i}{\hbar}S_X\theta\right)|+\rangle \tag{2.49}$$

and

$$P(\delta) = |\langle -|\Psi_f\rangle|^2,$$

where $\theta = \gamma b\tau$, τ being the interaction time with each RF field,

$\phi = (\omega_0 - \omega)T$,

and $\hat{u}$ is along the second RF filed.

The expression for the transition probability is

$$P(\delta) = \sin^2(2\omega_R\tau)\cos^2\frac{1}{2}((\omega_0 - \omega)T - \delta), \tag{2.50}$$

where the identification of $\gamma b/2$ to the Rabi frequency ω_R was made. A treatment of the problem based on the time dependent Schroedinger equation gives the same result when ω is near the resonance. We note that the precession angles are halved in Eq. (2.50) in comparison with the classical picture, a characteristic of a rotation of spin-$\frac{1}{2}$ system.

From Eq. (2.50) the RF powers are optimal when

$$\omega_R\tau = \frac{\pi}{4}. \tag{2.51}$$

A most useful lineshape can be obtained by subtracting transition probabilities for two different values of δ. When we define

$$L(\delta_1, \delta_2) = P(\delta_1) - P(\delta_2), \tag{2.52}$$

the combinations of $(\delta_1,\delta_2) = (+\pi/2, -\pi/2)$ and $(0, \pi)$ yield

$$L(\pi/2, -\pi/2) = -\sin((\omega_0 - \omega)T) \tag{2.53.a}$$

$$L(0, \pi) = \cos((\omega_0 - \omega)T) \tag{2.53.b}$$

In the experiment we measure the number of molecules undergoing the transition at a fixed frequency ω near the resonance using two different phases δ_1 and δ_2. The measured difference is

$$S = I_0 L(\delta_1, \delta_2), \tag{2.54}$$

where I_0 is the number of molecules available for the transition. In this case a shift in the resonance frequency and a change in the number of available molecules would appear as

$$\Delta S = I_0 \frac{\partial L(\delta_1, \delta_2)}{\partial \omega_0} \Delta\omega_0 \tag{2.55.a}$$

and

$$\Delta S = L(\delta_1, \delta_2) \Delta I_0 \tag{2.55.b}$$

respectively. It follows that near the resonance, ω close to ω_0, the signal that is most sensitive to a frequency shift and least sensitive to an intensity change is the one with the phase modulation of $(+\pi/2, -\pi/2)$. The reverse is true for $(0, \pi)$ modulated signal. Consequently our EDM measurement was made with the $\pm\pi/2$ modulation.

In the apparatus the free evolution time T is the time of flight for a molecule from one region of oscillating magnetic field to another separated by L_{CC} (215 cm), and $T = L_{CC}/v_z$. Using this expression the signal is

$$S = -I_0 \sin\left[\frac{2\pi(f - f_0)}{v_z/L_{CC}}\right]. \tag{2.56}$$

The period of the sinusoidal oscillation near the resonance, $\Delta F_0 = v_z/L_{CC}$, is referred to as the linewidth of the SOF transition. It is directly related to the sensitivity of the experiment to small frequency shift. Its dependence on the beam velocity was used to study the focussing quadrupoles (§§ 2.5.5) and it will be useful again to understand the two-coil Millman effects (§§ 3.4.1). The overall form of lineshape of the transitions is the oscillatory part contained in Lorentzian envelope whose width is inversely related to the interaction time of the molecules with a single coil. The spread of the molecular velocities can

also introduce some destructive interferences among the oscillatory parts with different periods to reduce the width of the envelope. A typical Ramsey pattern, as it is called, as measured in our apparatus under normal running condition is given in Figure 2.18.

2.7.6 SOF Coils and Electronics

The two rotating magnetic fields were generated by two coils which were placed outside the Pyrex tube and separated by 215 cm. The coils were coaxial with the tube and each one has twenty turns of wire wound on a Lucite cylinder of 21.6 cm diameter and 0.7 cm width and had an inductance of 250 μH. Current through the coil actually produced an oscillating field directed along the beam axis which could be decomposed into two counter rotating fields, only one of which was in resonance with the spin system.

When current I flows through a coil of n turns with a radius R, the magnetic field at a point on the axis of the coil is

$$\vec{B}(x)=\frac{\mu_o nI}{2}\frac{R^2}{(R^2+x^2)^{3/2}}\hat{x}, \tag{2.57}$$

where x is the distance from the point to the center of the coil. Suppose that the current I has time dependence of $I_c \cos \omega t$ and a molecule has velocity v along the beam axis (x). The condition on the field strength, Eq. (2.51), can be satisfied when

$$\frac{1}{2}\gamma\int_{-\infty}^{+\infty} dt\,\frac{1}{2}B(vt)=\frac{\pi}{4}, \tag{2.58}$$

where the factor 1/2 in the integrand is from the rotating field approximation. When the integration is done,

$$\frac{\gamma\mu_o nI_c}{2<v>}=\frac{\pi}{2}, \tag{2.59}$$

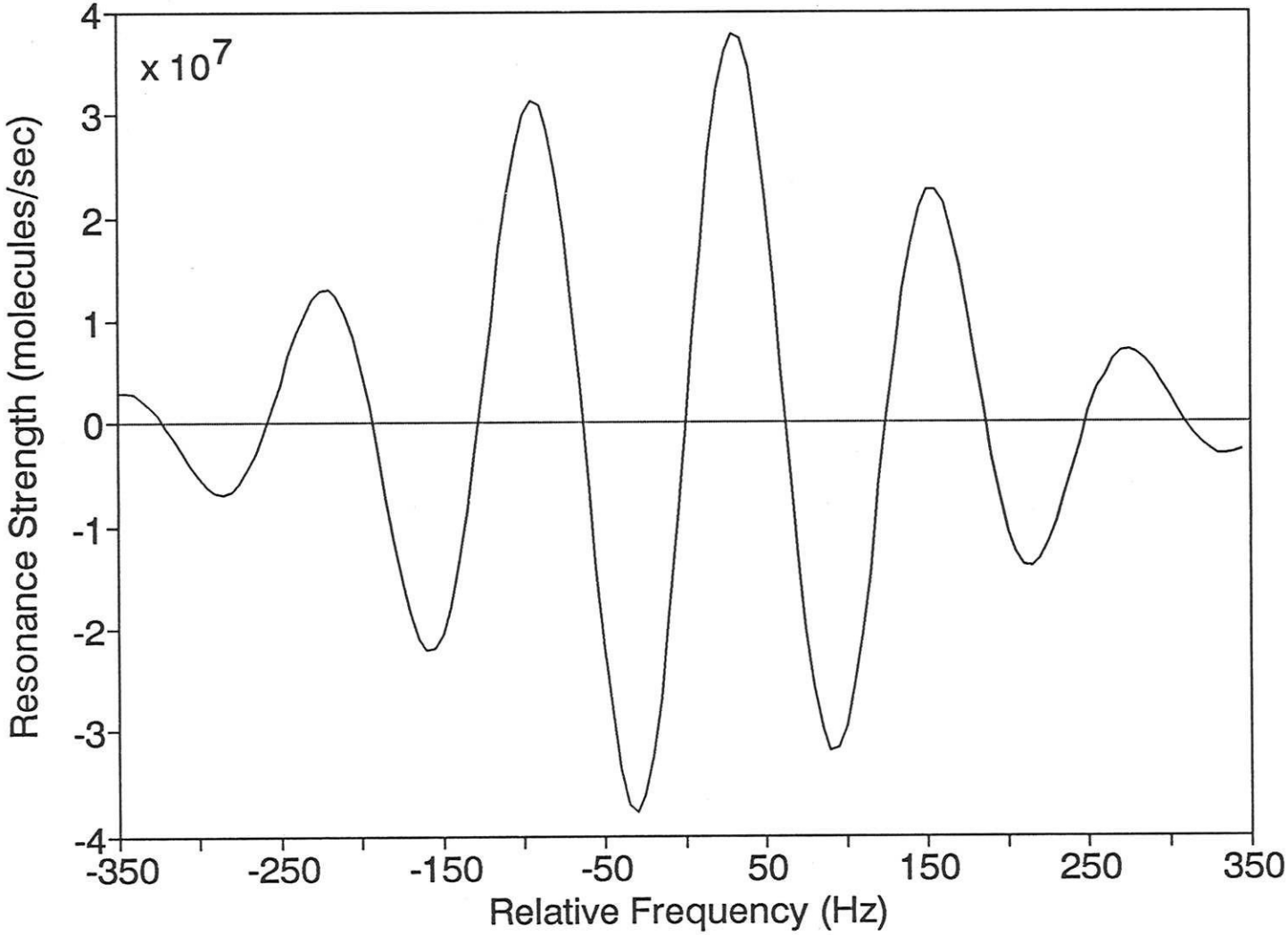

Fig 2.18 SOF resonance curve for JE transition

where $< v >$ is the average beam velocity along the beam axis (this velocity was called $< v_z >$ in §§ 2.5.5). From the parameters of our system, the coils are supposed to work best when I_C is 0.23 A which agreed within a few percent with what we observed.

Turning to the electronics that drove the coils (Figure 2.19), the reference signal was generated by a Hewlett-Packard 501A frequency synthesizer whose output frequency (close to 480 kHz) was controlled by a DAC on the computer with a resolution of 24 mHz. The synthesizer output signal was fed into a phase shifting circuit that split the input into two outputs and introduced a phase difference δ between them. The phase shifter was a logic circuit and the outputs in the form of square waves could have four different phase relations, $\delta = -\pi/2, 0, \pi/2, \pi$, depending on the levels of two TTL signals from the computer. The outputs from the circuit had four times the period of the input and were therefore at the correct frequency (120 kHz). After the phase shifter, each square wave was converted into a sinusoidal one by an active filter. This signal was amplified by a power op-amp (Apex PA-02) to produce an RF current. The output capacitor of the op-amp made a resonant circuit with the coil at 120 kHz as well as blocking a dc component of the output current. A resistor of 10 ohm was also included to broaden the resonance and to monitor the current.

2.7.7 Nuclear Magnetic Resonances

With the quadrupoles and the state selectors ready and the SOF coils working very efficiently we could observe large NMR signals of the JE or KH transition. The number (N) of molecules that are available for the NMR to take place and to be observed is proportional to the efficiencies of the focussing quadrupoles and both state selectors,

$$N = \frac{FOC}{4} \cdot a \cdot b. \tag{2.60}$$

To check the efficiency of the SOF we have to compare the number N with the strength of the NMR. However we note that there are molecules with different thallium isotopes and in higher vibrational states that could contribute to N but not to the NMR.

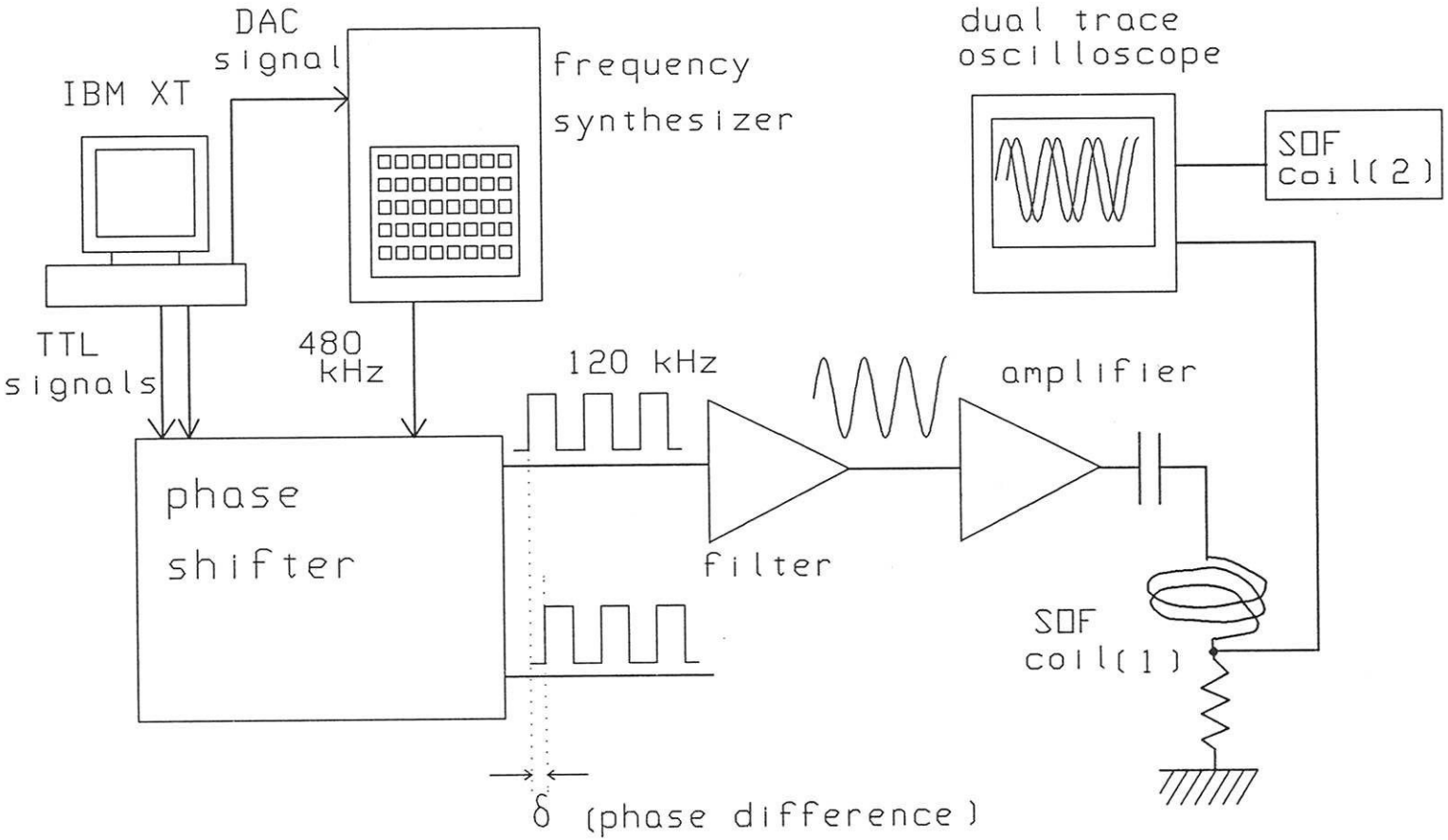

Fig. 2.19 SOF driver

Thallium has two major isotopes, ^{205}Tl and ^{203}Tl, with natural abundances of 70.5% and 29.5%, respectively. Our experiment was done on ^{205}Tl for its larger population. The other isotope also has the nuclear spin 1/2 and magnetic dipole moment slightly different from that of ^{205}Tl (Table 2.2), introducing about 1 kHz of shift in the NMR frequency. While the isotope shift was well resolved in the NMR, it was ignored by the state selector resonances with their large width of 16 kHz and molecules with the ^{203}Tl isotope were just as well selected as those with ^{205}Tl. Similarly the vibrational excitations change the strength (C_1) of the spin-rotation coupling so that the first excited vibrational level (n=1) has its NMR transition about 1 kHz below that of the ground level (n=0). The accompanying changes in the molecular electric dipole moment μ_E and other spectroscopic coefficients are still too small for the quadrupoles and the state selectors to distinguish different vibrational states. Consequently the proper expression for the efficiency of the SOF in driving the NMR is

$$c(JE) = \frac{C_{RES}(JE)}{0.705 \cdot P_{n=0} \cdot FOC/4 \cdot a(AJ) \cdot b(AJ)'} \tag{2.61}$$

where C_{RES} is the strength of the NMR transition from J to E. It is defined as the change in the detected beam flux as the phase difference δ is modulated between 0 and π (in this sense the zero phase difference corresponds to the RF magnetic fields turned on, and π to RF turned off). A similar definition for c(KH) can be given with the 20% deficiency of the DK resonance strength taken into account.

When we scanned the frequency of the SOF near the original JE or KH transition, we could observe clear resonances corresponding to the different isotope and higher vibrational levels up to n=3. Accidentally the isotope shift was very close to the shift from a vibrational excitation and some of the transitions overlapped. It somewhat complicated our attempts to measure the relative strengths of the NMR's from different vibrational levels, the information that was important to estimate the vibrational temperature of the beam (§§

2.2.1). We measured a ratio of 0.18 between two transitions from consecutive vibrational levels, which indicated that the vibrational temperature was $400 \pm 50°K$ and the fractional population, $P_{n=0}$ was 0.82.

With the quadrupole high voltage U_0 set to 9 kV and the state selector resonances as strong as in Eq. (2.46), the main NMR's were measured to be

$$C_{RES}(JE) = 3.78 \pm 0.20 \times 10^7 \text{ molecules/sec} \tag{2.62.a}$$

$$C_{RES}(KH) = 3.00 \pm 0.20 \times 10^7 \text{ molecules/sec.} \tag{2.62.b}$$

which correspond to 97% efficiency of the SOF. We note that from the observed signal strengths the vibrational temperature cannot be much higher than 400 °K, since that could imply an SOF efficiency larger than 100%.

2.8 Computer and Its Interface

So far in this chapter we have described design, construction, and operation of each part of the machine. To make an EDM measurement or simply to observe a resonance signal a coordinated operation is required and a computer was in charge of it. A personal computer (IBM XT) controlled the phase and frequency offsets of the SOF coils as well as the polarities of the electric and magnetic fields. It also set the state selector transitions to either AJ or DK, and read in and store the digitized detector outputs as the various running parameters were changed. To execute the operations on the apparatus, however, the computer needed an interface that could link it to the apparatus and we used a plug-in board for laboratory applications (Tecmar LabMaster). To make the hardware work as desired we developed a program devoted to the operation of the machine. The details of the software, both to control the machine for data taking and to analyze the numbers obtained thereby, are the subject of the next chapter.

2.9 Summary

In concluding this chapter we summarize some of the important parameters of the apparatus and its operation. In Table 2.4 we put together the operating conditions of the beam machine. The characteristics of the jet beam and the resonance strengths under those conditions are given in Table 2.5 and 2.6 in which N is supposed to mean the number of ions or molecules per second. It is pleasing to compare the numbers from the new jet source with those of the effusive source that was used for the previous version of this experiment [SCH88]. The strength of the JE transition has been increased by a healthy factor of 50 even though the quadrupoles now work at half of their best efficiency due to the reduced voltages (§§ 2.5.5). Such an improvement in the signal strength came with only 2.5 times larger background (from detector and scattered beam). However the total number of molecules detected per unit time (DC) includes the focussed beam as well. Because of an increase in FOC, DC as a whole has gone up by a factor of 4.

Now with all of the numbers at hand it is interesting to estimate expected sensitivity in the EDM measurement. Starting from the lineshape of the SOF at $\pm\pi/2$ modulation (Eq. 2.56), a change in the resonance frequency (δf) can be related to the change in the signal strength observed for a unit time (δS) by

$$\delta S = \frac{\pi C_{RES}}{\Delta F_O}\delta f. \tag{2.63}$$

When this is compared with the random noise contributed from the detector and scattered background and the focussed beam, the shot-noise limited sensitivity is

$$\delta f = \frac{\Delta F_O}{\pi C_{RES}}\sqrt{\frac{DC}{T_D}}, \tag{2.64}$$

where DC is the sum of BG, SC, and FOC and T_D is the total data taking time. Using the numbers from the tables we find for the DKH scheme and 1 second of integration the expected uncertainty is 44 mHz. In fact the sensitivity we actually achieved was close to this shot-noise limited value (§ 3.5).

parameters	place	numbers
pressures	source	$P_{SS} = 1.0 \times 10^{-7}$torr
	detector (oxygen off)	$P_{DD} = 0.5 \times 10^{-7}$torr
	detector (oxygen on)	$P_{DD} = 3.0 \times 10^{-7}$torr
	source side quadrupole	$P_{SQ} = 0.8 \times 10^{-7}$torr
	detector side quadrupole	$P_{DQ} = 0.8 \times 10^{-7}$torr
temperatures	oven (liquid TlF)	$T_L = 753°K$
	nozzle (gaseous TlF)	$T_G = 773°K$
	detector filament	$T_D = 1200°K$
high voltages	quadrupoles	$U_O = 9kV$
electric fields	state selector	$E_{SS} = 35V/cm$
	C region	$E_C = 29.5kV/cm$
magnetic fields	state selector	$B_{SS} = 27gauss$
resonance frequencies	AJ transition	$f(AJ) = 300kHz$
	DK transition	$f(DK) = 197kHz$
	JE/KH transition	$f_O = 119.57kHz$

Table 2.4 Operating conditions of the beam machine

detector background	N(ion) emitted from detector filament $BG = 7.5 \times 10^7$ ions/sec.
total output	N(TlF) emitted from source $TO = 1.8 \times 10^{16}$ molecules/sec (estimated)
full beam	N(TlF) detected without beam stop $FB = 1.25 \times 10^{10}$ molecules/sec
-- monomer fraction	Fraction of N(monomer) in the FB $r_m = 0.92$
-- vibrational fraction	Fraction of N(n=0) in the FB $P_{n=0} = 0.82$ (or $T_{vib} = 400°K$)
-- rotational fraction	Fraction of N(J=1) in the FB $P_{J=1} = 2.7 \times 10^{-3}$ (or $T_{rot} = 350°K$)
scattered background	N(TlF) scattered around the beam stop $SC = 4.4 \times 10^8$ molecules/sec

Table 2.5 Jet beam characteristics

focussed beam	N(TlF) focussed at U_o =9kV
	FOC = 4.4×10^8molecules/sec
-- focussing efficiency	Ratio of FOC to N(focussable) in the FB
	$\kappa = 43$
A state selector	N(TlF) from A to J by A_{RF}
resonance (AJ)	$A_{RES}(AJ) = 8.3 \times 10^7$molecules/sec
-- its efficiency (AJ)	Ratio of $A_{RES}(AJ)$ to N(A) in the FOC
	a(AJ) = 0.75
A state selector	N(TlF) from D to K by A_{RF}
resonance (DK)	$A_{RES}(DK) = 6.7 \times 10^7$molecules/sec
-- its efficiency (DK)	Ratio of $A_{RES}(DK)$ to N(D) in the FOC
	a(DK) = 0.60
C resonance (JE)	N(^{205}TlF, n = 0) from J to E by the SOF
	$C_{RES}(JE) = 3.8 \times 10^7$molecules/sec
-- its efficiency (JE)	Ratio of $C_{RES}(JE)$ to the available N(J)
	c(JE) = 0.97
C resonance (KH)	N(^{205}TlF, n = 0) from K to H by the SOF
	$C_{RES}(KH) = 3.0 \times 10^7$molecules/sec
-- its efficiency (KH)	Ratio of $C_{RES}(KH)$ to the available N(K)
	c(KH) = 0.97

Table 2.6 Focussing and resonance strengths

CHAPTER 3

MEASUREMENT

In Chapter 2 we described the experimental apparatus that generated a beam of TlF molecules, polarized the angular momenta, induced the Tl nuclear magnetic resonances, and finally detected them. With this hardware and the signals available we could measure the electric dipole moment of the molecule to look for a T-violating effect. In this chapter we discuss the strategies to extract informations on the EDM from the observed NMR signals and describe how those ideas were implemented in the computer program that controlled the machine and ran the experiment. As in any other precision measurements, in this TlF experiment our major concerns have been twofold; to make the ratio of signal-to-noise as large as possible (sensitivity), and to guard against systematic effects that could lead us to a wrong conclusion (specificity). With the signal-to-noise ratio increased by more than an order of magnitude the task of distinguishing an artifact from a true EDM became much more important because all the minute effects that used to be hidden by noise were now apparent.

3.1 Phase Sensitive Detection

The NMR signal near the zero crossing part of the lineshape is small compared to the detected beam of TlF, either scattered or focussed, and we intend to measure the EDM-induced frequency shift of the NMR as small as 0.2 mHz which is approximately 2 parts per million of the linewidth. Such small signals can nevertheless be observed by the technique of

phase sensitive detection where one changes a parameter that has a direct effect on only the signal and observes how the outcome of the experiment responds to the change. In the TlF experiment we have two groups of such parameters, phase (P) and frequency offsets (F) to observe the NMR signal itself, and three independent reversals of the electric fields (E), the magnetic fields (B), and the magnetic quantum numbers (M) which were used to measure the EDM.

3.1.1 Phase and Frequency Modulations

The first step of our EDM measurement is to put the Tl NMR line into a form which is most suitable for detecting a small change in a resonance frequency. As was already discussed (Eq. 2.58), the curve crosses zero at resonance and has the largest slope there when the phases are changed between $\delta = \pm\pi/2$. We call the periodic change in the phases the P modulation. The resulting lineshape near the resonance (Eq. 2.59) can be approximated as a straight line,

$$S = -2\pi I_0 T(f - f_0), \tag{3.1}$$

where T, the transit time between the two coils, is related to the linewidth by $T=1/\Delta F_0$. We note that, at resonance ($f = f_0$), $\partial S/\partial I_0=0$ and the signal strength S is completely insensitive to the change in the intensity I_0.

In addition to the P modulation we change the oscillator frequency between two values f_+ and f_-, above and below the resonance by an amount F.OFFSET = 1.25 Hz. This hopping in frequencies, the F modulation, is employed to monitor the slope of the line which is needed to interpret a change in the observed signal strength as a shift in the resonance frequency. Incidentally, this offset from f_0 keeps the derivative $\partial S/\partial I_0$ from vanishing and allows us to measure a change in the intensity of the resonance as well.

3.1.2 E, B, and M Reversals

The energy of the Tl nucleus ($\vec{\sigma}$) in the C region can be effectively described by the Hamiltonian,

$$H_C = -\vec{\sigma} \cdot (\mu_{Tl}\vec{B}_0 + dh\hat{\lambda}) \tag{3.2}$$

where μ_{Tl} is the magnetic dipole moment of the Tl nucleus, $\vec{B}_0$ is the internal magnetic field of the molecule, and $\hat{\lambda}$ is a unit vector from the Tl nucleus to the F nucleus (Eq. 1.33). We note that in this effective description $\vec{\sigma}$ is the only quantum mechanical operator, leaving $\vec{B}_0$ and $\hat{\lambda}$ as field vectors external to the Tl nucleus. These field vectors are determined by the electric field in the C region and by the particular state of the molecule which was chosen by the state selectors. As can be seen from Figure 3.1 when the electric field is reversed - the E reversal - the unit vector $\hat{\lambda}$ changes signs while $\vec{B}_0$ remains unchanged, and the new Hamiltonian is

$$H_C' = -\vec{\sigma} \cdot (\mu_{Tl}\vec{B}_0 - dh\hat{\lambda}). \tag{3.3}$$

Formally the E reversal amounts to be a parity transformation and we observe that

$$H_C' = PH_CP^{-1}. \tag{3.4}$$

When we reverse the electric field in the NMR region, we also flip those in the state selectors and the quadrupoles so that the evolution of a molecule throughout the machine is governed by the parity transformed Hamiltonian. Now comparing the Hamiltonians we note that, if the coupling constant d is non-zero, upon the E reversal there will be a shift $4d < \vec{\sigma} \cdot \hat{\lambda} >$ in the Tl NMR frequency.

In the same way we may consider a time reversal transformation of the Hamiltonian in Eq. (3.2)

$$H_C'' = +\vec{\sigma} \cdot (-\mu_{Tl}\vec{B}_0 + dh\hat{\lambda}), \tag{3.5}$$

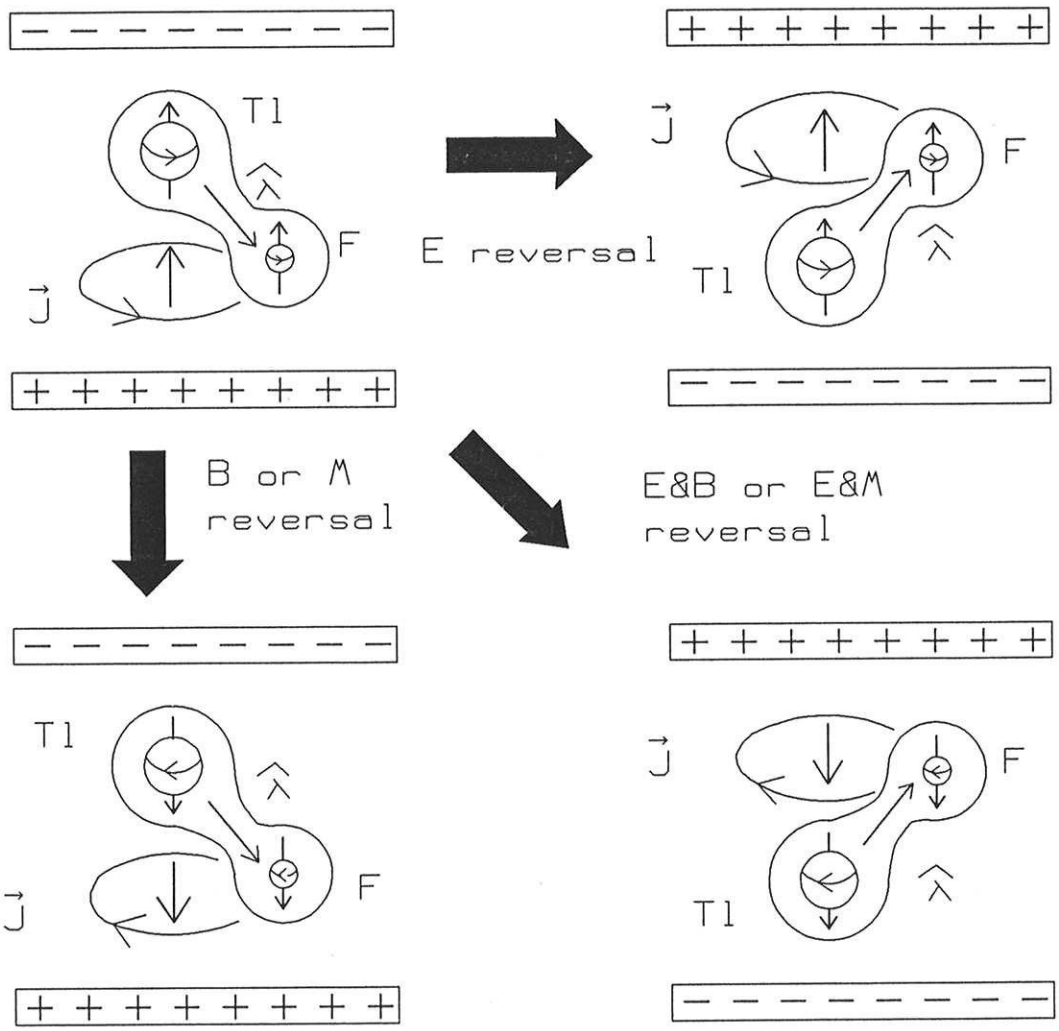

Figure 3.1 E.B and M reversals

which is identical to Eq. (3.3). Experimentally this is accomplished by reversing all the angular momenta of the molecule leaving the orientation of $\hat{\lambda}$ unchanged, Figure 3.1. In practice it turns out that there are two different ways of making the transformation. The first is to simply flip the magnetic fields in the state selectors thereby choosing the state with the same angular momenta, but referred to an inverted z axis. The second is to retune the state selector RF fields so that a state can be selected in which all the angular momenta are reversed while the z axis is unchanged. The former is called the B reversal and the latter the M reversal. In the M reversal the state selectors are alternately tuned to the AJ and DK transitions to study the JE and KH transitions in the C region respectively (hence the name AJE and DKH schemes). We note that the states J and K are the time reversed versions of K and H respectively as can be seen from Table 2.3 or Figure 2.16. More precisely the pairs (J,K) and (E,H) are not simply related by a time reversal transformation when the molecules are in the state selector where there is a magnetic field. It is only when they reach the C region without a magnetic field that they become degenerate Kramers doublets.

In contrast with the case of the time reversal transformation, there is no degeneracy in the molecular states of interest associated with the parity transformation. This is the reason there is only one experimental reversal corresponding to parity - namely the E reversal - while there are two for the time reversal. In fact even if there were degenerate pairs related by the parity transformation in a free molecule, the applied electric field in the C region would lift the degeneracy.

In the experiment the three reversals were made in a predetermined sequence and equal amount of data taking time was devoted to each of eight (2^3) possible configurations. The advantage of having three independent ways of detecting an EDM over just one proved to be enormous in both studying and eliminating various systematic effects. The situation can be compared to repeating a very complicated calculation to make sure first result was correct. In the second attempt it would be a better idea to try a different approach rather than duplicating the first calculation and possibly making the same mistakes on the way.

3.1.3 Manual Reversals

Each of the three reversals was made by relays driven by a computer. While the ideal relays were supposed to make the switching without introducing unintended changes in either the switched or the ambient fields, there were always some modifications in the fields accompanyed by the relay actions. For example in making an E reversal the potential differences between the two relay outputs before and after the reversal were different and also there was an ambient magnetic field that depended on the state of the relays. This type of effect could lead to a confusing or even wrong result for the experiment. A simple way to check for this problem was to repeat the measurements after swapping the connections from the outputs of the switching devices to the field plates or the magnets in the beam machine so that the same state in the electronics and relays would lead to the opposite state in the machine. We call it the manual reversal.

There were four types of manual reversals; E, B, M, and Q. In contrast to the regular E reversal, the manual one did not include swapping cables for the quadrupoles. Instead we had a separate manual reversal for them because the experiment should work equally well with either sign of quadrupole voltage. The reconnections were done between runs and a complete set of runs was supposed to consist of 16 different combinations of manual E, B, M, and Q connections. We note that for a given computer command the actual field directions with respect to the laboratory frame - from the hallway to window or the other way around - could be different depending on the manual connections and to make a proper interpretation of the data those "manual factors" obviously had to be included in the final analysis.

3.2 Programs

A fairly elaborate program was written in the programming language Forth. It controlled all of the modulations and the reversals, read in the digitized detector output, did online analyses and stored the numbers for later examination. In preparing the software, the signal-to-noise ratio and the systematics were again our major concerns.

3.2.1 Data Taking

It takes some time after each reversal for the apparatus to respond and reach a steady state under the new condition. We used 1 kHz clock cycle derived from an interface board to set the pace of the experiment and hence 1 msec was the basic unit of time. The next order of time scale came from the flight of a molecule which took about 17 msec from source to detector. The detector itself has a finite response time as well and 20 msec was taken as a suitable wait time after each change. We call it the DEAD interval. For modulations of P, F, and M the DEAD interval was essentially all it took to complete the changes, while for those of B and E there were relays with mechanical motions involved and the relaxation times for the fields themselves were also long. To a B reversal we allotted 1.25 second for the relays to act and for inductive transient effects to subside. It was even worse for an E reversal where the high voltages were first turned off, their polarities reversed, and finally turned back on. Typical running parameters were 6 seconds of wait time after turn-off, 1.25 second in switching the relays and 12.5 seconds of waiting after turn-on, i.e. altogether the gating time was 20 sec.

Given different gate times it was rational to do modulations with the shortest gate time most frequently, and ones with the longer waiting less frequently to achieve maximum duty factor of data taking. Therefore the innermost loop of the program - PMF.LOOP (see Figure 3.2) - had a sequence of P, M, and F reversals while reading in 128 numbers which, as a whole, we call a BLOCK. This was made up of 4 divisions each containing 32 numbers and each corresponding to a fixed value of the F parameter which was set in the sequence (+F,-F,-F,+F). We call this (+,-,-,+) switching pattern "mode 4". Each division in turn consisted of 4 subdivisions of 8 numbers, and for each of the subdivisions the M parameter was fixed in the order of (+M,-M,-M,+M). Finally, the 8 numbers in a subdivision were taken under the P modulations of (+P,-P,-P,+P,-P,+P,+P,-P). This switching pattern, (+,-,-,+,-,+,+,-), is called "mode 8". In summary, the P modulation of mode 8 was nested in the loop of M with mode 4 which, in turn, was nested in the F of mode 4. We note that a switching pattern of mode 2^n is not a simple juxtaposition of two smaller patterns of mode 2^{n-1}, but one of them followed by

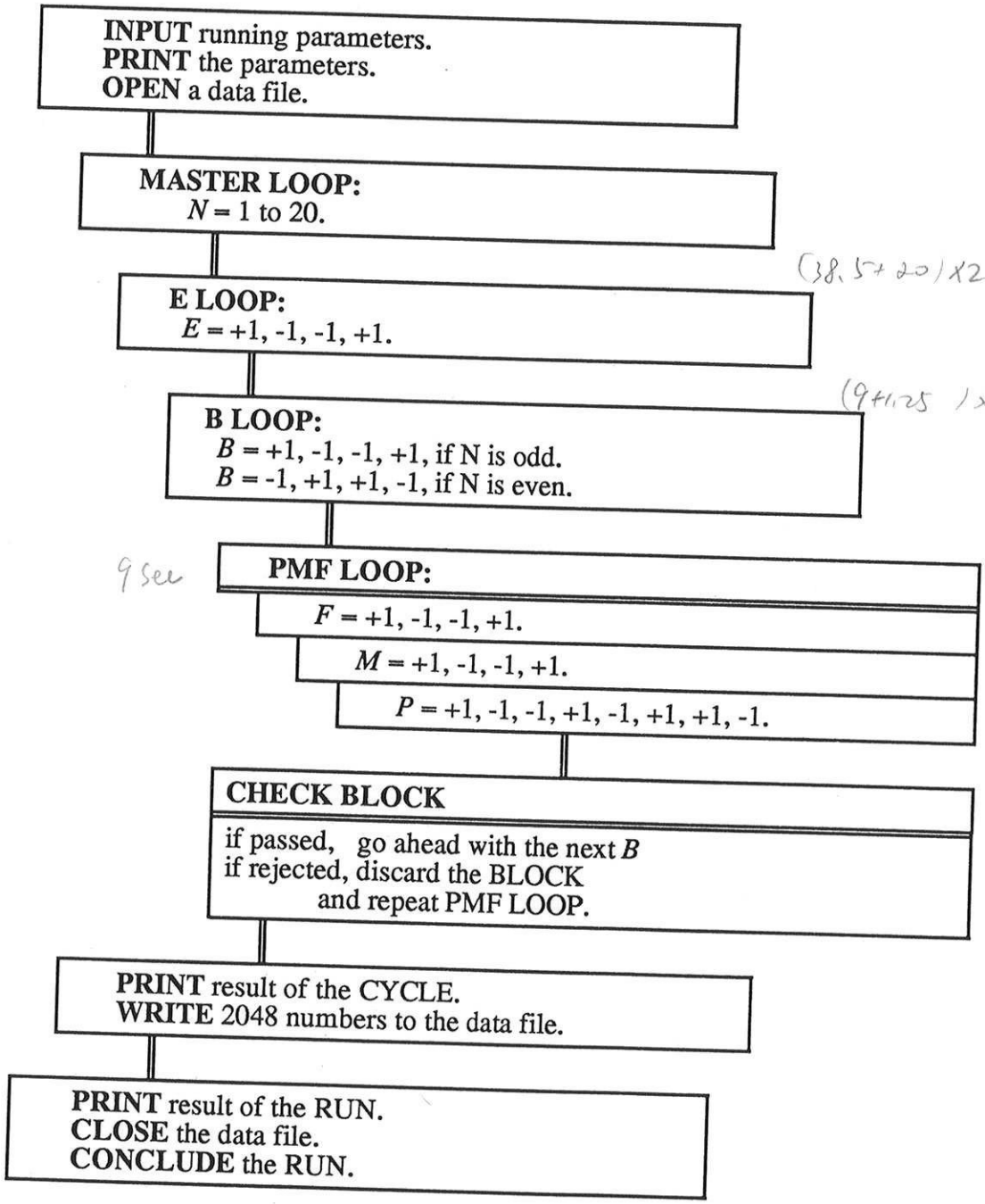

Figure 3.2 Flow diagram of data-taking program

another one negated. This is a better way of making a sequence of changes [PLA70] because it is capable of rejecting a drift in a background up to the (n-1)th order. As an example, a switching pattern of mode 4 can distinguish between a linear drift in beam intensity and a signal that is changing in phase with the switching. Similarly mode 8 switching can suppress the quadratic drift in background. Another advantage is that there are simply less reversals resulting in less wasted time, which becomes significant for B and E reversals. This can be understood by noting that there are only two reversals in one pattern of mode 4, which begins with + and ends with +, while there are four reversals to complete the pattern (+,-,+,-), which begins with + and ends with -.

Each number written into a BLOCK was the result of 50 msec of data accumulation - one DATA interval - and the period chosen was a compromise between a duty factor and noise rejection. Earlier analysis of the noise spectrum dictated a data-taking frequency of at least 7 Hz to avoid the low frequency part of the 1/f noise. Although later improvements in the apparatus made it safe to run at a somewhat lower frequency we used the 50 msec DATA interval for all of the runs we report here. It took 9 seconds to complete a BLOCK. At the end of each PMF.LOOP the numbers were grouped into two of 64 numbers according to their M parameters and each sub-BLOCK was checked for an excessive drift in a beam intensity. If any number within a group deviated from the group mean by more than a preset limit, the whole BLOCK was rejected. This limit was set to 1 or 2% of the integrated beam intensity during one DATA interval, which corresponded to more than 20 standard deviations when we assumed the Poisson statistics for the beam. One or two rejections out of ten were typical, mainly from vacuum bursts. This rejection procedure was an improvement over our old way of comparing one number at a time to the mean of the 80 preceding numbers, in that it examined a unit of sub-BLOCK taken under fixed E, B, and M conditions and there was no chance of one measurement affecting the rejection of another. In our previous continuous check, a drift of the intensity could force the testing routine to favor smaller (or larger) signals upon a field reversal and one could imagine that in some way the software might generate an apparent frequency shift mimicking a real EDM.

Four such PMF.LOOPs under the B reversal sequence (+B,-B,-B,+B) made up a B.LOOP, which then was nested in the E.LOOP, (+E,-E,-E,+E); see Figure 3.2. One execution of E.LOOP was a unit of EDM measurement, a CYCLE, but we note that half of a CYCLE was actually a complete measurement of an EDM in a sense that all five parameters, P, F, M, B, E were symmetrically changed. This was called a MEASUREMENT. Twenty CYCLEs made one RUN, but not all of the CYCLEs in a RUN were the same. Odd-numbered CYCLEs had the B.LOOP sequence of (+B,-B,-B,+B) while even-numbered ones had (-B,+B,+B,-B). This extra twist was introduced to further antisymmetrize the program and thereby reduce the systematic effects from transient change in the C electric field (§§ 3.5.3).

A CYCLE has 2048 numbers corresponding to 102.4 seconds of accumulated DATA intervals, and without a rejection it takes 194 seconds to complete one CYCLE. Thus the duty factor is at best 52.8%. In practice, rejections made it approximately 43% and the typical time spent for a RUN was 1 hour and 20 minutes. As a time saving feature, numbers from each CYCLE were held in a buffer until next reversal of E when the long wait time left enough spare time for archiving and printing. The data analysis and other decision making jobs were done by the computer during the DATA intervals when the accumulation of data was fully taken care of by counting circuit on the interface board, freeing the host microprocessor.

3.2.2 Analysis

Since the numbers are taken in a sequence of well defined states of P, F, E, B, and M, we are able to extract quantities that change with any desired combination of the five parameters. Altogether there are 32 ($= 2^5$) different combinations available, and for each of them we can define a CHANNEL and give a physical meaning to it. To be more systematic we define the NMR variables, (P, F)

P=+1 if δ=+π/2, -1 if $-\pi/2$.

F=+1 if frequency offset is +1.25 Hz, -1 if -1.25 Hz.

Similarly, the field variables, (E, B, M) are defined as follows,

E=+1 if $\vec{E}$ is from hall way to window, -1 otherwise

B=+1 if $\vec{B}$ is from hall way to window, -1 otherwise

M=+1 if AJE transitions are on, -1 for DKH.

As an example, when we are interested in the NMR signal strength accumulated over a CYCLE irrespective of either the frequency offset or the field configurations we consider the so called CHANNEL.P,

$$\text{CHANNEL.P} = \sum_{i=1}^{i=2048} P_i \text{N}_i, \tag{3.6}$$

where N_i is the number taken during the i-th DATA interval of the CYCLE, and P_i represents the phase state during the corresponding DATA interval. This definition of the CHANNEL.P for the modulation P can be easily generalized to any combination X of the five modulations. We formally introduce

$$\text{CHANNEL.X} = \sum_{i=1}^{i=2048} X_i \text{N}_i, \tag{3.7}$$

where X_i is the product of the variables making up the combination X, i.e. X_i=P_iF_i, if X=PF. The CHANNELs can be classified into two groups: those depending on the NMR variables (P, F) only, and the ones dependent on the field variables (E, B, M) as well.

The first group in which we have X=1, P, F, PF are the CHANNELs that characterize the beam and signal averaged over the various field configurations. For the simplest case, X=1 or more specifically X_i = 1 for all i, the corresponding CHANNEL measures the accumulated beam for a CYCLE. Actually it is the only P-independent CHANNEL that is

included in the regular on-line analysis. We call it TOTAL.BEAM, and square root of it is a measure of shot noise of the CYCLE. The CHANNEL.P, whose definition is already given as an example in Eq. (3.6), is sensitive to the detuning Δ of the oscillator frequency f_C from the real NMR frequency f_0. Data is taken at $f_\pm = f_C \pm$ F.OFFSET, and from the lineshape given in Eq. (3.1)

$$\text{CHANNEL.P} = -2\pi I_0(\Delta \cdot T)t_D, \tag{3.8}$$

where t_D is the sum of the DATA intervals, 104.8 seconds, for a CYCLE. CHANNEL.P is also called LOCK.IN because it is the signal strength we would have observed on a lock-in amplifier when the SOF oscillator is set to f_C. On the other hand, when X=PF

$$\text{CHANNEL.PF} = -2\pi I_0 \cdot (\text{F.OFFSET} \cdot T)t_D, \tag{3.9}$$

which we call CALIBRATION because it measures the slope of the resonance curve.

Now we turn to those CHANNELs that are sensitive to the field variables (E,B,M), there are two possibilities for a given combination Z of them: one is X=PZ which measures the frequency shift under a given reversal Z and the other is X=PFZ which determines the intensity shift. To illustrate this point suppose that the resonance frequency and its strength change from $f_0 + \delta f/2$ to $f_0 - \delta f/2$ and from $I_0 + \delta I/2$ to $I_0 - \delta I/2$, respectively, upon the Z reversal. Assuming there is no detuning,

$$\text{CHANNEL.PZ} = \quad 2\pi(I_0 + \delta I) \cdot (\delta f/2 \cdot T)t_D \tag{3.10.a}$$

$$\text{CHANNEL.PFZ} = -2\pi(\delta I/2) \cdot (\text{F.OFFSET} \cdot T)t_D. \tag{3.10.b}$$

We see that CHANNEL.PZ and CHANNEL.PFZ are directly proportional to δf and δI, respectively, and neglecting δI compared with I_0, the frequency and intensity shifts have been separated. Calibrating these CHANNELs using the CHANNEL.PF we have

$$\delta f/2 = -\text{F.OFFSET} \cdot \frac{\text{CHANNEL.PZ}}{\text{CHANNEL.PF}}, \tag{3.11.a}$$

new offset = offset + $\frac{\text{LOCK.IN}}{100 * G}$; $G = \frac{100{,}000}{\text{CALIBRATION}}$

which we define as a Z.SHIFT, and

$$\frac{\delta I/2}{I_o} = \frac{\text{CHANNEL.PFZ}}{\text{CHANNEL.PF}} \tag{3.11.b}$$

which we define as an intensity shift factor of type Z, or $\xi(Z)$. We note that

$$\text{Z.SHIFT} \equiv \frac{1}{2}[f_o(Z=+1) - f_o(Z=-1)] \tag{3.12.a}$$

and

$$\xi(Z) \equiv \frac{I_o(Z=+1) - I_o(Z=-1)}{I_o(Z=+1) + I_o(Z=-1)}. \tag{3.12.b}$$

In Table 3.1 we give names to each of the frequency and intensity shifts that were measured in this way. We note from the discussions in §§ 3.1.2 that the EBM.SHIFT is the one that measures the effect of interest from an EDM, and for this reason it is also called the EDM.SHIFT.

If there is a detuning Δ, the apparent frequency shift Z.SHIFT has a term, $-\xi(Z) \cdot \Delta$ in addition to the real frequency shift $\delta f/2$. This extra term appears because the asymmetric displacements of f_+ and f_- from f_o keep the derivative $\partial S/\partial I_o$ from vanishing even when averaged over F modulation. This is not desirable in that we need to get information on frequency and intensity shifts independently from each other, and before each RUN careful scans were made near the resonance to find the correct frequency averaged over the field configurations. A routine was also included in the program to monitor the detuning over a period of the RUN using the channel LOCK.IN (Eq. 3.8). At the end of each MEASUREMENT the routine defined a new center frequency f_C from integrated LOCK.IN signal according to

$$f_C = f_C^o + g \sum \text{LOCK.IN.} \tag{3.13}$$

Here f_C^o was the frequency set at the beginning of the RUN, and g was a suitable gain factor.

Z (reversal)	**Z.SHIFT** (frequency shift)	$\xi(Z)$ (intensity shift)
E	E.SHIFT	ε
B	B.SHIFT	β
M	M.SHIFT	μ
EB	EB.SHIFT	κ
BM	BM.SHIFT	λ
ME	ME.SHIFT	ν
EBM	EBM.SHIFT (=EDM.SHIFT)	ζ

Table 3.1 Names of the frequency and intensity shifts

So far we have considered the three reversals E, B, and M equivalently, but in practice there were significant frequency and intensity shifts associated with an M reversal and we had to make large hardware compensations to reduce them. This problem is discussed later in this chapter and here we note that it was natural, if not necessary, to treat the variable *M* differently from *E* or *B*. Because of this special treatment of the M reversal, the test for noise rejection was done on each sub-BLOCK of fixed *M*, and there were two separate feed back loops to null out the LOCK.INs for each sign of *M*. Similarly each CHANNEL.X was divided into two sub-CHANNELs which are defined by

$$\text{sCHANNEL.X(AJE)} = \sum_{i=1}^{i=2048} \frac{1+M}{2} X_i \mathrm{N}_i \tag{3.14.a}$$

$$\text{sCHANNEL.X(DKH)} = \sum_{i=1}^{i=2048} \frac{1-M}{2} X_i \mathrm{N}_i. \tag{3.14.b}$$

From this analysis we have the frequency and intensity shifts of E, B, and EB type for each of AJE and DKH as well as separate detunings and slopes. As an example,

$$\text{E.SHIFT}'(\text{AJE}) = -\text{F.OFFSET} \cdot \frac{\text{sCHANNEL.PE(AJE)}}{\text{sCHANNEL.PF(AJE)}'} \tag{3.15}$$

where the prime on the E.SHIFT is to denote that it is from a sub-CHANNEL. To get a total SHIFT for a given field reversal we combine those from the sub-CHANNELs in a proper way (Table 3.2). In this scheme we can think of the final SHIFT as an average of two independent measurements on the JE and KH transitions. Specifically, the total EDM.SHIFT is given by

$$\text{EDM.SHIFT} = \frac{1}{2}[\text{EB.SHIFT}'(\text{AJE}) - \text{EB.SHIFT}'(\text{DKH})], \tag{3.16}$$

where the minus sign was added to take into account M=-1 for DKH.

In a CYCLE we take 2048 numbers which contain much more information than the few CHANNELs described above. For the record all the raw numbers were stored in a file and off-line microscopic study of them proved very useful in understanding systematics in the early stage of the experiment.

3.3 Systematics from Inexact Reversals

We measure the NMR frequencies under the all different states of E, B, and M (there are eight possible configurations). If the only frequency shift were due to an EDM, the measurements would fall into two groups of four members each, depending on whether the product *EBM* is positive or negative. In practice however each reversal is imperfect and

	sub-CHANNELs		total-CHANNELs	
	AJE	**DKH**	**(AJE+DKH)/2**	**(AJE-DKH)/2**
frequency shift				
E	E.SHIFT '(AJE)	E.SHIFT'(DKH)	E.SHIFT	ME.SHIFT
B	B.SHIFT'(AJE)	B.SHIFT'(DKH)	B.SHIFT	BM.SHIFT
EB	EB.SHIFT'(AJE)	EB.SHIFT'(DKH)	EB.SHIFT	EBM.SHIFT
intensity shift				
ε	ε'(AJE)	ε'(DKH)	ε	ν
β	β'(AJE)	β'(DKH)	β	λ
κ	κ'(AJE)	κ'(DKH)	κ	ζ

Table 3.2 Relations between the sub- and total-CHANNELs

introduces some kind of change in the NMRs which has a more mundane origin than the T-violating EDM. In this section we describe the various shifts that were produced by the inexact reversals and what we did about them.

3.3.1 Frequency Shift under a Single Reversal

Suppose there is an E.SHIFT because of a small difference in the E field strengths before and after a reversal. Such a shift should be averaged out by the independent reversals of B and M and should not affect our EDM measurement directly. However, this cancellation is only as exact as the reversals of B and M themselves, and the fraction of the E.SHIFT

which appears as an EDM.SHIFT grows with the inexactitude in those reversals. As a rough estimate we may expect the combined contributions of these shifts to the measurement of an EDM to be

$$\text{"EDM.SHIFT"} \sim \Delta F_0 \cdot \frac{\text{E.SHIFT}}{\Delta F_0} \cdot \frac{\text{B.SHIFT}}{\Delta F_0} \cdot \frac{\text{M.SHIFT}}{\Delta F_0} \qquad (3.17)$$

where ΔF_0 is the linewidth of the resonance. We note that the expression is symmetric with respect to the three SHIFTs, as it must be since a similar argument can be made for the B and M SHIFTs. In order to understand their combined systematic contributions to the measured EDM we consider first the individual E, B, and M shifts.

The change, δE_C in the C region electric field strength can have either external or internal origins. As an example of an external source we can think of the C high voltage relay's failing to reverse the output potentials accurately, while for an internal one there can be a non reversing part of electric field that is generated by static charges built on the inner surface of the Pyrex tube. We can differentiate between them by swapping connections from the relay to the plates (manual reversal of type E): now the discrepancy in the potentials introduced by the relay, or by any other external devices for that matter, would affect the C field in the opposite sense from the normal connection and the E.SHIFT would change its sign. On the other hand, the static field always adds and subtracts in the same sense and its contribution remains independent of the connections. In spite of frequent breakdowns of the C high voltage relay, when it worked it performed well and we have not observed any systematic change in the E.SHIFT that was correlated with the manual reversal. Out of 28 RUNs we report here 13 were with normal connections (NC) and 15 with reversed connections (RC), with the results

$$\text{E.SHIFT(NC)} = -4.91 \pm 0.46 \text{ mHz} \qquad (3.18.a)$$

$$\text{E.SHIFT(RC)} = -5.56 \pm 0.43 \text{ mHz.} \qquad (3.18.b)$$

On the average E.SHIFT = -5.25± 0.31 mHz. This frequency shift corresponded to a field change δE_C of 0.13 V/cm according to the slope of the Stark shift at 29.5kV/cm (Eq. 2.48). It might have been due to some remaining effects from the static charges on the Pyrex tube that used to produce 120 mHz of E.SHIFT before they were shielded by the five cylinders around the C plates (§§ 2.7.2). Alternatively, it could have been from some type of contact potential between the plates.

In a B or an M reversal, what we reverse is the molecular field B_o at the site of the Tl nucleus due to the angular momenta in the molecule. There is supposed to be no externally applied magnetic field present in the C region. Any non reversing ambient field, which would be analogous to the static field in the case of the E reversal, would add to and subtract from the internal field and cause a frequency shift. The ambient field in the laboratory is reduced by a magnetic shield (§§ 2.7.4) to 0.5 mgauss. This remaining field caused about 1.2 Hz of resonance frequency shift which was then nulled out by a current I_A through the compensating coil around the C region. Such a non reversing field affects both the reversals of B and M, but there is another type of unwanted magnetic field that induces a shift only under an M reversal.

The state selectors have 27 gauss of magnetic field in their transition regions and the fringe fields of those magnets averaged over the C region makes a residual field of 2.1 mgauss along the quantization axis. This leakage field does not generate a B.SHIFT, at least to the extent that it reverses exactly, because it is reversed in synchronism with the internal field. It was not until we studied the M reversal carefully that we realized how big it was. Part of the reason we used a magnetic field of 27 gauss instead of the original 52 gauss in the state selectors was to reduce this effect, which still pushed the JE and KH transitions apart by 5 Hz. This M.SHIFT was the largest frequency shift among three reversals, and future TlF experiments should employ redesigned state selectors equipped with proper magnetic shield

to keep the C region clean from the residual fields. For our measurements we added another current I_{SS} to the compensating coil, that changed its directions under a B reversal to bring the two transitions JE and KH on top of each other.

Table 3.3 summarizes how the magnetic fields with the different origins combined under a given configuration of B and M. Here b_A and b_{SS} are respectively the components of ambient and stray state selector field along the quantization axis defined by the electric field. Given a total field strength B_t the corresponding NMR frequency is $2\mu_{Tl} \cdot B_t$. We note that the frequency shifts due to b_A are in the opposite directions for the AJE (M=+1) and the DKH (M=-1), and therefore the extra reversal of M allows us to average the total B.SHIFT to zero. In the measurements, however, with I_A carefully adjusted between RUNs to follow the fluctuations of the ambient field, we observed

$$\text{B.SHIFT}'(\text{AJE}) = -11.66 \pm 0.39\text{mHz} \qquad (3.19.a)$$

$$\text{B.SHIFT}'(\text{DKH}) = \quad -6.19 \pm 0.38\text{mHz}, \qquad (3.19.b)$$

averaging to -8.77±0.25 mHz. This non-zero average of the total B.SHIFT was disturbing. We think that it was a manifestation of either the asymmetry of the M reversal or the presence of an M-independent background shift synchronous with the B reversal. From the table we also see that the total M.SHIFT is proportional to b_{SS}. The measured M.SHIFT was -0.06 ± 0.25 mHz, but this did not mean that the fringe fields were so effectively nulled out by the reversing current I_{SS}. Part of the job was done by the software which changed the frequencies from the SOF oscillator in phase with the M reversal so that LOCK.IN'(AJE) and LOCK.IN'(DKH) were separately zero. (Of course, this adjustment was made only after each MEASUREMENT in order not to null out the EDM shift that we were trying to measure.) The proper measure of the residual b_{SS} after the hardware correction is the difference between the two center frequencies f_C (AJE) and f_C (DKH) at the end of each RUN, and on average it was less than 40 mHz.

	AJE (M=+1)		DKH(M=-1)	
	B=+1	B=-1	B=+1	B=-1
internal field	B_0	$-B_0$	$-B_0$	B_0
ambient field	b_A	b_A	b_A	b_A
state selector field	b_{SS}	$-b_{SS}$	b_{SS}	$-b_{SS}$
total field strength	$B_0+b_A+b_{SS}$	$B_0-b_A+b_{SS}$	$B_0-b_A-b_{SS}$	$B_0+b_A-b_{SS}$
B.SHIFT'	$2\mu_{Tl}\, b_A$		$-2\mu_{Tl}\, b_A$	
M.SHIFT	$2\mu_{Tl}\, b_{SS}$			

Table 3.3 Residual fields and B and M shifts

3.3.2 Intensity Shift under a Single Reversal

If the strength of the NMR signal changes when a reversal is made, we call the change an intensity shift. There is no direct mechanism whereby an intensity shift under a single reversal can affect the measured EDM.SHIFT, but it can combine with other imperfections in the measurement to have an influence on the EDM channel (§§ 3.3.3). The intensity shifts are also good measure of the inexactitude of each reversal and they were closely monitored:

$$\varepsilon\,(\text{AJE}) = -0.62 \pm 0.03\% \qquad \varepsilon\,(\text{DKH}) = 0.58 \pm 0.03\% \qquad (3.20.a)$$

$$\beta\,(\text{AJE}) = -0.27 \pm 0.03\% \qquad \beta\,(\text{DKH}) = -0.16 \pm 0.03\%. \qquad (3.20.b)$$

For the E or B reversals, an inexact reversal of the electric or magnetic field in a state selector can change the resonance frequency and push the RF fields out of resonance. In this case its efficiency in driving the transition can be different before and after the reversal. In fact this type of shift is expected to have only a second order effect on ε or β because at resonance, where the lineshape is flat, the transition probability is not sensitive to the frequency of the RF fields. For the case of the E reversal, however, the frequency of the state selector transitions is so sensitive to the magnitude of the electric field that a non reversing field of 0.1 V/cm can lead to an intensity shift ε of a half a percent. Another possible source for ε is an inexact reversal of the quadrupole potentials. However, for the quadrupoles at U_0=9 kV, observations showed that

$$\frac{1}{\mathrm{FOC}}\frac{d\mathrm{FOC}}{dU_0} = 3.5\times 10^{-4}\,\mathrm{Volt}^{-1}, \tag{3.21}$$

which was too small to account for the observed intensity shift.

So far we have considered the changes in the efficiency of either a state selector or a quadrupole due to a non reversing part of the fields there. Another way for the non reversing fields to affect the signal strengths is to depolarize the molecules i.e. to induce some unwanted transitions and interfere with the state selection or the polarization detection asymmetrically with respect to a reversal. This type of systematic effect, if present in our apparatus, was very small (§§ 2.6.6), but could have contributed to intensity shifts at the level of a few parts in a thousand.

The intensity shift factors ε and β associated with the E and B reversals were certainly not zero, but they were far smaller than the natural size of μ (produced by M reversal). The strengths of the optimized AJ and DK transitions, to which those of the JE and KH transitions respectively are directly proportional, differed by as much as 20% (μ = 10%) and the RF power for the AJ transition had to be substantially decreased to have them about the same. With this compensation we obtained μ=0.51±0.03% over the 28 RUNs. After the care-

ful study of the DK transition (§§ 2.6.7), we concluded that the most likely reason for the big difference was a loss of the focussed molecules in the D state through some unwanted transitions between the quadrupoles and state selectors.

3.3.3 Coupling of Frequency and Intensity Shifts

Suppose that there is a frequency shift when E reverses but that the shift is independent of the sign of B. In that case we would ideally expect EB.SHIFT=0. However, this is not so if there is an intensity shift β. For example, suppose that when B is reversed the intensity of the NMR signal vanishes completely i.e. $\beta = 1$, then in such a measurement it appears that EB.SHIFT = E.SHIFT. This situation is an extreme example of the coupling between the frequency and intensity shifts of two reversals. In general we find that the false EB.SHIFT due to this kind of coupling, which we call ΔEB, is

$$\Delta EB = \beta \cdot (E.SHIFT) + \varepsilon \cdot (B.SHIFT). \tag{3.22}$$

In deriving the expression, terms of the higher order in the shifts - frequency or intensity - were neglected and zero detuning was assumed.

Since the two M states correspond to two virtually independent experiments, each with its own frequency servo loop based on its own LOCK.IN signal, we consider the false EB.SHIFTs for each of the M states separately. From the expression of Eq. (3.16) for the total EDM.SHIFT, the false EDM.SHIFT, which we call ΔEDM, is

$$\Delta EDM = \frac{1}{2}[\Delta EB'(AJE) - \Delta EB'(DKH)]. \tag{3.23}$$

Experimentally we found

$$\Delta EB'(AJE) = \quad 0.09 \pm 0.01 \text{ mHz} \tag{3.24.a}$$

$$\Delta EB'(DKH) = -0.04 \pm 0.01 \text{ mHz}, \tag{3.24.b}$$

and ΔEDM was 0.05 mHz which was actually subtracted from the total EDM.SHIFT to find the desired final result. This was the only correction we had to make to the EDM.SHIFT and it did not change the conclusion of our measurement. We define the corrected shift

$$\text{C.EDM.SHIFT} \equiv \text{EDM.SHIFT} - \Delta\text{EDM}. \tag{3.25}$$

If, contrary to the assumption above, there were a non-zero detuning Δ it could couple with the intensity shift of type EB, which was called κ in Table 3.1, to produce another false contribution to the EDM.SHIFT,

$$\frac{1}{2}[\kappa'(\text{AJE})\,\text{LOCK.IN}'(\text{AJE}) - \kappa'(\text{DKH})\,\text{LOCK.IN}'(\text{DKH})]. \tag{3.26}$$

In fact κ′ for each M was more than an order of magnitude smaller than ε′ or β′, and the detunings measured by LOCK.IN channels were only of order 1 mHz, so this extra error was negligible.

3.3.4 Frequency Shift under Combined Reversals

When we considered the frequency and the intensity shifts under the reversal of a single kind of field, we were interested in changes in that field e.g. for the E reversal we studied the effects of δE_C on the E.SHIFT. If, on the other hand, the reversal of the electric fields changes the magnetic field in the C region or vice versa, it is a far more serious problem in the EDM measurements because it can produce an EDM like shift which is more difficult to distinguish from the real one.

Suppose there is a small magnetic field δB/2 that is flipping in phase with E, then the induced EDM.SHIFT will be $\mu_{Tl}\delta B$, equally contributing to both AJE and DKH schemes. We must therefore set a limit of less than 0.1 μgauss on δB if we are to keep such a systematic effect below the experimental sensitivity of 0.1 mHz. Like δE_C for the E.SHIFT, δB can come from either an external or an internal source. Externally, if the relays that reverse the

electric fields are actuated by electromagnets, the magnetic fields generated by them have a definite relationship with the electric fields they control. Internally, if there is a leakage current from one of the C plates to the other or to the surroundings, it can also produce E-dependent magnetic fields. The analogy with δE_C can be carried out further: the relay-related false EDM.SHIFT changes its sign when the electrical connections are manually reversed, whereas the direction of the leakage current depends only on the polarities of the plates and the resulting false EDM.SHIFT is not affected by the connections. Before we built our own high voltage relay for the C plates we used a pair of 100 kV DPST relays which draw about half an ampere to close. They were working in a complementary manner, i.e. they were turned on one at a time (Figure 2.8), to minimize the change in the magnetic fields upon an E reversal. Still we observed an EDM.SHIFT of 2.4 mHz which changed sign in correlation with the manual reversals and disappeared when we moved the high voltage rack farther away from the beam machine. Our homemade high voltage relay used an AC motor which was turned on only during the switching time. All the other relays were either small or of an AC type, and we found that there were no significant changes in the EDM.SHIFT associated with the manual reversals.

$$\text{C.EDM.SHIFT(EN)} = -0.08 \pm 0.38\text{mHz} \qquad (3.27.a)$$

$$\text{C.EDM.SHIFT(ER)} = 0.29 \pm 0.32\text{mHz}. \qquad (3.27.b)$$

In the present scheme of our experiment there is no test that will allow us to tell the difference between the leakage current effect and the real EDM, and efforts were made to eliminate the possible leakage paths. One mechanism for such a current was local breakdown from the C plates to nearby dielectric surfaces, mainly the inner surface of the Pyrex tube, which we observed in the dark as fuzzy blue images on the tube. The breakdown was thought to be due to microscopic sharp points on the field plates. By bringing a permanent magnet close we could move the images around confirming that they were a type of current. The aluminum cylinders that we installed to shield the C region from the static charges successfully prevented those breakdowns as well. As a more direct indicator of the leak we measured the current flowing into or out of each of the two high voltage feedthroughs, and found it to

be smaller than 2.0 nA when the plates were held at positive and negative 30 kV. In the worst imaginable case the current travels the full length of the C region along the edges of the plates and even then, 2.0 nA could not induce an EDM.SHIFT larger than 1 μHz.

There were other possibilities for the E switching devices to generate E-dependent current, and one of them was in the circuit to control the state selector electric fields. The fields were all derived from a single 600-V supply and its output was divided through chains of resistors to produce the voltages required for the transition and buffer regions. Currents of a few mA flowed in the chains and if the voltage is first reversed by the relay and then divided - which was our original design and the simpler one to build -, these currents change direction under the E reversal. Like the high field leakage current, the effect of the divider chain currents on an EDM.SHIFT would not be changed by the manual reversals. One of the last modifications made was to alter the sequence to a more sensible one of voltage dividers followed by the relays. Although we have not gone back to the original circuit to make a comparison, we expected that the effect was not large because the currents were passing through short lengths of wire that were physically far from the beam machine. There were similar currents on the high voltage monitor chains, which had to be at the output ends of the relays to do their role, but these currents were only a few μA and their effects were estimated to be negligible.

Generalizing the idea that the E reversal can have an effect on the B field, we may consider the complementary situation where the B reversal changes the E field in the C region. If a part of the electric field $\delta E/2$ is reversing in synchronism with B, then there will be an EB.SHIFT′ in proportion to δE for each of the AJE and DKH. However, in this case the EB.SHIFT′ does not change sign under an M reversal and therefore the EDM.SHIFT is not sensitive to the anomalous part of the electric field. In other words, the M reversal averages out these systematics, a clear example of the advantage of having the extra reversal. The observed EB.SHIFT′ for each transition,

$$EB.SHIFT'(AJE) = -4.12 \pm 0.35 \text{ mHz} \quad (3.28.a)$$

$$EB.SHIFT'(DKH) = -4.20 \pm 0.34 \text{ mHz}, \quad (3.28.b)$$

which averaged to -4.16 ±0.24 mHz, could be interpreted as an evidence for such a changing electric field. Unlike the E-dependent δB, it is hard to find a mechanism that can be responsible for a B-dependent δE. We can imagine that reversal of the currents in the state selector magnets might be accompanyed by a slight change in the distribution of the electrostatic potential there, but its effect in the C region is far too small to have any significance. Some other possible explanations for the observed EB.SHIFT′ of each transition are to be found in the following sections.

3.4 Other Systematics

3.4.1 Two-Coil Millman Effect

In the separated oscillating fields method the phase relationship between the two fields determines the detailed structure of the lineshape, and an unaccounted phase difference can directly lead to a shift in the observed resonance frequencies. The Millman effect, originally discovered in the context of a single coil nuclear magnetic resonance experiment [MIL39], can introduce such an extra phase difference in the SOF method under a B or M reversal. Suppose that the axis of the first RF coil is parallel to the beam line, but that the second coil makes an angle θ to the beam line due to a slight misalignment. When we decompose the oscillating field generated by the second coil into two counter rotating ones, because of the misalignment the clockwise field precedes that of the first coil by θ while the counterclockwise one lags by θ. If either B or M is reversed, i.e. if we make a time reversal transformation on the molecular states, the nuclear spin is resonant with alternately clockwise or counterclockwise rotating field and picks up the geometric phase shifts in the opposite sense. This changes the transition probabilities of the NMR (Eq. 2.50) according to

$$P_{CW}(\delta) = \cos^2 \frac{1}{2}\{(\omega_o - \omega)T - \delta - \theta\} \tag{3.29.a}$$

$$P_{CCW}(\delta) = \cos^2 \frac{1}{2}\{(\omega_o - \omega)T - \delta + \theta\}, \tag{3.29.b}$$

where δ is the intended shift of $\pm\pi/2$.

The change in the phase appears as a frequency shift of $\delta f_M = \theta/(2\pi T)$, so that the observed B.SHIFT′ for each transition was actually due to a combination of the non reversing ambient field and the Millman effect,

$$\text{B.SHIFT}'(\text{AJE}) = 2\mu_{\Pi} \cdot b_A + \frac{\theta}{2\pi T}. \tag{3.30}$$

We note that by varying T, the time of flight between the two coils, we can differentiate the two different origins of the shift. We made use of the strong dependence of the velocity of the focussed molecules on the quadrupole voltages to obtain a plot of the B.SHIFT versus the linewidth of the SOF resonance, which is inversely related to T (Figure 3.3). This showed that θ was approximately 6×10^{-3} radian, corresponding to a two-coil Millman shift of about 140 mHz. While not a small shift in itself, it was still dominated by the shift from non reversing field by a factor of ten.

During the preliminary runs we found that there was a more direct disturbance of the phase relationship between the two oscillating fields caused by the phase modulating electronics itself. The problem occurred in the monostable multivibrator (one shot) at the output stage of the phase shifter, which introduced a delay for the fine adjustments of the phase difference between the two 120-kHz square wave outputs. It happened to share a 5 V power supply with the transistors that amplified the TTL signals for the E and B reversals. The states of the transistors seemed to affect the delay time of the one shot and hence the output phase relation, and we observed a few mHz of frequency shift from this instrumental effect.

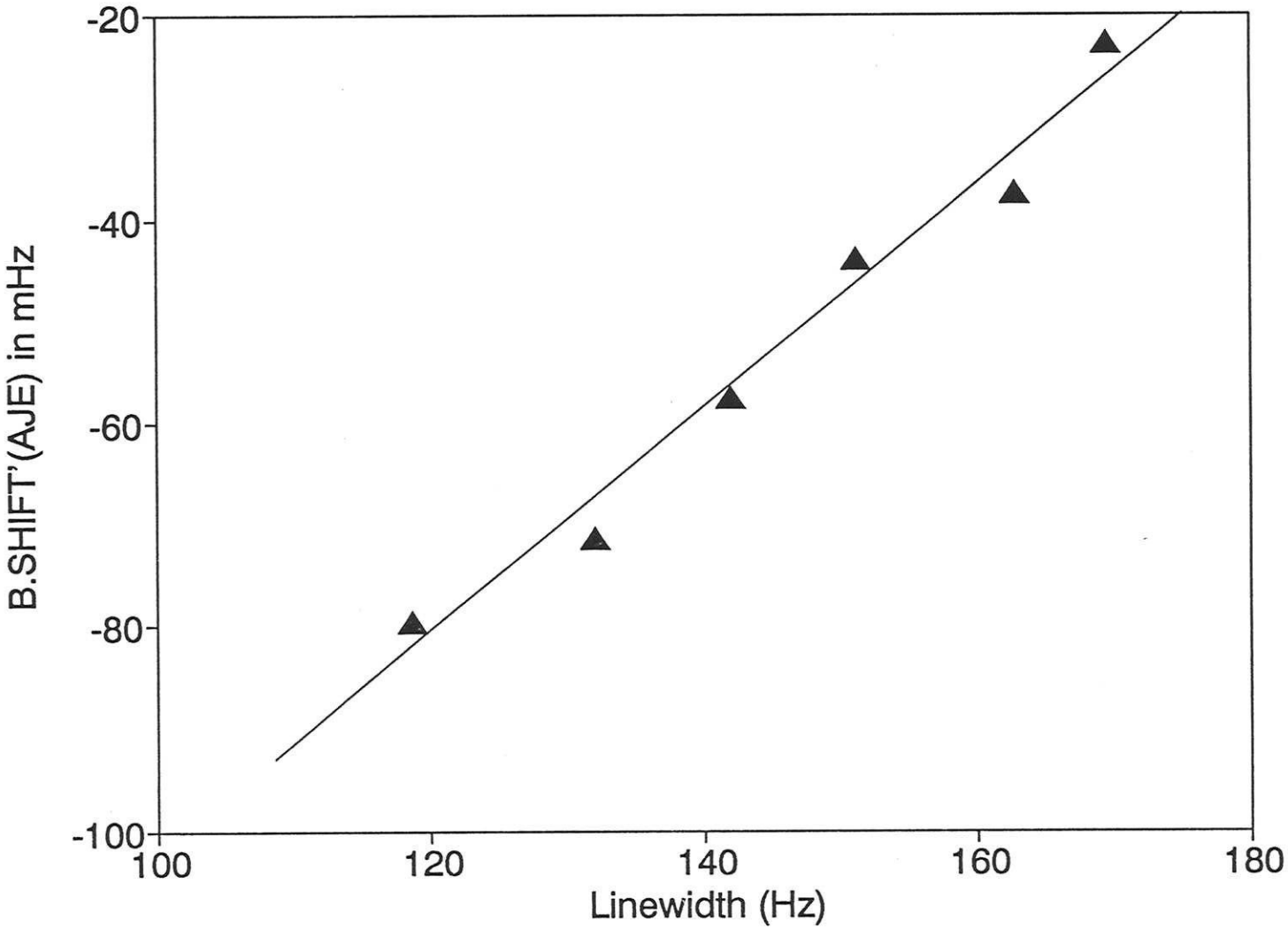

Fig. 3.3 B.SHIFT' vs. linewidth (Millman effect)

It took an extra delay of only a few tenths of a nano second to explain the observed frequency shift while a typical response time of the logic units was specified to be 10 nano seconds. We built a whole new set of switching electronics with better design and the problem was gone.

3.4.2 Motional Effects

In the early beam resonance experiments on neutrons and Cs atoms one of the most troublesome systematic effects was from motional magnetic field, $\vec{b}_M = (1/c)\vec{v} \times \vec{E}$, that changed its directions on reversal of the electric field $\vec{E}$. In combination with applied magnetic field $\vec{B}$ this motional field produced a modulation of the Zeeman shift that was synchronous with the E reversal. If the B and E fields were perfectly parallel, this effect would produce no shift, because in that case $\vec{b}_M$ would be perpendicular to the applied B field causing no change in total magnetic field strength under the E reversal. In practice, however, there was always finite misalignment in the two fields, and when they make an angle θ in the plane transverse to the beam velocity, $\vec{b}_M$ changes the total magnetic field strength by $b_M \sin\theta$. It was difficult in those experiments to tell the difference between a real EDM and this spurious effect.

One of the advantages of our working on the polar molecule TlF in this regard is that we are virtually free from such an alignment problem because there is no externally applied magnetic field in the C region. The electric field is the only symmetry axis of the system and that determines the alignment of the internal field $\vec{B}_O$. Consequently the misalignment angle θ is zero and there is no first order effect of the motional magnetic field $\vec{b}_M$. Now the Zeeman shift from the motional field appears only as a second-order effect, which is on the order of $(b_M/B_O)^2$. When there is an ambient magnetic field along $\vec{v} \times \vec{E}$, however, it can tilt the effective magnetic field at the site of the Tl nucleus and can have the same effect as the misalignment. In our apparatus there was a residual field corresponding to 1.2 Hz of B.SHIFT along $\vec{E}$, and given the cylindrical symmetry of the shield, it is reasonable to assume a comparable field along the direction of $\vec{v} \times \vec{E}$. In that case the misalignment factor $\sin\theta$ was

$$\sin\theta = \frac{\text{B.SHIFT}}{f_o} \cong 10^{-5}. \tag{3.31}$$

It can be compared with the estimated θ of 10^{-2} in the Cs beam experiment [CAR68]. The motional field itself for the TlF beam passing through the electric field of 30 kV/cm at 280 m/sec is 93 μgauss which leads to an EDM.SHIFT of less than 3 μHz for the value of θ above.

In addition to the motional magnetic fields due to the normal flight of the molecules along the beam axis, we may consider effects from a lateral movement of the beam under a field reversal. In general such a movement can not give rise to a significant frequency shift because the parallel-plate design of the C electrodes produces a very uniform field between the plates. For an order-of-magnitude estimate we considered an easier case of parallel round disks and found that 1 mm of transverse displacement could lead to a frequency shift of less than 0.02 mHz. Although we can imagine some mechanisms that might force the beam profile to move - e.g. E-dependent imperfections in the quadrupole field distribution or B-dependent magnetic field nonuniformity in the state selectors - any such movements are not expected to be large enough to have an observable effect.

3.4.3 Transient Effects

As was discussed in the subsection on data taking (§§ 3.2.1) after a modulation or a reversal, the computer waited for a while until the machine reached a steady state under the new condition. The waiting times were supposed to be long enough that the transient behavior of the signal would not affect the measurements. On the other hand, to make the best use of the running time we could not be too generous. In order to find a good compromise we studied the transient signals carefully. Also the sequence of the reversals was carefully anti-symmetrized in order to average out any residual transients. The transient signals could be most directly studied by monitoring the output from the detector as a modulation was made. For more detailed information we referred to the numbers archived from a RUN to compare

the signals taken under the same states of the machine but with different times having passed since a reversal. These analyses allowed us to unravel the following problem with the E reversal.

In a CYCLE, E fields were changed in the sequence of (+E,-E,-E,+E), and we were able to determine the frequency shift of type E from either first or the second half of the CYCLE. While the two independent measurements should be equivalent, the results turned out to be different by as much as 200 mHz. The discrepancy was generated by the transient signal which, in the first half, is associated with the -E state, and in the second half with the +E state. In an E reversal we waited 12.5 seconds after the high voltage supplies were turned back on (first they had to be turned off to make a reversal). After the turn-on, the time constant for charging the C plates was short enough to bring the potential very close to the final value at the end of the wait time if we assume simple exponential law. A closer look at the measured numbers, however, showed that for the final few volts the time constant was rather long, about 20 seconds. As a consequence, when the new numbers began to be read in after the E reversal, the C high voltage was still about 2 volts less than its final voltage.

This tail part of the transient signal has a potential danger in it. In the first half of a CYCLE during the -E configuration, the B.LOOP of (+B,-B,-B,+B) picks up a quadratic part of the drift in the C voltage as a B.SHIFT which has no cancelling counterpart since there is no transient during the previous +E state. This produces a non-zero EB.SHIFT for the first half. Fortunately the transient behaviors seemed to be the same whether the reversal was from +E to -E or the other way around, and therefore the first and the second halves contributed with opposite shifts producing no net EB.SHIFT for a CYCLE as a whole. Nevertheless we preferred not to rely on the symmetry of the transients and so we introduced another twist in the data taking program to ensure that the effect would be cancelled: every second CYCLE, the B.LOOP was done in an inverted sequence (-B,+B,+B,-B) to produce an EB.SHIFT of the opposite sign.

3.4.4 Background Signals

With the machine working as intended it was generally successful in achieving clean and efficient state selection (§§ 2.6.7). But there were still some small NMR signals to be found near the JE and KH resonances with the state selector RF power turned off (RF.OFF). They were considered to be from the higher, most likely J=2, rotational states. Although the RF.OFF background was usually kept much smaller than the regular signals with the state selectors on (RF.ON), they could nevertheless affect the measurements in one way or another. A considerable amount of time was invested in understanding and minimizing their effects.

One of the ways that the RF.OFF background can affect the measurements is that its intensity shift is detected as a frequency shift of the corresponding type. This effect is most pronounced when the RF.OFF peaks near the running point, and it can lead to the apparent frequency shift of

$$\Delta f = r \cdot \xi \cdot \frac{\Delta F_0}{2\pi}, \tag{3.32}$$

where r is the ratio of the RF.OFF to RF.ON signal strengths, ξ is the intensity shift factor of the RF.OFF peak, and ΔF_0 is the linewidth of the RF.ON signal. When r is on the order of 1.0% and ΔF_0=130 Hz, a few mHz of a shift is not surprising. Even when the RF.OFF itself does not have a significant intensity shift, it can push the running point away from the true zero crossing of the RF.ON line and introduce a detuing Δ. In that case the intensity shift of the RF.ON part would couple with such a detuning to produce a frequency shift. In this generalized picture the intensity shift factor ξ should be replaced with $\xi(\text{RF.OFF}) + \xi(\text{RF.ON})$. Secondly, if we consider the frequency shift of the RF.OFF background, it is less likely to affect the experiment because its contribution is simply reduced by the factor r. Finally it is possible that the velocity of the molecules participating in the

RF.OFF resonance might change under some reversal. In that case if the RF.OFF near the running point is many "Ramsey wiggles" away from its own resonance frequency, the effect of the change will be amplified and the local movement of the background can be significant.

To deal with these RF.OFF background effects we first tried to make a correction by taking measurements with the state selectors turned on and off, and subtracting the off signal from the on signal to find the RF.OFF-corrected results. This helped us to understand the effects from the RF.OFF background but it was not an ideal way to run the experiment because half the time was spent learning about the background. We decided to deal with the background signals head on, and we studied them in more detail.

Above E_c of 20 kV/cm we observed three RF.OFF resonances near 120 kHz. Two were close to the JE and KH NMR lines and approximately 1 kHz apart while the third was small and further away. Their lineshapes were different from the RF.ON lines with a characteristically small width of 80 or 90 Hz and rather flat envelops without pronounced peaks. We have varied many parameters of the machine to make this background as small as possible. It was very persistent and did not respond to most of the changes, but it showed a strong dependence on the quadrupole high voltages and also on the RF power of the separated oscillating magnetic fields. Qualitatively, as the quadrupole voltages were increased the RF.OFF resonances grew in the same way as the RF.ON did, but the former peaked at a much higher voltage than the latter, suggesting strongly that the RF.OFF background involved the higher rotational states. We took the advantage of this and made our runs at lower focussing voltages where the RF.OFF background was significantly reduced at the expense of the RF.ON signal (§§ 2.5.5). We also found a preference of the RF.OFF background for the weaker oscillating magnetic fields - consistent with its smaller linewidth. When the quadrupole voltage and the SOF power were optimized we were able to make the RF.OFF background smaller than 1.0% of the RF.ON signal.

Observations on the background showed that it was approximately the same whether both of the state selectors were turned off or only one of them (either A or B) was off, and for the latter case the signals did not depend on which transition the other state selector was tuned to, AJ or DK. It was inferred from the observation that the states involved in the RF.OFF background were not related to those of the AJE or DKH schemes. In an attempt to make an identification of the RF.OFF background we generalized the observation and scanned the RF field frequency at one of the state selector with the other off. If the state selector were tuned to a transition that populated the states for the RF.OFF resonances, the background would change - either increasing or decreasing. None of the transitions between the focussed and the unfocussed states of the J=1 manifold affected the background, but we did discover one such transition at a frequency corresponding to a pair of states in the J=2 manifold. For this reason we think the RF.OFF background is produced by Majorana transitions among the J=2 population of the beam.

Finally we studied the Zeeman and Stark shifts of the RF.OFF resonances and as was expected they had the same Zeeman shifts as the RF.ON signal confirming that they were thallium nuclear spin flips. The Stark shifts, however, were in the opposite sense and only half as large as that of the RF.ON. We made use of the opposite movements of the resonances to separate the RF.OFF from the RF.ON as much as possible. A field of strength 30 kV/cm was found to place the RF.ON resonance approximately mid-way between the two RF.OFF resonances, which further reduced the size of the RF.OFF background near the operating frequency of the experiment. This was the main reason why we ran at such a high field in spite of the many practical difficulties it caused. The use of high field also increased the sensitivity of the experiment to the T-violating effects through stronger polarization of the molecules, but it was the background signals that really forced us to add the extra 10 kV/cm to the originally planned field of 20 kV/cm.

Before the background signals were put under this tight control, they were relatively large and contributed to the various shifts monitored in a RUN leading to especially confusing results for the B.SHIFT′ and EB.SHIFT′. Because they were independent of the state

selector RF field, the shifts of the RF.OFF background accumulated the same counts in each of the sub-CHANNEL AJE and DKH. When these sub-CHANNELs were interpreted as frequency shifts with physical meanings, they were weighted with the opposite M variables. Consequently the resulting B.SHIFT′(AJE) and B.SHIFT′(DKH) showed anomalous discrepancy, and similar problem was found in the channel of EB.SHIFT as well. With the RF.OFF background greatly reduced and pushed away from the RF.ON line, these anomalous shifts were also minimized. We note, however, that in the final data we report here, there is still the same type of inconsistency in the B.SHIFT′ (Eq. 3.19) and EB.SHIFT′ (Eq. 3.28) and we suspect that the residual background effects are responsible.

3.5 Results

28 RUNs were made over a period of a week at the end of July 1989. The running conditions of the beam machine were as described in Table 2.4 and the total running time was about 38 hours, out of which 16 hours were the net data taking time. The results from the 28 RUNs are presented - in the same format as Table 3.2 - in Table 3.4 where the frequency shifts are in mHz and the intensity shifts are in %. More detailed results are summarized in Table 3.5 where the manual connection (§§ 3.1.3) for each RUN is also specified. In the table N stands for a normal connection, while R for a reversed connection. Normal and reversed are defined in accordance with the definition of the field variables given at the beginning of §§ 3.2.2. For the manual reversal of type Q a connection is defined to be normal if the horizontal rods are charged to the same polarity as the window-side C plate. In Table 3.5 C.EDM.SHIFTs of the 28 RUNs are shown. E.SHIFTs and BM.SHIFTs, which are proportional to non-reversing ambient E and B fields respectively, are also given as a measure of inexactitude of the reversals in each RUN. Finally, in Figure 3.4 the C.EDM.SHIFTs are plotted with the corresponding error bars.

After a small correction to the EDM.SHIFT (§§ 3.3.3), we quote as a final result

$$\text{C.EDM.SHIFT} = (0.14 \pm 0.24)\ \text{mHz} \tag{3.33}$$

which we interpret as a null shift. We also note that the systematic correction was 0.05 ± 0.01 mHz. The correction had no qualitative effect on our conclusion. The quoted error can be compared with the ideal statistical noise of 0.19 mHz over the 16-hour data taking period (§ 2.9). The final result is based on the assumption that the 28 measurements of the shift belong to Gaussian distributions having a common central value. To check the goodness of such an assumption we calculate chi-squared of the sample

$$\chi^2 = \sum_i \frac{(\text{C.EDM.SHIFT}(i) - \langle\text{C.EDM.SHIFT}\rangle)^2}{\sigma_i^2}, \tag{3.34}$$

where σ_i is the uncertainty (one standard deviation) of the measurement from the i-th RUN. The result obtained is $\chi^2 = 36$ for 27 degrees of freedom, which is larger than one would expect to find 89% of the time from a purely statistical sample. This could indicate that the error bars assigned to the individual RUNs are too small or that the central value varies from RUN to RUN in a systematic way. The error bar of a RUN (σ_i) is obtained from the observed variance of 20 shifts measured in the RUN without any rejections, and therefore there is no reason to inflate the error bars. We have also looked closely at the 28 RUNs to see if there was a systematic fluctuation of any monitored shifts that was correlated with the measured EDM.SHIFT. Such a systematic fluctuation would have supported the idea of a non-statistical distribution of the sample. We did not find any evidence of such an effect. However, when the C.EDM.SHIFTs are grouped according to the B manual connections we found

$$\text{C.EDM.SHIFT(BN)} = -0.26 \pm 0.32 \text{ mHz} \tag{3.35.a}$$

$$\text{C.EDM.SHIFT(BR)} = 0.65 \pm 0.37 \text{ mHz}. \tag{3.35.b}$$

Each of these numbers is approximately one standard deviation away from the total mean, and this discrepancy suggests that there could be a small difference between the central values of the two distributions, BN and BR. If such a systematic effect were present, it would

explain the marginally excessive value of the chi-squared. However, we expect that the contribution of the spurious effect to the final C.EDM.SHIFT should cancel when we average over the 28 RUNs - that is precisely why we had the manual reversals.

For these reasons, instead of increasing the final error bar by 15% to bring the chi-squared into comfortable 27, we opted to quote the number in Eq. (3.33) as it stands.

	sub-CHANNELs		total-CHANNELs	
	AJE	**DKH**	**(AJE+DKH)/2**	**(AJE-DKH)/2**
E	-5.12 ± 0.40	-4.94 ± 0.41	-5.25 ± 0.31	0.13 ± 0.25
B	-11.66 ± 0.39	-6.19 ± 0.38	-8.77 ± 0.30	-2.65 ± 0.25
EB	-4.12 ± 0.35	-4.20 ± 0.34	-4.19 ± 0.25	0.19 ± 0.24
ε	-0.62 ± 0.03	0.58 ± 0.03	0.00 ± 0.02	-0.60 ± 0.02
β	-0.27 ± 0.03	-0.16 ± 0.03	-0.22 ± 0.02	-0.05 ± 0.02
κ	0.01 ± 0.03	0.02 ± 0.03	0.02 ± 0.02	-0.01 ± 0.02

Table 3.4 Results of the July 1989 RUNs

RUN #	Manual connection				E.SHIFT (mHz)	BM.SHIFT (mHz)	C.EDM.SHIFT (mHz)
	E	B	M	Q			
1	N	N	N	N	-3.77 ± 1.81	-3.77 ± 1.52	-2.08 ± 1.69
2	R	N	N	R	-6.20 ± 3.26	-19.61 ± 1.35	-3.82 ± 1.66
3	N	N	N	R	-3.66 ± 1.47	11.69 ± 1.40	1.46 ± 1.69
4	N	R	N	N	-10.75 ± 2.72	-11.20 ± 1.45	1.37 ± 1.21
5	R	R	N	R	-1.52 ± 1.40	6.18 ± 1.62	-0.19 ± 0.94
6	R	R	R	R	-6.02 ± 1.55	-8.17 ± 1.18	-1.27 ± 1.26
7	R	R	R	N	-4.66 ± 1.42	-21.57 ± 1.24	1.48 ± 1.45
8	R	R	N	N	-2.78 ± 1.29	-13.55 ± 1.44	0.01 ± 1.33
9	R	N	N	N	-7.06 ± 1.21	2.39 ± 1.33	-0.48 ± 1.21
10	R	N	R	N	0.96 ± 3.75	5.52 ± 1.48	0.56 ± 1.06
11	R	N	R	R	-3.11 ± 3.10	13.68 ± 1.20	-1.90 ± 1.14
12	R	N	N	R	-3.58 ± 2.22	22.32 ± 1.67	0.73 ± 1.45
13	N	N	N	R	-2.57 ± 1.41	-6.81 ± 1.34	-0.71 ± 1.56
14	N	N	R	R	5.76 ± 5.90	-5.43 ± 1.38	0.76 ± 1.14

Table 3.5 Details of the July 1989 RUNs

Table 3.5 continued

RUN #	Manual connection				E.SHIFT (mHz)	BM.SHIFT (mHz)	C.EDM.SHIFT (mHz)
	E	B	M	Q			
15	N	N	R	N	-7.75 ± 1.99	-0.57 ± 1.38	-0.08 ± 1.39
16	N	N	N	N	-9.52 ± 1.26	0.61 ± 0.93	-0.18 ± 1.14
17	R	N	R	R	-5.31 ± 1.93	-18.01 ± 1.84	-0.97 ± 1.35
18	R	N	R	N	-6.20 ± 1.51	-19.65 ± 1.69	2.52 ± 0.99
19	N	N	R	N	-0.80 ± 1.44	-5.62 ± 1.64	-1.93 ± 1.12
20	N	N	R	R	-2.89 ± 1.63	-7.98 ± 0.92	-0.91 ± 1.56
21	R	R	R	N	-6.10 ± 1.60	7.83 ± 1.53	2.25 ± 1.13
22	R	R	R	R	-6.22 ± 4.45	12.37 ± 1.75	3.60 ± 1.64
23	N	R	R	N	-1.83 ± 1.47	-1.00 ± 1.54	0.20 ± 1.38
24	N	R	R	R	-2.92 ± 1.81	-17.52 ± 1.51	1.81 ± 1.54
25	N	R	R	R	-7.41 ± 2.90	3.86 ± 1.51	-1.20 ± 1.70
26	N	R	R	N	-9.81 ± 1.40	2.76 ± 1.35	0.26 ± 1.81
27	R	R	N	N	-9.66 ± 1.38	1.39 ± 1.21	0.41 ± 1.52
28	R	R	N	R	-11.12 ± 1.99	2.67 ± 1.42	0.41 ± 1.60

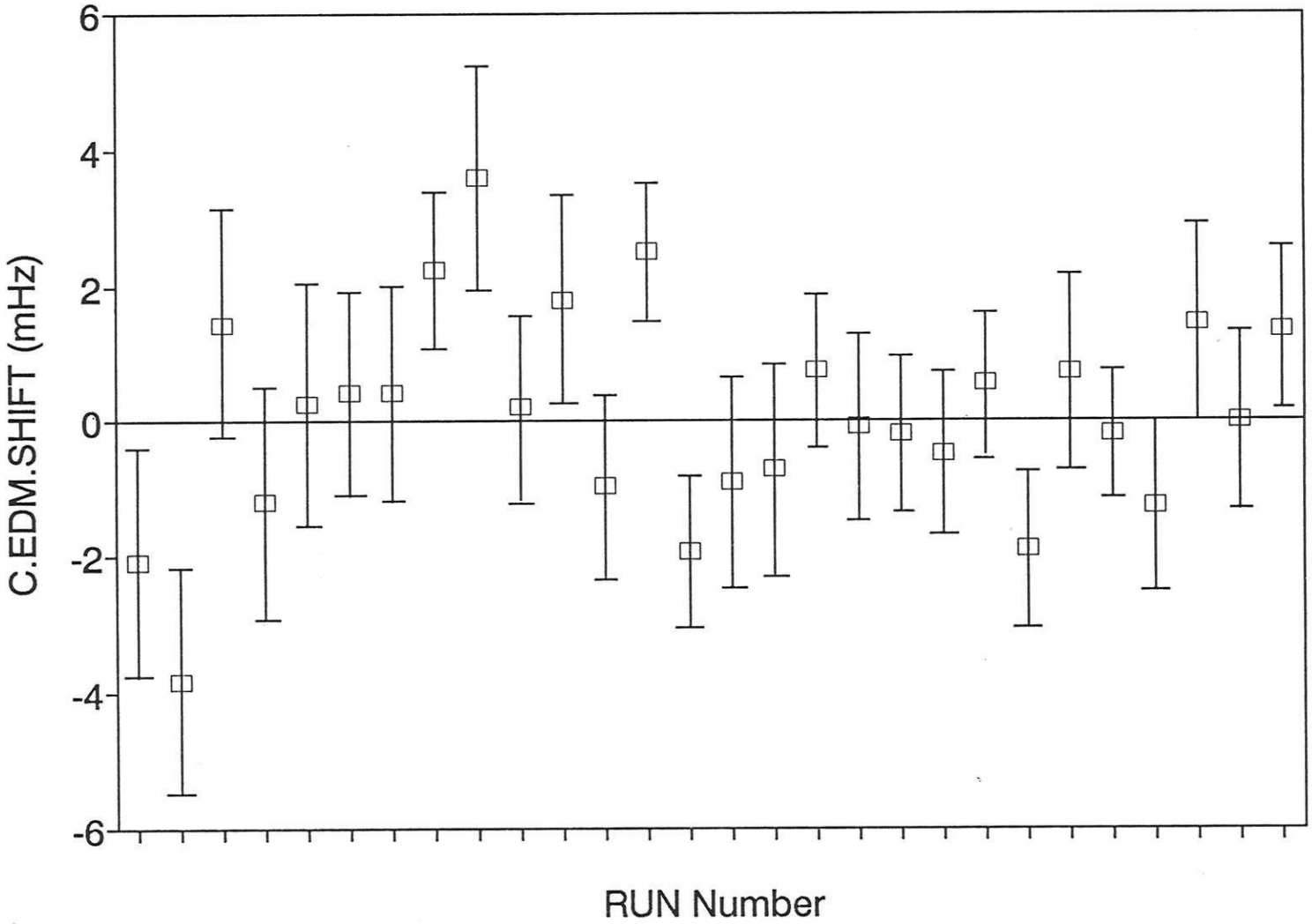

Fig. 3.4 C.EDM.SHIFTs of 28 RUNs

CHAPTER 4

INTERPRETATION

Though the original motivation for the TlF experiment was to measure the proton EDM [SAN67], it is obviously not the only possibility for T-violation in the complicated structure of the molecule. A molecular EDM proportional to the Tl nuclear spin can arise from an EDM of the Tl nucleus as a whole or as a result of an EDM of the electron or from P- and T-odd interactions between the electrons and nucleons. In this chapter our result will be interpreted in terms of these various hypothetical T-violating mechanisms in TlF.

4.1 P- and T-violating Coupling Constant

The measured frequency shift, C.EDM.SHIFT = (0.14 ± 0.24)mHz, is related to the coupling constant d of the P- and T-violating effective Hamiltonian, $H_{PT} = -dh\ \vec{\sigma} \cdot \hat{\lambda}$ (Eq. 1.33), by the relation

$$\text{C.EDM.SHIFT} = -2d\ |<\vec{\sigma} \cdot \hat{\lambda}>|. \tag{4.1}$$

In order to estimate d, we need to know the projection of $\hat{\lambda}$ onto the quantization axis of the nuclear spin $\vec{\sigma}$ while the molecule is under the electric field E_C = 29.5 kV/cm. Because of the large electric polarizability and the strong spin-rotation coupling of the TlF molecule, the electric field direction (z axis) becomes the quantization axis of $\vec{\sigma}$ (§§ 3.4.2), and

$$<\vec{\sigma}\cdot\hat{\lambda}>=<\cos\theta>. \tag{4.2}$$

Here θ is the angle between the z axis and $\hat{\lambda}$. Now for a given hyperfine state, e.g. J or E, $<\cos\theta>$ can be calculated from the corresponding wavefunction of total Hamiltonian in the C region. In practice the Stark interaction dominates in determining the orientation of the molecule and the hyperfine structure can be ignored. Since $W = h\mathrm{B}\vec{\mathrm{J}}^2 - \mu_E E_C \cos\theta$ (Eq. 2.19),

$$<\cos\theta>=\frac{h\mathrm{B}<\vec{\mathrm{J}}^2>-<W>}{\mu_E E_C}. \tag{4.3}$$

Applying the method of continued fractions [KUS59] to the states $|J=1, M_J=\pm1\rangle$ in a field of $E_C = 29.5$ kV/cm (J is the nominal quantum number for the rotational angular momentum) we found $<\cos\theta>=0.542$. Hence

$$d = (-0.13 \pm 0.22)\text{mHz}. \tag{4.4}$$

In Fig. 4.1 $<\cos\theta>$ is plotted as a function of the field E_C. We note that the higher field makes the projection larger and the experiment becomes more sensitive to the parameter d for a given resolution in the NMR frequency.

The expression for $<\cos\theta>$ in Eq. (4.3), though formally appealing, requires one to know the eigenfunction as well as the eigenenergy of the Hamiltonian W, and is not the most convenient one to use. To find an alternative we note that

$$\frac{dW}{dE_C}=\frac{\partial W}{\partial E_C}+\frac{\partial W}{\partial\theta}\frac{d\theta}{dE_C}. \tag{4.5}$$

From a classical Hamiltonian, on the other hand,

$$W=\frac{I}{2}\dot{\theta}^2+\frac{J_Z^2}{2I\cdot\sin^2\theta}-\mu_E E_C\cos\theta, \tag{4.6}$$

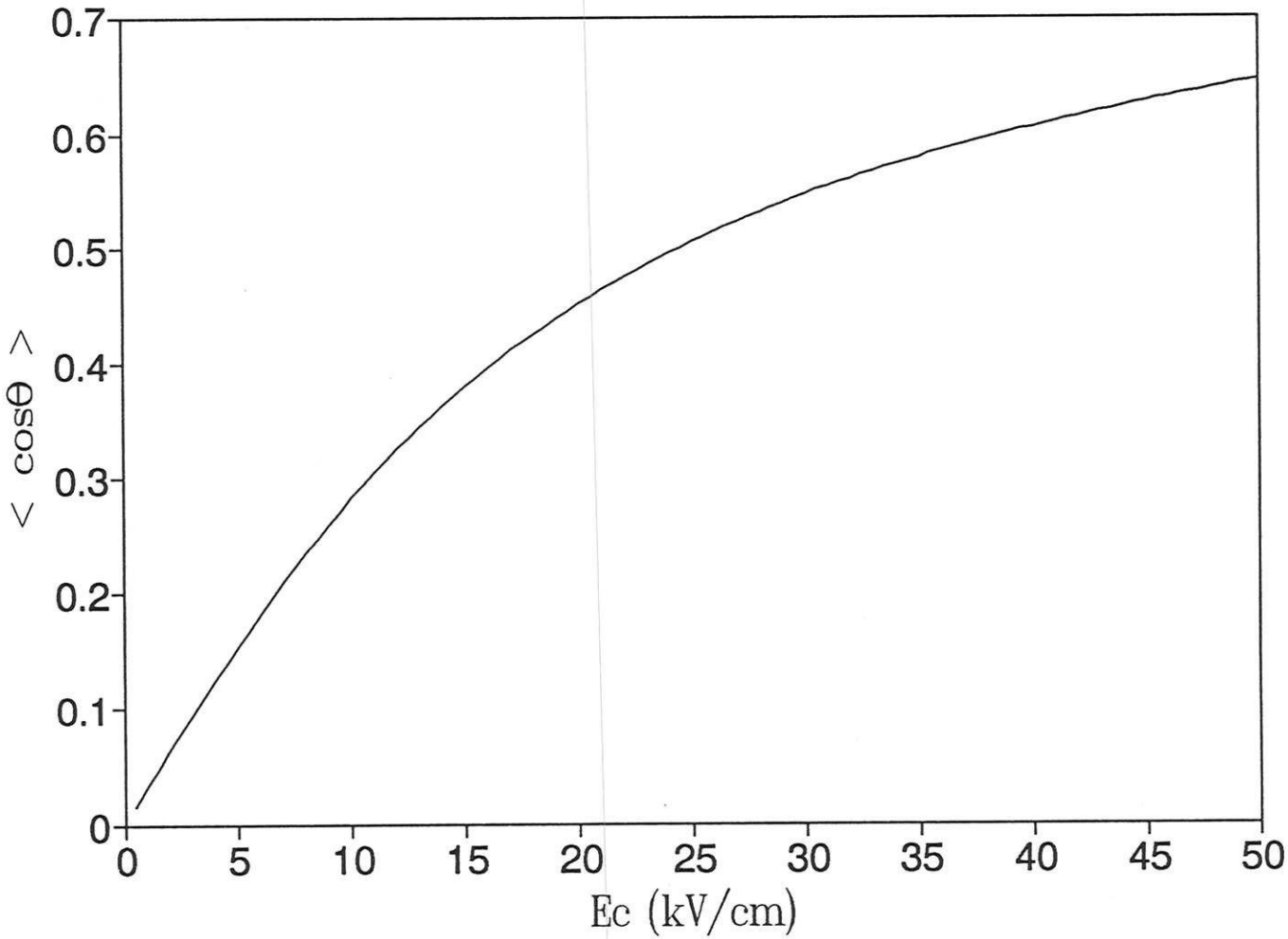

Fig. 4.1 <cos Θ > vs. Ec for TlF in J=1 Mj=±1 state

$<\vec{\sigma}\cdot\hat{\lambda}>$ for an eigenstate of the total Hamiltonian, $H_{HF}+H_{STA}$. The result generally depends on the particular state we consider. For the state H the eigenstate of H_{HF} is $|M_J=1, M_1=1/2, M_2=1/2\rangle$, where 1 and 2 refer to the Tl and F nucleus respectively. In this case $<\vec{\sigma}\cdot\hat{\lambda}>$ does reduce to $<\cos\theta>$ and we may use the expression in Eq. (4.7). When the electric field is small $<W>$ for J=1 and $M_J=\pm1$ is approximately given by

$$<W>\cong 2hB-\frac{1}{20}\frac{(\mu_E E_C)^2}{hB}-dh<\vec{\sigma}\cdot\hat{\lambda}>. \tag{4.11}$$

It follows that $<\cos\theta>$ is $\mu_E E_C/10hB$. Hence the molecular EDM d_{TlF} is related to the measured number d by

$$d_{TlF}=d\frac{\mu_E}{10B}, \tag{4.12.a}$$

given our value for d

$$d_{TlF}=(-1.7\pm2.9)\times10^{-23}e\ \text{cm}. \tag{4.12.b}$$

We note that the above expression for d_{TlF} is specific to the molecule in state H, but by rotational invariance it applies also to any state in the J=1 manifold with the total angular momentum F=2. For the F=1 multiplet which includes states J and K we find that the measured parameter d can be interpreted as an EDM larger than Eq. (4.12.b) by a factor of 3.4.

4.3 Proton EDM

It is of interest to interpret our result in Eq. (4.4) in terms of the proton EDM because that is what the experiment was originally devised to measure [SAN67], and the result puts by far the best limit on it. If a proton carries an EDM d_p along its spin, the electric dipole interaction of the Tl nucleus in the nuclear shell model is

$$H_{PT}(d_p)=-d_p\sum_n\vec{\sigma}_n\cdot\vec{E}(\vec{r}_n), \tag{4.13}$$

where $\vec{E}(r_n)$ is E field at the location $\vec{r}_n$ of the n-th proton, referred to the center of mass of the nucleus $\vec{r}_{Tl}$. We note that the summation is only over the protons because Tl has an even number of neutrons with their spins paired off. Now requiring the nucleus to be in electrostatic equilibrium we put

$$\sum_n e\,\vec{E}(\vec{r}_n) = 0. \tag{4.14}$$

The electric field $\vec{E}(\vec{r}_n)$ can be represented by the potential $V(\vec{r}_n)$, such that $\vec{E}(\vec{r}_n) = -\vec{\nabla} V(\vec{r}_n)$. To proceed, we make a Taylor expansion of the potential near the center of mass of the nucleus [HIN80a]. Under the equilibrium condition the expansion leads to

$$\vec{\nabla} V(0) = -\frac{1}{6Z}\sum_n r_n^2\,\vec{\nabla}[\nabla^2 V(0)], \tag{4.15}$$

where the spherical symmetry of the nucleus was used to eliminate the linear and cross product terms in $\vec{r}_n$. Making a similar expansion of the interaction Hamiltonian, Eq. (4.13), under the constraint of the above equation,

$$H_{PT}(d_p) = -d_p\left[\frac{1}{Z}\sum_n r_n^2 \sum_{n'} \vec{\sigma}_{n'} - \sum_n r_n^2 \vec{\sigma}_n\right] \cdot \left[\frac{1}{6}\vec{\nabla}\nabla^2 V(0)\right]. \tag{4.16}$$

We note that H_{PT} naturally breaks into nuclear and electronic parts,

$$H_{PT}(d_p) = -d_p \vec{D} \cdot \vec{X}. \tag{4.17}$$

Since the Tl nucleus has one unpaired 3s proton in the shell model, the nuclear part $\vec{D}$ can be written as

$$\vec{D} = (\langle r^2 \rangle_{total} - \langle r^2 \rangle_{3s})\vec{\sigma}_{Tl}. \tag{4.18}$$

From the Gauss's law the electronic part $\vec{X}$ can be rewritten in terms of a gradient of the electronic charge density ρ at the nucleus,

$$\vec{X} = \frac{2\pi}{3} e \vec{\nabla}\rho(0), \tag{4.19}$$

which, when time averaged, is parallel to the internuclear vector $\hat{\lambda}$ because of the cylindrical symmetry of the molecule. Finally,

$$H_{PT}(d_p) = -d_p D X \vec{\sigma}_{Tl} \cdot \hat{\lambda} \tag{4.20}$$

which is in the same form as the effective Hamiltonian $H_{PT} = -dh\vec{\sigma}_{Tl} \cdot \hat{\lambda}$ in Eq. (1.33). Most recently Coveney and Sandars [COV83] made estimates of D and X. Using their values of D= 2.9 fm^2 and X=2711 in atomic units together with our measurement of d, we obtain for the proton EDM:

$$d_p = (-3.7 \pm 6.3) \times 10^{-23} e\,\text{cm}. \tag{4.21}$$

From the nuclear factor D in Eq. (4.18) it is clear that the experiment would not have been sensitive to the proton EDM if the nucleus were a point particle. The fact that we could circumvent Schiff's theorem [SCH63] because of the finite size of the Tl nucleus is an example of the volume effect discussed in §§ 1.4.1. In that case it is the nuclear forces that allow us to measure the proton EDM. Now we discuss how the presence of magnetic forces on the Tl nucleus can also help reveal the proton EDM [HIN80a]. Considering the nucleus as a point particle this time, the presence of an internal magnetic field $\vec{B}_o(\vec{r}_{Tl})$ modifies the equilibrium condition of Eq. (4.14) into

$$Z\vec{E}(\vec{r}_{Tl}) + \mu_{Tl}\vec{\nabla}(\vec{\sigma}_{Tl} \cdot \vec{B}_o(\vec{r}_{Tl})) = 0. \tag{4.22}$$

where μ_{Tl} is the magnetic dipole moment of the nucleus. This modification leads to an extra electric dipole interaction of

$$H'_{PT}(d_p) = d_p \vec{\sigma}_{Tl} \cdot \left[\frac{\mu_{Tl}}{Z} \vec{\nabla}(\vec{\sigma}_{Tl} \cdot \vec{B}_o(\vec{r}_{Tl})) \right]. \tag{4.23}$$

Besides disturbing the electrostatic balance, the magnetic field can couple directly with the EDM via the nuclear motion with respect to the center of mass of the molecule. It is an electric analogue of the more familiar spin-orbit coupling of an electron, and

$$H''_{PT}(d_P) = -d_P \vec{\sigma}_{Tl} \cdot \left[\frac{1}{2Mc} (\vec{p} \times \vec{B}_o - \vec{B}_o \times \vec{p}) \right], \tag{4.24}$$

where M and $\vec{p}$ are mass and momentum of the Tl nucleus, respectively.

Formally, both interactions can be derived by introducing a new type of Lorentz- and gauge-invariant electromagnetic coupling into the Dirac equation for the nucleus,

$$(i\hbar c\gamma^\mu \partial_\mu - Mc^2)\psi = \frac{i}{2} d_P \gamma^5 \sigma_{\mu\nu} F^{\mu\nu} \psi, \tag{4.25}$$

where the standard notation and metric are used. This P- and T-odd coupling on the right-hand side of the equation, which is a pseudotensor-tensor interaction of Dirac and electromagnetic fields, was first considered by Salpeter [SAL58] to study effect of an electron EDM on a hydrogen atom. When expanded it leads to the Hamiltonian,

$$H_{PT}^{M}(d_P) = -d_P \beta (\vec{\sigma} \cdot \vec{E} + i\vec{\alpha} \cdot \vec{B}_o), \tag{4.26}$$

whose two terms reduce to the interactions in Eq. (4.23) and Eq. (4.24) in the limit of heavy - and slow - nucleus. Evaluating the combined effect of the interactions [HIN80a,COV83], we can place another limit on the proton EDM

$$d_P = (-1.1 \pm 1.9) \times 10^{-22} e\,\text{cm}, \tag{4.27}$$

which is roughly three times larger than the one in Eq. (4.21). The theoretical difficulties in estimating this magnetic effect are less than the case of the volume effect because no nuclear structure consideration is required here. In that sense the limit in Eq. (4.27) is an independent - if somewhat conservative - estimate of d_P that compliments the calculation of the volume effect.

4.4 Nuclear EDM

Even if the proton and neutron possess no permanent EDM, a nucleus may do so as a result of its structure. In the following model of nuclear EDM we regard a nucleus as a charge distribution of a finite size from the beginning and we consider its electrostatic interaction with the potential $V(\vec{r})$ produced by the electrons,

$$W_{\mathrm{Tl}} = \sum_n e\, V(\vec{r}_n), \tag{4.28}$$

where $\vec{r}_n$ is the location of the n-th proton as in Eq. (4.13). When it is expanded in a Taylor series, the linear and cubic terms in $\vec{r}_n$ are the P- and T-odd interactions of interest and once again by invoking the equilibrium condition of Eq. (4.15) they can be written as [COV83]

$$H_{\mathrm{PT}}(d_{\mathrm{Tl}}) = e\left[\frac{3}{5}\sum_n r_n^2 \vec{r}_n - \frac{1}{Z}\sum_n r_n^2 \sum_{n'} \vec{r}_{n'}\right] \cdot \left[\frac{1}{6}\vec{\nabla}\nabla^2 V(0)\right], \tag{4.29}$$

where we have neglected the octupole interaction

$$H'_{\mathrm{PT}} = \frac{e}{6}\sum_n \theta_n^{ijk}\partial_i\partial_j\partial_k V(0) \tag{4.30}$$

with $$\theta_n^{ijk} = r_n^i r_n^j r_n^k - \frac{r_n^2}{5}[\delta_{ij} r_n^k + \delta_{jk} r_n^i + \delta_{ki} r_n^j],$$

because the Tl nucleus has spin 1/2. We note that $H_{\mathrm{PT}}(d_{\mathrm{Tl}})$ is also decomposed into the nuclear and electronic parts like $H_{\mathrm{PT}}(d_{\mathrm{P}})$ in Eq. (4.16). Once again the electronic part is proportional to $\vec{\nabla}\rho(0)$ and the Hamiltonian $H_{\mathrm{PT}}(d_{\mathrm{Tl}})$ can be rewritten as

$$H_{\mathrm{PT}}(d_{\mathrm{Tl}}) = -4\pi e \vec{\nabla}\rho(0) \cdot \vec{Q}\,(\mathrm{Tl}), \tag{4.31}$$

where $\vec{Q}$, which is called the Schiff moment, is defined as

$$\vec{Q}(\mathrm{Tl}) = \frac{e}{6}\left[\frac{3}{5}\sum_n r_n^2 \vec{r}_n - \frac{1}{Z}\sum_n r_n^2 \sum_{n'} \vec{r}_{n'}\right]. \tag{4.32}$$

The expectation value of $\vec{Q}$(Tl) must lie along the only symmetry axis of the nuclear system, namely $\vec{\sigma}_{Tl}$ and the Hamiltonian is again in the form of $dh\ \vec{\sigma} \cdot \hat{\lambda}$. Using the theoretical value for X (Eq. 4.19) and our measurement of d, we obtained the result

$$Q\ (\mathrm{Tl}) = (-1.8 \pm 3.0) \times 10^{-23} e\ \mathrm{cm\ fm^2}. \tag{4.33}$$

In fact, comparing the expressions for $H_{PT}(d_p)$ and $H_{PT}(d_{Tl})$, the proton EDM and the Schiff moment can be related by

$$Q\ (\mathrm{Tl}) = \frac{1}{6} d_p \mathrm{D} \tag{4.34}$$

and our EDM measurement on the Tl nucleus is completely summarized by the quantity Q (Tl), the hypothetical EDM of a proton being one of its interpretations. By the same token, the magnetic effect considered in the previous section could equally well have been interpreted in terms of the EDM of the nucleus as a whole.

The Schiff moment of the Tl nucleus can be related to fundamental P- and T-violating interactions as, for example, Sushkov *et al* [SUS84] have done for the Kobayashi-Maskawa model. In that model the nuclear CP-violation is dominated by virtual kaon exchange. Sushkov *et al* wrote this interaction as a simple shell-model potential for the valence (3s) proton of Tl nucleus,

$$H_{PT}(\mathrm{KM}) = \xi \vec{\sigma}_{3s} \cdot \nabla U_{core}(\vec{r}_{3s}), \tag{4.35}$$

where ξ is the T-violation parameter and U is a nuclear potential - e.g. a Saxon-Woods potential. Later it was pointed out by the same group [FLA86] that the core excitation can also make a comparable contribution to the nuclear EDM. They concluded that Q (Tl) should be 10^{-29}~10^{-30} e cm fm^2. Sadly, this estimate is some 7 orders of magnitude smaller than our measurement, as is the KM prediction for the neutron when compared with the current limits on the neutron EDM. As was noted previously (§§ 1.4.2) estimates of T-odd

nuclear moments based on the KM model are generally very small and it is not surprising that calculations from other CP-violating theories predict much larger Schiff moment for Tl nucleus than the KM model does [KHA88].

4.5 Electron EDM

An electron EDM d_e will give rise to the T-odd Hamiltonian,

$$H_{\mathrm{PT}}(d_e) = -d_e\beta(\vec{\sigma}\cdot\vec{\mathrm{E}} + i\vec{\alpha}\cdot\vec{\mathrm{B}}) \tag{4.36}$$

(see also Eq. 4.26 for the proton case). It can induce a molecular EDM via the second-order perturbation,

$$\vec{d}_{\mathrm{TlF}} = \sum_i \frac{\langle\psi_O|\vec{D}|\psi_i\rangle\langle\psi_i|H_{\mathrm{PT}}(d_e)|\psi_O\rangle}{E_O - E_i} + \mathrm{h.c}, \tag{4.37}$$

where h.c. stands for the hermitian conjugate and $\vec{D}$ is the molecular electric dipole moment operator, $\vec{D} = \mu_{\mathrm{E}}\hat{\lambda}$. We note that the Hamiltonian in its nonrelativistic limit is proportional to the total spin of electrons and for TlF, which has closed electron shells, the second-order contribution might be expected to vanish. However, the electrons in the vicinity of the Tl nucleus are highly relativistic and it turns out that due to relativistic effects there is a substantial molecular EDM induced by d_e.

The origin of this relativistic enhancement can be found in the singularities of the ($j = 1/2$) Dirac wavefunctions in a Coulomb field. This is most apparent when we consider coupling due to the magnetic interaction part of the Hamiltonian, $-id_e\beta(\vec{\alpha}\cdot\vec{\mathrm{B}})$ between the single electron states $|s_{1/2}\rangle$ and $|p_{1/2}\rangle$. Here the magnetic field is produced by the nuclear magnetic dipole moment and is given by

$$\vec{\mathrm{B}} = \mu_{\mathrm{Tl}}\left[-\frac{8\pi}{3}\vec{\sigma}_{\mathrm{Tl}}\delta(\vec{r}) + \frac{3(\vec{\sigma}_{\mathrm{Tl}}\cdot\hat{r})\hat{r} - \vec{\sigma}_{\mathrm{Tl}}}{r^3}\right]. \tag{4.38}$$

The delta function leads to a "contact" interaction,

$$\langle p_{1/2}|\, V|\, s_{1/2}\rangle \propto \psi_{p_{1/2}}(0)\psi_{s_{1/2}}(0), \tag{4.39}$$

which diverges at the origin like $r^{2\xi-2}$ with $\xi = \sqrt{1-(\alpha Z)^2}$. In a more realistic treatment the finite size of the nucleus should be taken into account and this eliminates the divergence, although the $-id_e\beta(\vec{\alpha}\cdot\vec{B})$ coupling still makes a significant contribution to the induced EDM.

The electric part of Eq. (4.36), $-d_e\beta(\vec{\sigma}\cdot\vec{E})$, is directly proportional to the electron spin and induces no second-order EDM of the molecule even in relativistic calculation. The leading contribution from this term appears in the third-order perturbation that includes the hyperfine interactions [FLA85]. Detailed estimate shows that there is a similar relativistic enhancement of this third-order effect and the molecular EDM induced by $-d_e\beta(\vec{\sigma}\cdot\vec{E})$, though higher in order, is in fact larger than that due to $-id_e\beta(\vec{\alpha}\cdot\vec{B})$. Using the calculation of Flambaum and Khriplovich we can place a limit on the electron EDM

$$d_e = (-1.4\pm 2.4)\times 10^{-25}\ e\ \text{cm} \tag{4.40}$$

from our measurement. It is competitive with the best limit (Table 4.2)

$$d_e = (-1.5\pm 5.7)\times 10^{-26}\ e\ \text{cm} \tag{4.41}$$

from the experiment [MUR89] on a Cs atom which has one unpaired valence electron.

4.6 T-odd Weak Couplings

So far we have considered T-violation in the molecule to be confined either to the nucleus or to the electrons. Another obvious possibility is that it may arise from T-odd weak couplings between the electrons and the nucleons. Among the various Lorentz-invariant combinations of bilinear covariants of Dirac spinors it can be shown that the scalar-pseudoscalar and tensor-pseudotensor interactions are odd under P and T (see Table 4.1).

The scalar-pseudoscalar couplings are given as either

	bilinear covariant	P	T
scalar	$\overline{\psi}_a\psi_b$	$\overline{\psi}_a\psi_b$	$\overline{\psi}_b\psi_a$
pseudoscalar	$\overline{\psi}_a\gamma^5\psi_b$	$-\overline{\psi}_a\gamma^5\psi_b$	$-\overline{\psi}_b\gamma^5\psi_a$
vector	$\overline{\psi}_a\gamma^\mu\psi_b$	$\overline{\psi}_a\gamma_\mu\psi_b$	$\overline{\psi}_b\gamma_\mu\psi_a$
axial vector	$\overline{\psi}_a\gamma^5\gamma^\mu\psi_b$	$-\overline{\psi}_a\gamma^5\gamma_\mu\psi_b$	$\overline{\psi}_b\gamma^5\gamma^\mu\psi_a$
tensor	$\overline{\psi}_a\sigma^{\mu\nu}\psi_b$	$-\overline{\psi}_a\sigma_{\mu\nu}\psi_b$	$-\overline{\psi}_b\sigma_{\mu\nu}\psi_a$
pseudotensor	$\overline{\psi}_a\gamma^5\sigma^{\mu\nu}\psi_b$	$\overline{\psi}_a\gamma^5\sigma_{\mu\nu}\psi_b$	$\overline{\psi}_b\gamma^5\sigma_{\mu\nu}\psi_a$

Table 4.1 P and T transformations of bilinear covariants.

$$< H_{PT}^{(1)}(C_S^{(1)}) >= iC_S^{(1)}\frac{G_F}{\sqrt{2}}(\overline{\psi}_n\psi_n)(\overline{\psi}_e\gamma^5\psi_e) \tag{4.42}$$

or

$$< H_{PT}^{(2)}(C_S^{(2)}) >= iC_S^{(2)}\frac{G_F}{\sqrt{2}}(\overline{\psi}_n\gamma^5\psi_n)(\overline{\psi}_e\psi_e), \tag{4.43}$$

where G_F is the Fermi constant and $C_S^{(1,2)}$ represent the strengths of the interactions. We also note that the Hamiltonians are taken in the form of contact interactions because the 4-momeutum change associated with the process is presumably much smaller than the mass of the gauge particle. In the limit of low electron momentum $H_{PT}^{(1)}$ can be approximated as [BOU75],

$$H_{PT}^{(1)}(C_S^{(1)}) = C_S^{(1)} \frac{G_F}{2\sqrt{2}} \gamma^0 \left[i \frac{\vec{\sigma} \cdot \vec{p}}{m_e} \right] A\delta(\vec{r}), \tag{4.44}$$

where A is the mass number (isoscalar symmetry is assumed for simplicity). Note that there is a cancellation of this coupling in systems having closed electron shells, just as in the case of the electron EDM. In order to estimate its effect on the EDM of TlF one has to consider once again the third-order perturbation involving the hyperfine interaction. Using the results of Flambaum and Khriplovich together with our experimental result we find that

$$C_S^{(1)} = (5.4 \pm 9.2) \times 10^{-6}, \tag{4.45}$$

which is approximately the same as the upper bound obtained from the recent Cs experiment [MUR89] - see Table 4.2.

Similarly $H_{PT}^{(2)}$, when expanded to the order in $1/m_p$, is [FLA85]

$$H_{PT}^{(2)}(C_S^{(2)}) = C_S^{(2)} \frac{G_F}{2\sqrt{2}} \gamma^0 \left[i \frac{\vec{\sigma}_{3s} \cdot \vec{p}_{Tl}}{m_p} \right] \delta(\vec{r}). \tag{4.46}$$

Its effect appears as a second-order perturbation, but due to nonrelativistic movement of the nucleons - or simply from its $1/m_p$ dependence - the limit on $C_S^{(2)}$ derived from our experiment is about two orders of magnitude larger than that on $C_S^{(2)}$.

Now for the tensor-pseudotensor interaction there are also two possibilities like Eq. (4.42) and (4.43). However, we consider here only the coupling where γ^5 is acting on the electronic part.

$$H_{PT}(C_T) = iC_T \frac{G_F}{\sqrt{2}} (\bar{\psi}_n \sigma^{\mu\nu} \psi_n)(\bar{\psi}_e \gamma^5 \sigma_{\mu\nu} \psi_e). \tag{4.47}$$

This type of interaction was first considered by Hinds, Loving, and Sandars [HIN76] and from the nonrelativistic expansion of the nucleonic part [MAR85],

$$H_{PT}(C_T) = \sqrt{2} i C_T G_F (\gamma^0 \vec{\gamma})_e \cdot \delta(\vec{r} - \vec{r}_{3s}) \vec{\sigma}_{3s} \tag{4.48}$$

Coveney and Sandars [COV83] estimated its effect on TlF. Using their result and our measurement we obtain

$$C_T = (1.7 \pm 3.0) \times 10^{-7}, \tag{4.49}$$

which is comparable with the limit derived from the experiment on Hg [LAM87].

From this point of view of new weak currents, the nuclear EDM considered in § 4.4 can be interpreted in terms of T-odd nucleon-nucleon interactions. Flambaum *et al* studied such an interaction [FLA86]. From their calculation our measurement of the Schiff moment, Q(Tl), places a limit

$$1.2\eta_{pp} - 1.4\eta_{pn} \cong (-0.01 \pm 0.02), \tag{4.50}$$

where η is a measure of the T-odd weak scalar-pseudoscalar coupling in units of the Fermi constant for proton-proton (pp) or proton-neutron (pn) interactions. As was pointed out by the authors, the calculation involves large uncertainties and the result should be taken as an order-of-magnitude estimate. Still it provides the most stringent limit on such coupling strengths.

4.7 Conclusion

The limits on T-violation parameters derived from our measurement are listed with the corresponding numbers from the Hg and Cs experiments in Table 4.2, where EDM's are in e cm, the Schiff moments in e cm fm^2 and the coupling strengths are dimensionless.

We note that the atomic Hg EDM has been measured with three orders of magnitude higher resolution than our measurement of TlF EDM, yet the latter puts generally more stringent limits on fundamental T-violation parameters. This greater sensitivity of a TlF molecule to P- and T-violating effects can be understood from an expression of d_{TlF}, equivalent to Eq.(4.10),

	TlF [CHO89]	Hg [LAM87]	Cs [MUR89]
atomic or molecular EDM	$(-1.7\pm2.9)\times10^{-23}$	$(0.7\pm1.5)\times10^{-26}$	$(-1.8\pm6.9)\times10^{-24}$
Schiff moment	$(-1.8\pm3.0)\times10^{-23}$	$(-1.8\pm3.8)\times10^{-23}$	n/a
proton EDM	$(-3.7\pm6.3)\times10^{-23}$	n/a	n/a
electron EDM	$(-1.4\pm2.4)\times10^{-25}$	$(-0.5\pm1.1)\times10^{-24}$	$(-1.5\pm5.7)\times10^{-26}$
$C_S^{(1)}$	$(5.4\pm9.2)\times10^{-6}$	$(1.0\pm2.2)\times10^{-5}$	$(2.5\pm9.8)\times10^{-6}$
C_T	$(1.7\pm3.0)\times10^{-7}$	$(-1.2\pm2.5)\times10^{-7}$	n/a

Table 4.2 Limits on T-violation parameters

$$\vec{d}_{TlF} = \sum_i \frac{\langle \Psi_O | \vec{D} | \phi_i \rangle \langle \phi_i | H_{PT} | \Psi_O \rangle}{E_O - E_i} + \text{h.c,} \tag{4.51}$$

where the electric dipole moment operator $\vec{D}$ can be written as $\mu_E\hat{\lambda}$. Because TlF is a polar molecule we have large electric dipole coupling, $\langle\Psi|\,\mu_E\hat{\lambda}|\,\phi_i\rangle$>. The presence of nearby rotational levels with opposite parity and the same total angular momentum makes the molecule much more sensitive than the atom to H_{PT}.

The significance of our measurement can be summarized as follows. Our result provides the best limit on the proton EDM d_p. We also place stringent limits on the P- and T-odd weak coupling strengths between the electrons and nucleons, $C_S^{(1)}$ and C_T. For

nucleon-nucleon T-odd couplings our limit of $\eta \sim 0.02$ is also one of the smallest available. For the electron EDM our limit is the second best, being four times larger than the recent result from Cs atoms.

For the future of the TlF experiment we believe that the beam machine at Yale which has so far achieved improvements by a factor of 50 over the last few years can still make more progress. There is a potential for even larger signal-to-noise ratio if the interference from the higher rotational states is properly removed and the uninteresting focussed states are quenched. Simply by having the machine in a more reliable state one can take data for a longer period of time to obtain better statistics. Some of the remaining systematics should, however, be understood in more detail for real progress in the experiment. In this regard the anomalies associated with the AJE/DKH comparisons need to be studied carefully. First of all, to remove the instrumental artifacts that introduced the frequency shift between JE and KH transitions (M.SHIFT) one may want to install magnetic shields around the state selectors. When all the details are taken care of, another order of magnitude improvement in the measurement of T-violation from TlF could be expected. In the long run, just as the beam resonance experiments on neutrons and atoms finally gave way to the measurements on trapped particles, so it will be necessary to find ways of slowing and trapping TlF molecules without disturbing the coherent evolution of the Tl nuclear spins. With the present beam machine we can observe the Tl spin precession only for 10 msec or so whereas trapped TlF could have an interaction time as long as 10 seconds, leading to an enormous improvement. With recent advances in the techniques of slowing and trapping atoms and ions there is real hope in that direction.

References

[ALT86] Altarev, I.S., *et al.* JETP Lett. **44**, 460 (1986).

[AND66] Anderson, J.B., Andres, R.P., and Fenn, J.B., Adv. chem. Phys. **10**, 275 (1966).

[ANS85] Anselm, A.A., Bunakov, V.E., Gudkov, V.P., and Uraltsev, N.G., Phys. Lett. **152B**, 116 (1985).

[BAR89] Barr, S.M., and Marciano, W.J., *CP Violation* Jarlskog, C., ed. Singapore. World Scientific. (1989).

[BEA83] Beall, G., and Deshpande, N., Phys. Lett. **132B**, 427 (1983).

[BEN78] Bennewitz, H.G., and Buess, G., J. Chem. Phys. **28**, 175 (1978).

[BLA83] Blanke, E., *et al.*, Phys. Rev. Lett. **51**, 355 (1983).

[BOR75] Borkenhagen, U., Malthan, H., and Toennies, J.P., J. Chem. Phys. **63**, 3173 (1975).

[BOU75] Bouchiat, C., Phys. Lett. **57B**, 284 (1975).

[CAS69] Casella, R.C., Phys. Rev. Lett. **22**, 554 (1969).

[CAR68] Carrico, J.P., *et al.*, Phys. Rev. **174**, 125 (1968).

[CHO89] Cho, D., Sangster, K., and Hinds, E.A., Phys. Rev. Lett. **63**, 2559 (1989).

[CHR64] Christenson, J.H., Cronin, J.W., Fitch, V.L., and Turlay, R., Phys. Rev. Lett. **13**, 138 (1964)

[COM83] Commins, E.D., and Bucksbaum, P.H., *Weak Interactions of Leptons and Quarks* New York. Cambridge University Press. (1983).

[COV83] Coveney, P.V., and Sandars, P.G.H, J. Phys. B **16**, 3727 (1983).

[DAY54] Dayton, I.E., Shoemaker, F.C., and Mozley, R.F., Rev. Sci. Instr. **25**, 485 (1954).

[DIJ72] Dijkerman, H., Flegel, W., Gräff, G., and Mönter, B., Z. Natur. Forsch **27**, 100 (1972).

[DRE77] Dress, W.B., *et al.*, Phys. Rev. D **15**, 9 (1977).

[FEN87] Fenn, J.B., private communications.

[FLA85] Flambaum, V.V., and Khriplovich, I.B., JETP **62**, 872 (1985).

[GIM82] Gimlet, J.L., Henrikson, H.E., Boehm, F., and Lerner, J., Phys. Rev. C **25**, 1567 (1982).

[GRE61] Greene, E.F., Rev. Sci. Instr. **32**, 860 (1961).

[HAL84] Halzen, F., and Martin, A.D., *Quarks and Leptons* New York. Wiley. (1984).

[HAL84] Hallin, A.L., *et al.*, Phys. Rev. Lett. **52**, 337 (1984).

[HAR82] Hardekopf, R.A., Keaton, P.W., Lisowski, P.W., and Veeser, L.R., Phys. Rev. C **25**, 1090 (1982).

[HAR69] Harrison, G.E., Sandars, P.G.H., and Wright, S.J., Phys. Rev. Lett. **22**, 1263 (1969).

[HER79] Herzberg, H., *Molecular Spectra and Molecular Structure* Vol.4 New York. Van Nostrand Reinhold. (1979).

[HIN76] Hinds, E.A., Loving, C.E., and Sandars, P.G.H., Phys. Lett. **62B**, 97 (1976).

[HIN80a] Hinds, E.A., and Sandars, P.G.H., Phys. Rev. A **21**, 471 (1980).

[HIN80b] Hinds, E.A., and Sandars, P.G.H., Phys. Rev. A **21**, 480 (1980).

[HIN89] Hinds, E.A., *Atomic Physics 11* by Haroche, S., Gay, J.C., and Grynberg, G., ed. p.151. Singapore. World Scientific. (1989).

[KEN67] Keneshea, F.J., and Cubicciotti, D., J. Phys. Chem. **71**, 1958 (1967).

[KHA88] Khatsymovsky, V.M., Khriplovich, I.B., and Yelkhovsky, A.S., Ann. Phys. **186**, 1 (1988).

[KHR82] Khriplovich, I.B., and Zhitnitsky, A.R., Phys. Lett. **109B**, 490 (1982).

[KLE89] Kleinknecht, K. *CP Violation* Jarlskog, C. ed. p. 41 Singapore. World Scientific. (1989).

[KOB73] Kobayashi, M., and Maskawa, T., Prog. Theo. Phys. **49**, 652 (1973).

[KUS59] Kusch, P., and Hughes, V.W., *Handbuch der Physik* Flügge, S. ed. vol. 37/1 p. 138. Berlin. Spinger-Verlag. (1959).

[LAM87] Lamoreaux, S.K., *et al.*, Phys. Rev. Lett. **59**, 2275 (1987).

[LEE56] Lee, T.D., and Yang, C.N., Phys. Rev. **104**, 254 (1956).

[LEE73] Lee, T.D., Phys. Rev. D **8**, 1226 (1973).

[LOV87] Lovejoy, C.M., and Nesbitt, D.J., Rev. Sci. Instr. **58**, 807 (1987).

[MAR85] Mårtensson-Pendrill, A-M., Phys. Rev. Lett. **54**, 1153 (1985).

[MIL39] Millman, S., Phys. Rev. **55**, 628 (1939).

[MUR89] Murthy, S.A., Krause, D.Jr., Li, Z.L., and Hunter, L.R., Phys. Rev. Lett. **63**, 965 (1989).

[PAU68] Pauly, H., and Toennies, J.P., Methods. Exp. Phys. **A7**, 227 (1968).

[PER82] Perkins, D.H., *Introduction to High Energy Physics* 2nd ed. Reading, Massachusetts. Addison-Wesley. (1982).

[PLA70] Player, M.A., and Sandars, P.G.H., J. Phys. B **3**, 1620 (1970).

[PUR50] Purcell, E.M., and Ramsey, N.F., Phys. Rev. **78**, 807, (1950).

[RAM56] Ramsey, N.F., *Molecular Beams*. London. Oxford University Press. (1956).

[REE77] Reed, K.A., and Wharton, L., J. Chem. Phys. **66**, 3399 (1977).

[REI65] Reif, F., *Fundamentals of Statistical and Thermal Physics*. New York. McGraw Hill. (1965).

[ROT76] Roth, A., *Vacuum Technology*. Amsterdam. Noth-Holand. (1976).

[RUB81] Rubbmark, J.R., Kash, M.M., Littman, M.G., and Kleppner, D., Phys. Rev. A **23**, 3107 (1981).

[RYA84] Ryali, S.B., and Fenn, J.B., J. Phys. Chem. **88**, 245 (1984).

[SAC86] Sachs, R.G., Phys. Rev. D **33**, 3283 (1986).

[SAN64] Sandars, P.G.H., and Lipworth, E., Phys. Rev. Lett. **13**, 718 (1964).

[SAN67] Sandars, P.G.H., Phys. Rev. Lett. **19**, 1396 (1967).

[SAN68] Sandars, P.G.H., J. Phys. B **1**, 511, (1968).

[SAN75] Sandars, P.G.H., and Sternheimer, R.M., Phys. Rev. A **11**, 473 (1975).

[SCH63] Schiff, L.I., Phys. Rev. **132**, 2194 (1963).

[SCH68] Schiff, L.I., *Quantum Mechanics*. 3rd ed. New York. McGraw-Hill. (1968).

[SCH87] Schropp, D.Jr., Cho, D., Vold, T., and Hinds, E.A., Phys. Rev. Lett. **59**, 991 (1987).

[SCH88] Schropp, D.Jr., Ph.D. Thesis, Yale university, (1988), unpublished

[SLO81] Slobodrian, R.J., *et al.*, Phys. Rev. Lett. **47**, 1803 (1981).

[SMI57] Smith, J.H., Purcell, E.M., and Ramsey, N.F., Phys. Rev. **108**, 120 (1957).

[SMI90] Smith, K.F., *et al.*, Phys. Lett. **234B**, 191 (1990).

[STE 67] Stein, T.S., Carrico, J.P., Lipworth, E., and Weisskopf, M.C., Phys. Rev. Lett. **19**, 741 (1967).

[SUS84] Sushkov, O.P., Flambaum, V.V., and Khriplovich, I.B., JETP **60**, 873 (1984).

[TOE84] Toennies, J.P., *et al.*, *Proceedings of the 14th International Symposium on Rarefied Gas Dynamics* Oguchi, H. ed. p. 733 Tokyo. University of Tokyo Press. (1984).

[TRE84] Trelle, R.P., *et al.*, Phys. Lett. **134B**, 34 (1984).

[TSO79] Tsou, L.Y., Auerbach, D.J., and Wharton, L., J. Chem. Phys. **70**, 5296 (1979).

[VOL84] Vold, T.G., Raab, F.J., Heckel, B., and Fortson, E.N., Phys. Rev. Lett. **52**, 2229 (1984).

[WIG32] Wigner, E.P., Nachr. Ges. Wiss. Götingen Math-Physik K1, **(32)** 546 (1932).

[WEI76] Weinberg, S., Phys. Rev. Lett. **37**, 657 (1976).

[WEI68] Weisskopf, M.C., *et al.*, Phys. Rev. Lett. **21**, 1645 (1968).

[WIL81] Wilkening, D.A., Ph.D. Thesis, Harvard University, (1981), unpublished.

[WIL84] Wilkening, D.A., Ramsey, N.F., and Larson, D.J., Phys. Rev. A **29**, 425 (1984).

[WOL64] Wolfenstein, L., Phys. Rev. Lett. **13**, 562 (1964).

[WOL86] Wolfenstein, L., Ann. Rev. Nucl. Sci. **36**, 137 (1986).

[WU57] Wu, C.S., *et al.* Phys. Rev. **105**, 1413 (1957)